University of Southampton Research Repository

Copyright © and Moral Rights for this thesis and, where applicable, any accompanying data are retained by the author and/or other copyright owners. A copy can be downloaded for personal non-commercial research or study, without prior permission or charge. This thesis and the accompanying data cannot be reproduced or quoted extensively from without first obtaining permission in writing from the copyright holder/s. The content of the thesis and accompanying research data (where applicable) must not be changed in any way or sold commercially in any format or medium without the formal permission of the copyright holder/s.

When referring to this thesis and any accompanying data, full bibliographic details must be given, e.g.,

Thesis: Author (Year of Submission) "Full thesis title", University of Southampton, name of the University Faculty or School or Department, PhD Thesis, pagination.

Data: Author (Year) Title. URI [dataset]

UNIVERSITY OF SOUTHAMPTON

FACULTY OF NATURAL AND ENVIRONMENTAL SCIENCES

SCHOOL OF OCEAN AND EARTH SCIENCE

Volume [1] of [1]

How the interaction between sediment density flows and the seafloor influences flow evolution

By

Jamie Lee Hizzett

Thesis for the degree of Doctor of Philosophy

June 2020

UNIVERSITY OF SOUTHAMPTON

ABSTRACT

FACULTY OF NATURAL AND ENVIRONMENTAL SCIENCES

SCHOOL OF OCEAN AND EARTH SCIENCE

Thesis for the degree of Doctor of Philosophy

How the interaction between sediment density flows and the seafloor influences flow evolution

Jamie Lee Hizzett

Seafloor sediment density flows are the primary mechanism for transporting sediment to the deep sea. These flows are important because they pose a hazard to seafloor infrastructure and deposit the largest sediment accumulations on Earth. How sediment density currents interact with the seafloor is important, yet, poorly understood. This interaction is important because it governs how sediment density flows evolve along their trajectories; either by causing them to erode sediment and accelerate, or deposit sediment and to decelerate.

This thesis explores how sediment density currents interact with the seafloor by exploring flows at different scales: from field scale monitoring to controlled laboratory experiments.

Field-scale turbidity currents are investigated in the Squamish River Delta, British Columbia. Previous studies indicate that landslides are the predominant trigger of powerful flows in this and other locations. However, analysis of 93 repeat bathymetric surveys suggests that initially dilute non-landslide-triggered sediment density flows can be at least as powerful as landslide-triggered flows. For the first time, we show that settling from surface plumes can dominate the triggering of hazardous submarine flows.

This thesis uses laboratory experiments to explore how fine cohesive sediments can be incorporated into sediment gravity flows by the disintegration of eroded mud clasts. Previous laboratory studies indicate mud clasts can only travel several hundred metres before disintegration, while field observations indicate clasts can travel tens to hundreds of kilometres. They demonstrate that sand armouring can enable the transportation of mud clasts over many kilometres. The results reconcile the contradiction between field observations and previous laboratory investigations.

Finally, this thesis uses laboratory experiments to examine the sediment concentration and thickness of the basal layer of a sediment density flow. Field studies indicate the importance of dense basal layers in driving the overriding sediment gravity flow. However, the structure of these dense basal layers remains poorly understood, as no instruments are currently available to measure sediment concentration in such layers. Here we evaluate the Electrical Resistivity Tomography method and its applicability to enable us to monitor the sediment distribution within such layers in laboratory conditions.

Table of Contents

Table of Tables

Chapter 1

Chapter 2

Chapter 3

Chapter 4:

Table of Figures

Chapter 1:

Chapter 2:

Chapter 3:

Chapter 4:

Accompanying Materials

Academic Thesis: Declaration of Authorship

I, Jamie Lee Hizzett

Declare that this thesis and the work presented in it are my own, and has been generated by me as the result of my own original research.

How the interaction between sediment density flows and the seafloor influences flow evolution

I confirm that:

1. This work was done wholly or mainly while in candidature for a research degree at this University;
2. Where any part of this thesis has previously been submitted for a degree or any other qualification at this University or any other institution, this has been clearly stated;
3. Where I have consulted the published work of others, this is always clearly attributed;
4. Where I have quoted from the work of others, the source is always given. With the exception of such quotations, this thesis is entirely my own work;
5. I have acknowledged all main sources of help;
6. Where the thesis is based on work done by myself jointly with others, I have made clear exactly what was done by others and what I have contributed myself;
7. Parts of this work have been published as: *Which Triggers Produce the Most Erosive, Frequent, and Longest Runout Turbidity Currents on Deltas?*

Signed:

Date: 13/06/2020

Acknowledgements

I would like to thank the University of Southampton and the Natural and Environmental Research Council (NERC) for funding my Ph.D. studies. I would also like to thank Herriott Watt University, in particular the organisers of the Oil and Gas CDT training for all of the bespoke industry training and networking opportunities presented to me throughout my Ph.D. years. Special thanks to Lorna and Anna who not only organised the CDT training, but were exceptional in accommodating my study suspension when I needed to care for a relative.

I would like to thank my supervisors, Esther, Matthieu, Mike, and Pete. Without their encouragement and guidance I would not have been able to complete a task as daunting as a Ph.D. thesis. I would like to especially thank Esther for her exceptional counsel and support, particularly when things seemed dire. I would also like to thank Charlie Thompson for acting as panel chair and advising and encouraging me throughout my studies.

Thank you to all of my co-authors, manuscript reviewers, and everyone who has worked with me on each of my thesis chapters, as well as those who I worked with in Canada and the Netherlands on various fieldwork campaigns. I have learned so much from all of you.

Thank you to the original geohazards team who were studying at the NOCS when I joined, and to those who subsequently joined along the way. Through their example, our chats, fieldwork, and drinks, I learned a great deal. Thanks to Alessandro, Ed, James, Josh, Maria, Millie, Sophie, Will, and Zoe.

I would like to thank Gavin, Age, and Xiaodong. Gavin and Age being my friends and officemates, and Xiaodong being our adopted office-mate and honorary coffee-time group member.

Thank you to Orla for enlisting my help, and helping me with the annular flume. I learned a lot whilst troubleshooting that annular flume, and without discussions with Orla I would have struggled in my own experiments using the flume.

Thank you to my family for your encouragement, without it I would not be where I am today.

Finally, a special, big thank you to Bella. Without your continued love and support I would not be nearly as determined to finish my Ph.D. to begin our lives together with little Luna in our new family.

Chapter 1: Introduction

1.1. Overview

The purpose of this thesis is to examine the interaction between submarine sediment density flows and the seafloor. This chapter begins with a general introduction to sediment density flows, and their significance to science and wider society. I then introduce the importance of the interaction between sediment density flows and the seafloor. Finally, I describe the main research topics of this thesis, which are framed as a series of questions that are addressed in detail in Chapters 2, 3 and 4. The findings of those chapters are then synthesised in the concluding Chapter 5.

1.2. What Are Submarine-Sediment-Density Flows and Why Are They Important?

Submarine sediment density flows (hereafter termed 'sediment density flows'), as with terrestrial sediment density flows (e.g. avalanches, dust storms, and pyroclastic flows), are driven by gravitational pull on the sediment that is transported within these types of gravity flow. Submarine sediment density flows are part of a spectrum of flows (Fig. 1, 2) with low-density turbidity currents and debris flows as the end member states of the spectrum. Low-density turbidity currents are flows where fluid turbulence is supporting low concentrations of suspended sediment (Mulder and Alexander, 2001). Turbidity currents produce gradually aggrading deposits on the seafloor as the sediment progressively settles out from the flows (Kuenen and Migliorini, 1950; Bouma, 1962; Talling, 2014). At the other end of the spectrum, debris flows are characterised by high sediment concentrations, which results in suppressed turbulence levels. As a result, debris flows are often laminar and their deposits form by en-masse freezing of the flow, which is in contrast to the gradual aggrading deposits of turbidity currents. Debris flows can have a variety of sediment support mechanisms, such as the density of the sediment-water mixture, yield strength, pore pressure, and grain-to-grain interactions (Mulder and Alexander, 2001; Talling et al., 2012). Additionally, sediment density flows can transform between different flow types (e.g. transform from turbidity current to any flow in the spectrum, including debris flows, and vice versa; Fig. 1, 2), which can result in a transitional or hybrid flow (Fig. 2; Mulder and Alexander et al., 2001; Haughton et al., 2009).

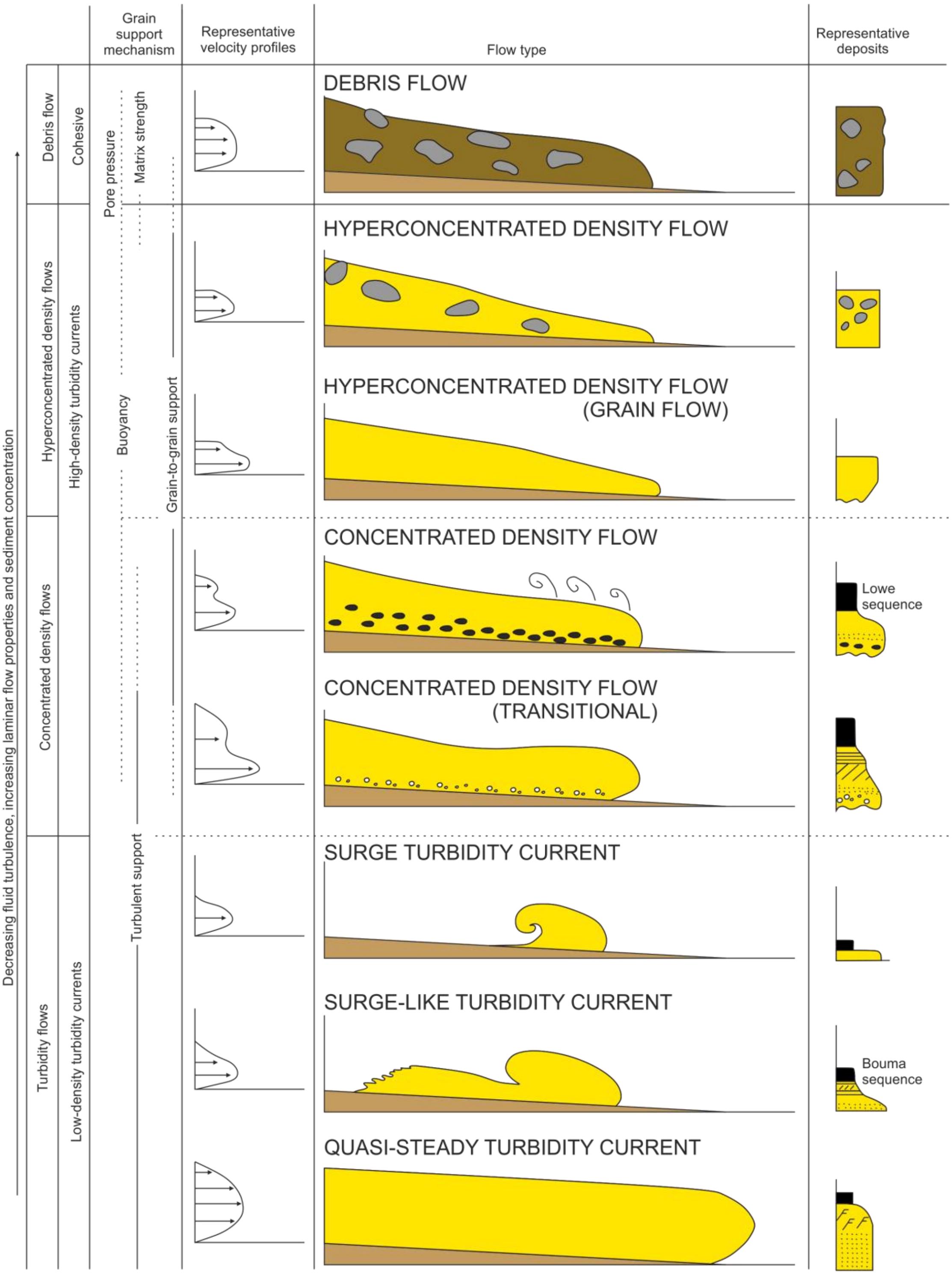

FIGURE 1:SCHEMATIC REPRESENTATION OF SEDIMENT DENSITY FLOWS SHOWING GENERALLY ACCEPTED NOMENCLATURE, GRANULAR SUPPORT MECHANISMS, REPRESENTATIVE VELOCITY PROFILES, FLOW TYPE, AND REPRESENTATIVE DEPOSITS (MODIFIED FROM MULDER AND ALEXANDER, 2001).

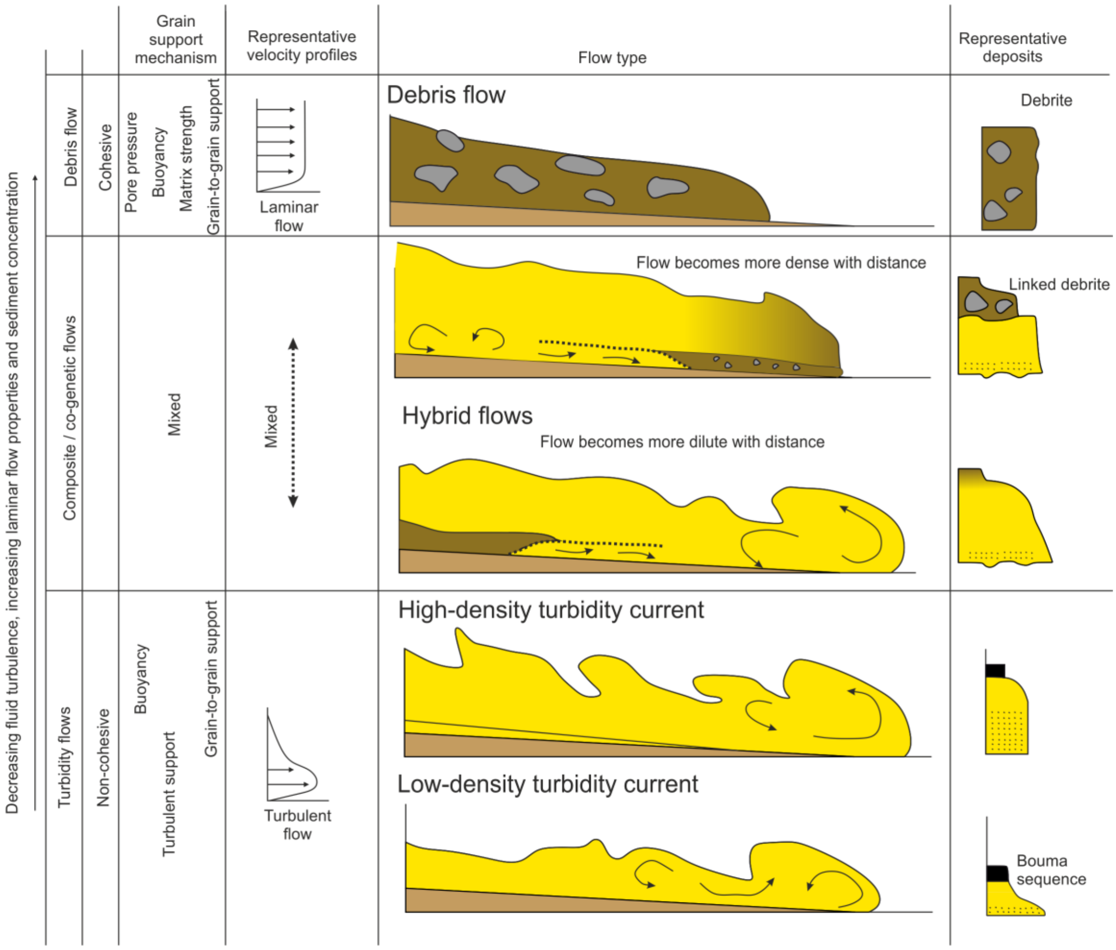

Figure 2: Schematic representation of sediment density flows that includes hybrid flows, showing generally accepted nomenclature, granular support mechanisms, representative velocity profiles, flow type, and representative deposits (Modified from Haughton et al., 2009).

Sediment density flows are important because they can transport globally significant volumes of sediment (>2000 km^3 in a single event; Haflidason et al., 2004), organic carbon (Galy et al., 2007), and pollutants (Warrick and Milliman, 2003) to the deep ocean. The deposits of sediment density flows build extensive submarine fans over geological time-scales. These fans host reservoirs that store a significant part of the global hydrocarbon reserves (Weimer and Link, 1991; Weimer and Slatt, 2004). Sediment density flows also form a potential hazard for subsea infrastructure (e.g. cables and pipelines), and have been recorded to travel in excess of 19 m s^{-1} based on sequential cable breaks (Piper et al., 1999). Sediment density flows therefore not only play an important role in the rock and carbon cycles, they are also of high socio-economic importance.

1.3. The Interaction Between Submarine Sediment-Density-Flows and the Seafloor

The primary focus of this thesis is on how sediment density flows interact with the seafloor. This interaction is important because it determines the evolution of the sediment density flows. Flows that are powerful enough to erode (and entrain) sediment from the seafloor will increase their driving force, which in turn leads to a more powerful flow and further erosion; whereas, flows that deposit sediment lose their driving force, resulting in a less powerful flow and more deposition (e.g. ignition; Pantin, 1979; Parker et al., 1986). The current lack of understanding on the exchange of sediment between the flow and the seafloor is hindering our capability to predict how flows evolve, which is essential to mitigating the hazard that these flows pose to seafloor structures, such as telecommunication cables (Heezen and Ewing, 1952) and oil and gas infrastructure (Zakeri, Høeg, et al., 2008). Additionally, our current understanding of sediment exchange between the flow and the seafloor limits our capability to predict the distribution of sediment type throughout sediment density flow deposits, which is key to characterising and extracting from subsurface hydrocarbon reservoirs hosted in ancient turbidity current deposits.

There are several long-standing scientific questions regarding sediment density flows that can only be answered by a better understanding of the interaction between these flows and the seafloor. It has been shown that some sediment density flows were capable of transporting sediment for extremely long distances (up to 1000s of km; e.g. Talling et al., 2007), but what are the physical controls that explain this? Can we learn more from the patterns of erosion and deposition from past flows? The importance of sediment entrainment to modify flow behaviour has been documented, but how precisely how does this entrainment occur in different flow types? One reason for this outstanding uncertainty is due to challenges in imaging the near-bed region beneath flows. So, how can we hope to better understand the exchange between the bed and a flow? An answer to any of these questions needs a better understanding of the sediment exchange between the sediment density flows and the seafloor; therefore this thesis centres around three specific questions regarding this interaction:

1) How does the triggering mechanism of a sediment density flow control seafloor interaction and flow evolution? (Chapter 2)
2) How do sediment density flows entrain fine cohesive sediment from the seafloor? (Chapter 3)
3) What does the interface between sediment density flows and the seafloor look like on a centimetre-scale? (Chapter 4)

1.3.1. How Does the Trigger Mechanism of the Sediment-Density-Flow Control Seafloor Interaction and Flow Evolution?

A number of potential triggers have been proposed for turbidity current initiation, including submerged slope failures (Obelcz et al., 2017; Prior et al., 1981), hyperpycnal flows (Dietrich et al., 2016; Mulder et al., 2003), hypopycnal flows (Kineke et al., 2000; Parsons et al., 2001), storm resuspension (Normandeau et al., 2014; Saucier & Chassé, 2000) and earthquakes (Goldfinger et al., 2007). Understanding how these triggers influence the resultant flow behaviour and flow run-out length is important for understanding how the seafloor is shaped, how submarine fans are built, and assessing hazards to seafloor infrastructure (Talling, 2014). It has been suggested that the most powerful and longest run-out flows are likely to originate from large-scale triggers such as gravitational collapses of submarine slopes (e.g. Heezen and Ewing, 1962; Haflidason et al., 2005; Hsu et al., 2008; Normark and Piper, 1991; Cattaneo et al., 2012; Talling, 2014). These suggestions are largely based on the idea that large collapses trigger flows that are more capable of eroding seafloor sediment, which is entrained within the flow. This entrainment enables flows to increase in mass and thus potentially accelerate and self-sustain; a condition known as 'ignition' (Pantin, 1979; Parker et al., 1986); however, to date, field datasets have not allowed us to test the influence of the trigger on the run-out distance.

In Chapter 2, an unusually detailed dataset is analysed that comprises 93 daily repeat bathymetric surveys of a highly active turbidity current system – the Squamish Prodelta, British Columbia. These repeat surveys provide evidence for more than 100 turbidity currents that eroded and deposited within three submarine channels. Each of these flows can be linked to either a landslide trigger, or was triggered by settling from a dilute river plume. Thus, here it is possible to investigate the following three questions: (1) What is the most common trigger mechanism for turbidity currents offshore from a river delta? (2) Which trigger mechanism generates turbidity currents that rework the most sediment and thus have the greatest effect on delta sculpting? (3) Which trigger mechanism produces the longest runout flows and carries the most sediment to the lobe?

1.3.2. How Do Sediment-Density-Flows Entrain Fine Cohesive Sediment from the Seafloor?

It is has been shown that the amount of fine cohesive sediment (clay) within a sediment density flow may modify its behaviour (e..g. Baas et al., 2009; Sumner et al., 2009). The type of flow (laminar or turbulent) strongly governs the nature of impact on seafloor infrastructure (Zakeri, 2010), as well as the resultant depositional geometries that can control hydrocarbon systems (Richards et al., 1998). However, the mechanism by which clay is incorporated into a gravity flow remains unclear. Chapter 3 explores how clay clasts ripped up from the seafloor disintegrate and supply clay to the flow.

Clay is the cohesive component of mud that binds via electrostatic forces. Evidence suggests that even small quantities of clay (<1%) can cause particles to gel and suppress turbulence, which leads to flow transformations (Baas et al., 2009). Clay clasts can become incorporated into a sediment density flow, either by being present in the flow from the beginning (e.g. introduced from break down of a submarine landslide), or eroded from the seafloor as rip up clasts. It is thought that such clasts release clay into a flow as they break down; however, the process by which mud clasts break down is poorly understood. Furthermore, there is an apparent contradiction between experimental work and field studies on how far clay clasts can be transported within a flow. Experiments using clear water flows suggest that mud clasts break down quickly, typically over several hundred metres (Smith, 1972). However, clay clasts observed in outcrop and modern deposits are interpreted to have travelled several tens, if not hundreds of kilometres (e.g. Stevenson et al., 2018).

The process of clast armouring may explain the contradiction between experiments and natural flows. Clast armour is a protective layer of coarse sediment (i.e. silt, sand, and/or gravel) that reduces the effectiveness of abrasive forces on the clast (Bell, 1940). There are many examples of modern armoured clasts (e.g. Bell, 1940; Stanley, 1969; Goldschmidt, 1994), and studies suggest that there are also many ancient examples (e.g. Stanley, 1964; Ponce and Carmona, 2011; Felix et al., 2009; Dasgupta and Buatois, 2012). Importantly, it is thought that the armour of terrestrial mud clasts is permanent (Bell, 1940). However, despite their common occurrence, the mechanisms responsible for the development of the armour, the importance of the armour for moderating clast abrasion rates, and thus the role that armoured mud clasts play in the transformation of turbidity currents are poorly understood.

Chapter 3 therefore seeks to understand the importance of armouring in modulating the abrasion of mud clasts and thus the transformation of turbidity currents. Specifically, Chapter 3 aims to address the follow: (1) understand the mechanism(s) by which mud clasts become armoured and if that armouring is permanent; (2) Determine how armouring affects clast abrasion, and quantify the distance that clasts with and without armour may be transported; (3) Consider the implications of clast armouring for flow transformations and interpreting deep-water deposits.

1.4.3. What Does the Interface Between Sediment-Density-Flows and the Seafloor Look Like on a Centimetre-Scale?

The part of the flow that modifies and interacts directly with the seafloor is the base of the flow. As the base of sediment density flows can attain high velocities and sediment concentrations (>10% concentration by volume) it has been challenging to make direct measurements within this zone in both the laboratory and the field. Yet observations of the base are critical as this zone controls the exchange of sediment between the flow and the seafloor. Additionally, studies have shown that the basal part of seafloor-hugging sediment density flows (e.g. turbidity currents) can generate significant impacts on pipelines and their terminals and even cause them to rupture (Zakeri, 1980; Zakeri et al., 2008). In Chapter 4, a new application of the Electrical Resistivity Tomography technique (ERT) is introduced for measuring the flow structure of this high concentration near-bed layer. The method is evaluated, and suggestions for future experiments are outlined.

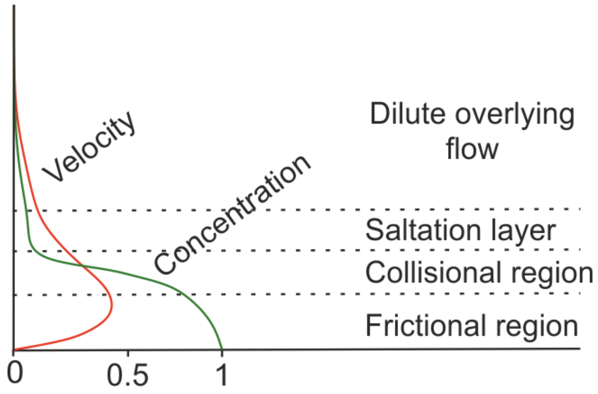

FIGURE 3: SCHEMATIC SHOWING LAYERING WITHIN STRATIFIED GRAVITY FLOWS (MODIFIED FROM SOHN, 1997).

The nature of the dense-near bed layer in sediment density flows has been debated in the past (Hiscott, 1994; Sohn, 1997) and remains one of the least understood parts of sediment density flows (Paull et al., 2018). Experimental work has shown that such dense basal layers can be on the order of millimetres to centimetres thick (Gao, 2008; Hiscott, 1994; Sumner et al., 2008; Cartigny et al., 2013). Yet field observations show that relatively denser layers at the base of turbidity currents could be metres thick (Sumner and Paull, 2014; Hughes Clarke, 2016). Our understanding of dense near-bed layers results from a lack of technology suitable to constrain the structure of such dense near-bed layers of natural flows. Conventional techniques for measuring sediment density flows in either the laboratory or on the seafloor tend to rely on acoustic backscatter, which is attenuated at ~20% sediment concentration (Gartner et al., 2004). This means that acoustic methods can only study the uppermost layers of such flows.

Unfortunately, all methods currently that are capable of measuring high sediment concentration all rely on placing sensors within the basal layer (Felix et al., 2016; Rai & Kumar, 2015) and these sensors disrupt the structure of the dense basal layer (Lanckriet et al., 2014). Examples of these methods are sediment traps (Khripounoff et al., 2003), laser diffraction probes (Shugar et al., 2010), or conductivity probes (Lanckriet et al., 2014). A non-invasive measurement technique that can measure high sediment concentrations at the base of a flow would help to improve our understanding of dense basal layers. Here a non-invasive Electrical Resistivity Tomography technique is applied as a method to measure dense-basal layers in turbidity currents.

The overall aim of the chapter is to evaluate the ERT method, including the inversion software, for measurement of high concentration flows in a flume. This is achieved by answering the following questions:

- First, the chapter aims to test the sensitivity of the inversion from voltage to sediment concentration, by examining how variation of the parameters set within the inversion software affects the shape and absolute values of the resulting sediment concentration profiles.
- Second, the resulting sediment concentration profiles are compared with previous studies to validate the sediment concentration profiles produced by the experiments.
- Third, the chapter comments on the feasibility of measuring sediment concentrations in dense basal layers with the non-invasive ERT technique for measuring sediment concentrations above 20%, and further modifications to the method are suggested.

Chapter 2: Which Triggers Produce the Most Erosive, Frequent, and Longest Runout Turbidity Currents on Deltas?

This chapter is a reproduction of a text published in *Geophysical Research Letters*.

J. L. Hizzett[1,2], J. E. Hughes Clarke[3], E. J. Sumner[2], M. J. B. Cartigny[4], P. J. Talling[4], and M. A. Clare[1], 2017, Which triggers produces the most erosive, frequent, and longest runout turbidity currents on deltas? *Geophysical Research Letters*, 45, 2. 855-863.

[1]National Oceanography Centre, University of Southampton, Waterfront Campus, Southampton, UK
[2]Ocean and Earth Science, National Oceanography Centre Southampton, University of Southampton, Southampton, UK
[3]Center for Coastal and Ocean Mapping, University of New Hampshire, Durham, NH, USA
[4]Departments of Earth Science and Geography, University of Durham, Durham, UK

Abstract

Subaerial rivers and turbidity currents are the two most voluminous sediment transport processes on our planet, and it is important to understand how they are linked offshore from river mouths. Previously, it was thought that slope failures or direct plunging of river floodwater (hyperpycnal flow) dominated the triggering of turbidity currents on delta fronts. Here we reanalyse the most detailed time-lapse monitoring yet of a submerged delta; comprising 93 surveys of the Squamish Delta in British Columbia, Canada. We show that most turbidity currents are triggered by settling of sediment from dilute surface river plumes, rather than landslides or hyperpycnal flows. Turbidity currents triggered by settling plumes occur frequently, run out as far as landslide-triggered events, and cause the greatest changes to delta and lobe morphology. For the first time, we show that settling from surface plumes can dominate the triggering of hazardous submarine flows and offshore sediment fluxes.

2.1 Introduction

River deltas play an important role in global carbon and sediment cycles. They receive much of the annual flux of 20 Gt of fluvial sediments that is either stored in deltas or redistributed in the oceans (Milliman and Farnsworth, 2013). Fjords fed by river deltas store 11% of the carbon delivered by rivers to the ocean each year. Sediment is redistributed over the submarine part of deltas by turbidity currents. Turbidity currents pose a hazard to subsea infrastructure such as cables and pipelines (Carter et al., 2014). Understanding how turbidity currents are triggered and evolve is key to linking fluvial sediments to their ultimate resting place in the world's oceans.

Here we seek to understand how turbidity currents are triggered offshore from river mouths, and which trigger mechanism produces the most frequent, erosive, and longest runout turbidity currents. These factors are particularly important because they determine which flows are the most hazardous, or transport the most sediment and cause the most seabed change, and thus play the greatest role in transforming deltas. There are few direct observations of turbidity currents in action, and even fewer observations of multiple turbidity currents at one site with different triggers. This means that although a number of trigger mechanisms have been proposed, there are few field studies that document which triggers dominate and are associated with the largest sediment fluxes. In this study we analyse the most detailed time-lapse mapping yet from a deltaic system to understand how trigger mechanisms are linked to flow behaviour and runout. This data set comprises 93 near-daily time-lapse surveys acquired at Squamish Delta in Howe Sound, Canada, during the 2011 freshet. These surveys define 95 turbidity current events, recognized by changes in seafloor elevation, across the three channels (Fig. 1; Hughes Clarke, 2016; Hughes Clarke et al., 2014, 2012)

We seek to understand the importance of turbidity currents formed by different trigger mechanisms at a fjord-head delta. Our aims are to (1) determine which is the most common trigger mechanism for turbidity currents, (2) show which trigger mechanism generates turbidity currents that rework the most sediment and thus have the greatest effect on delta sculpting, and (3) determine which trigger mechanism produces the longest runout flows and carries the most sediment to the lobe.

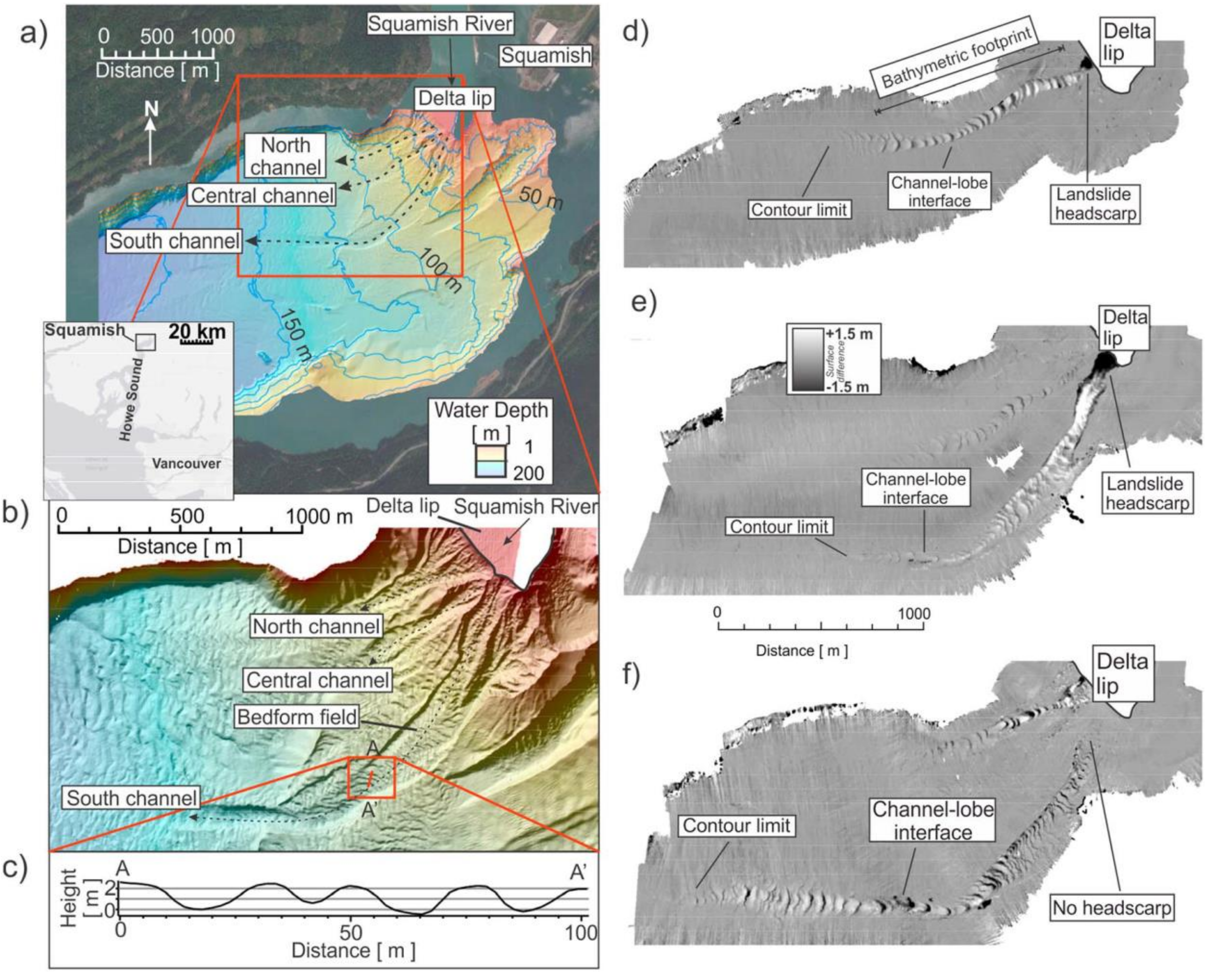

Figure 1: (a) Overview bathymetric map of the Squamish Delta. Inset map shows the location of Squamish Delta. (b) Bathymetric map of the Squamish Delta showing the channels and associated bedform fields. (c) The morphology of bed forms on the channel floor. (d–f) Changes in seafloor elevation between bathymetric surveys on different days in 2011, showing morphological footprint of individual flows. The white patches indicate areas characterized by deposition in between surveys, while the black patches indicate areas characterized by erosion. (d) Flow triggered by a small volume landslide (~4,000 m3). (e) Flow triggered by a large volume landslide (~22,000 m3). (f) Flow triggered by sediment setting from a surface plume, which lacks a landslide headscarp. Note that the small landslide (Figure 1d) and the settling plume trigger (Figure 1e) produce longer runout turbidity current than the large landslide (Figure 1f).

2.1.1 Past Work on Turbidity Current Triggers on Deltas

Various processes have been proposed to trigger turbidity currents on deltas, these include submarine landslides (Obelcz et al., 2017; Prior et al., 1981); and plunging (hyperpycnal) river plumes (Dietrich et al., 2016; Mulder et al., 2003), sediment settling from surface (hypopycnal) river plumes (Kineke et al., 2000; Parsons et al., 2001), and by sediment remobilised by internal waves or tides (Normandeau et al., 2014; Saucier and Chassé, 2000).

Submarine slope failures (hereafter called “landslides”) can mix with seawater to generate more dilute turbidity currents that runout further than the toe of the landslide deposit. Landslides can occur due to over steepening of the prograding delta lip and can be released abruptly (Prior et al., 1981) or gradually by retrogressive breaching (Mastbergen and Van Den Berg, 2003). Landslides can transform into turbidity currents if the body of sediment disintegrates, enabling turbulence to suspend sediment (Felix and Peakall, 2006). The runout of landslide-triggered turbidity currents is poorly documented and understood. Large volume terrestrial landslides runout further than small volume landslides (Dade and Huppert, 1998). However, it is unknown if the same relationship holds in the ocean where the flow can evolve and transform through water entrainment.

Hyperpycnal flows occur when rivers form a sediment-laden plume that is denser than the ambient seawater (Mulder and Syvitski, 1995). Such a hyperpycnal plume plunges beneath the seawater and flows along the basin floor as a turbidity current. Hyperpycnal flows in marine environments are thought to occur during river flood events when suspended sediment concentrations exceed ~40 kg m^3 (Mulder et al., 2003). Hyperpycnal flows can erode sediment from the seafloor (Dietrich et al., 2016), thus enhancing their density contrast and leading to acceleration (Pantin, 1979; Parker et al., 1986).

Turbidity currents triggered by sediment settling from a river plume, hereafter called “plume-triggered events,” occur when sediment settles out from a buoyant surface (hypopycnal) plume onto the seafloor (Parsons et al., 2001). Sediment is initially concentrated in sheets or small-scale fingers at the base of the buoyant plume. This can lead to sediment concentrations that exceed 20 kg m^{-3} and result in sediment settling (Parsons et al., 2001). Detailed field observations of plume events are rare (Lintern et al., 2016) but have shown that resulting flows can be fast moving (>10 ms^{-1}). Plume events are as yet an understudied phenomenon and are documented by few field studies (e.g., Hughes Clarke et al., 2014; Kineke et al., 2000; Lintern et al., 2016) or inferred from numerical (Shao et al., 2017) and laboratory studies (Parsons et al., 2001; Sequeiros et al., 2009).

Once turbidity currents are triggered, they can evolve along three trajectories. In the first trajectory, (1) the flow erodes more sediment than it deposits leading to “self”-acceleration (Pantin, 1979; Parker et al., 1986). This increases flow density and leads to acceleration of the flow, which in turn leads to further erosion. The second trajectory (2) leads to a dissipating flow (Pantin, 1979; Parker et al., 1986), where the flow deposits more sediment than it erodes. This net deposition reduces the density contrast and the flow decelerates. The third trajectory (3) bypasses sediment causing near-equal amounts of sediment deposition and erosion. However, the relationship between triggering mechanism and subsequent flow evolution is poorly understood due to a lack of suitably detailed field observations.

2.2 Regional Background

Squamish Delta is an example of a sandy fjord-head system in which water depths increase rapidly offshore to 100 m within ~1 km of the shore (Hughes Clarke et al., 2014; Fig. 1a). The delta front comprises three distinct channel-lobe systems with bed form fields (northern, central, and southern channels; Fig. 1b) formed by turbidity currents (Hughes Clarke et al., 2012). The bed forms in each channel (interpreted as cyclic steps, Hughes Clarke et al., 2012) interact with, and are maintained by, turbidity currents (Fig. 1c).

During the May–October freshet the Squamish River discharge exceeds 350–500 m^3 s^{-1}, with occasional flood peaks in excess of 1,000m^3 s^{-1} (Clare et al., 2016; Hughes Clarke et al., 2014). Bed load from the gravelly riverbed flows over the delta lip, sometimes causing progradation of >10 m in a single day. However, much of the delta front sediment is fine-to-medium sand, which is finer than the gravel-dominated bed load in the river channel. This suggests that the delta front sediment mostly originates from the ebb tide river wash load carried offshore in a surface plume (Hughes Clarke, 2016). Rapid (>3,000 m^3 per low tide) accumulation of sediment leads to slope failure (Hickin, 1989; Hughes Clarke et al., 2012), with the largest (50,000–150,000 m^3) delta lip failures typically occurring a few hours after flood peaks (Clare et al., 2016). Suspended sediment measurements in the river plume show that sediment concentrations are insufficient (usually <0.07 kg m^{-3}) to form a plunging (hyperpycnal) flow (Hughes Clarke et al., 2014).

Hughes Clarke et al. (2014) demonstrated that turbidity currents commonly occur at low tides due to sediment settling from the Squamish River plume. Sediment settling from the river plume was demonstrated by high backscatter both at the surface and in the water column (Fig. 2).

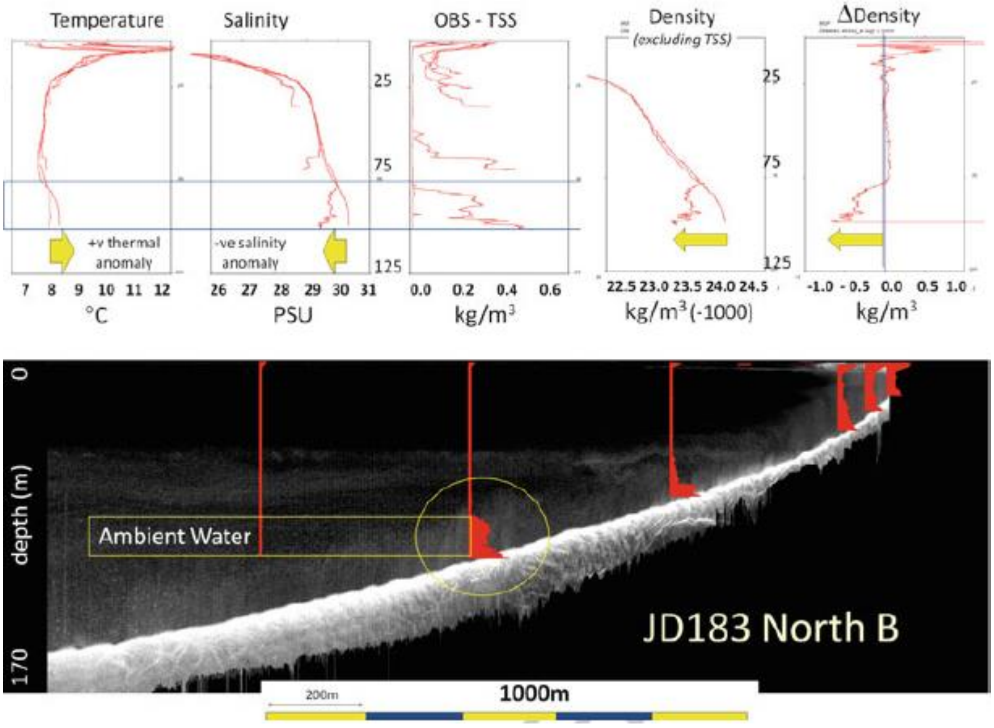

Figure 2: Figure showing how sediment settling from the river plume coincides with a turbidity current. Optical backscatter profiles (red) superimposed on multibeam water-column backscatter data for one flow in 2012. The upper plots show temperature, salinity, and suspended sediment profiles for six casts along the multibeam profile. The image shows high-backscatter at the surface resulting from a sediment-laden plume, along with high backscatter above the sea-bed from a turbidity current (From Hughes Clarke et al., 2014, p. 261).

Similar observations of plume-triggered turbidity currents have been made offshore from other rivers globally (e.g. Sepik River, Papua New Guinea, Kineke et al., 2000, and Fraser River Delta, Canada, Ayranci et al., 2012; Kostaschuk et al., 1993; Lintern et al., 2016). These observations are also in agreement with the experimental models of Parsons et al. (2001), which show that turbidity currents can be triggered by river plumes with densities below the threshold required for river plunging. While the exact mechanism by which settling plume sediment generates turbidity currents is still poorly understood, it seems likely that this mechanism is more widespread than currently recognized due to the lack of appropriate monitoring data (Wright and Friedrichs, 2006). To determine whether conditions at the Squamish Delta are typical, we compare the suspended sediment flux, discharge, and sediment yield with 566 other rivers in the global database (Fig. 3) of Peucker-Ehrenbrink (2009). The

Squamish River, and other rivers where turbidity currents are known to be triggered by settling from river plumes (Fraser Delta, Sepik River), fits well within the broad spread of measurements. This suggests that settling plumes may also be likely in many other locations globally.

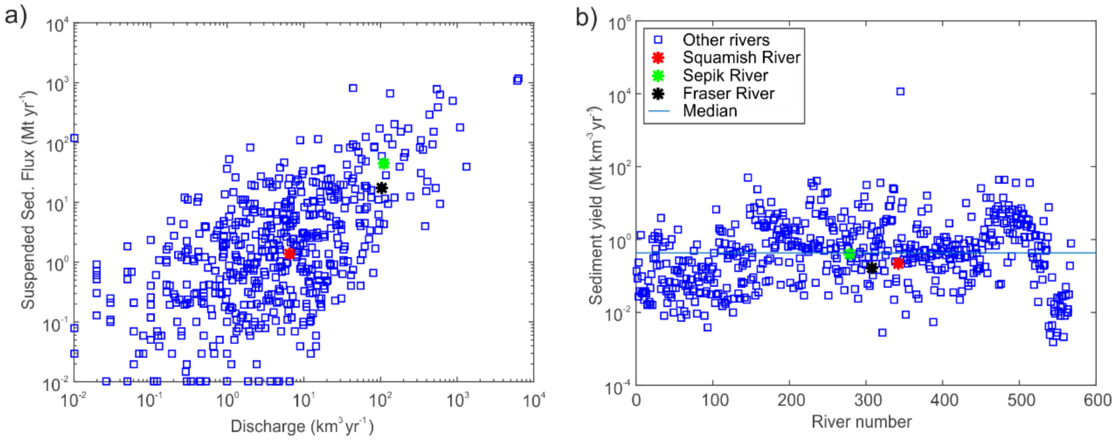

Figure 3: **a)** Plot comparing annual water discharge, and annual suspended sediment flux, of the Squamish, Fraser and Sepik Rivers with 564 rivers from around the world. **b)** Comparison of the annual sediment yield ($Sed. Flux * (\frac{1}{Q})$) between the Squamish, Fraser, and Sepik Rivers with 564 other rivers from around the world. The Fraser River (e.g. Ayranci et al., 2012; Kostaschuk et al., 1993; Lintern et al., 2016) and Sepik River (e.g. Kineke et al., 2000) are highlighted because settling plumes have been shown to trigger turbidity currents at these locations.

2.3 Methods

Here we study the relationship between flow triggers and flow evolution. Both the type of trigger and how the flow evolves are deduced from changes in seafloor morphology (Fig. 1c–1e), between 93 sequential near-daily surveys. This allows us to define 95 turbidity currents that occurred across three channels on the delta front. We use this to understand flow runout and behaviour from patterns of erosion and deposition caused by these flows. We distinguish landslide-triggered flows, from flows that we infer to be triggered by sediment settling from surface plumes, using the presence or absence of a landslide headscarp.

Data were collected using an EM710 multibeam sonar with a vertical resolution of 0.2% of water depth, and a horizontal resolution of 3% of water depth. The active prodelta region was surveyed every weekday, with the distal delta surveyed every fortnight. The very shallow water (<5 m) delta top was also surveyed on a semiweekly basis (Hughes Clarke et al., 2012).

We calculated the difference in seafloor elevation between consecutive bathymetric surveys, which are typically 1 day apart, but can be 3 days apart across weekends. We define an event when there is discernible change in seafloor morphology, and subdivide events that affected the southern, central, and northern channels on the delta front. When there is change in more than one channel during the same period, these are counted as separate events. We note that more than one turbidity current or landslide may have occurred between consecutive surveys. Landslide volumes for surveys across weekends are not significantly greater than those during weekdays, and the three largest landslides occurred between weekdays, suggesting that this variable time period between surveys is not causing detectable bias (Fig. 4).

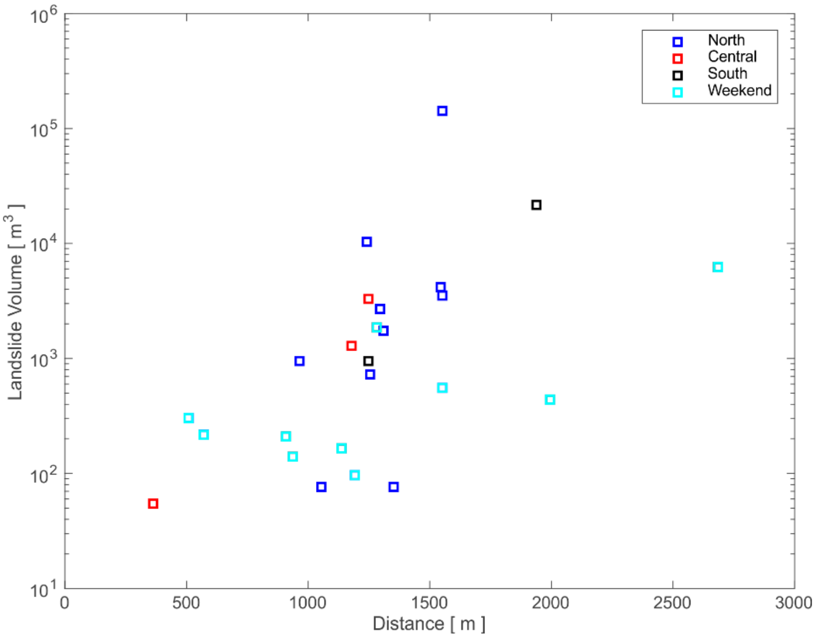

FIGURE 4: RUNOUT DISTANCE OF EVENTS COMPRISING AN INITIAL LANDSLIDE AND SUBSEQUENT TURBIDITY CURRENT, PLOTTED AGAINST INITIAL LANDSLIDE VOLUME. RUNOUT DISTANCE IS DEFINED FROM THE PATTERN OF VISIBLE CHANGE TO THE SEAFLOOR BETWEEN REPEAT SURVEYS. EVENTS BETWEEN DAILY SURVEYS ARE SHOWN FOR THE NORTHERN (BLUE SQUARES), CENTRAL (RED SQUARES) AND SOUTHERN (BLACK SQUARES) CHANNELS, WHILST EVENTS BETWEEN SURVEYS ACROSS A WEEKEND ARE SHOWN BY CYAN-COLOURED SQUARES. THE PLOT SHOWS LARGER VOLUME EVENTS DID NOT OCCUR PREFERENTIALLY DURING THE MORE WIDELY SPACED (3 DAY) SURVEYS ACROSS WEEKENDS.

Flows cause upstream migration of bed forms (Hughes Clarke et al., 2012; Hughes Clarke, 2016; Fig. 1b). Such upslope migrating bed forms are represented in the difference map by adjacent patches of leeside erosion and stoss-side deposition (Fig. 1c–1e). If the volume of erosion on the lee slope exceeds deposition on the stoss slope, then this represents an overall increase in the volume of sediment within the turbidity current. If the erosion and deposition are almost equal, the flow is said to be bypassing as there is no net change in flow volume across one bed form. The evolution of the total amount of sediment in the turbidity current is then calculated by the cumulative loss and gain of sediment volumes with distance from the delta lip (Fig. 5a). For error estimations see Figure 6.

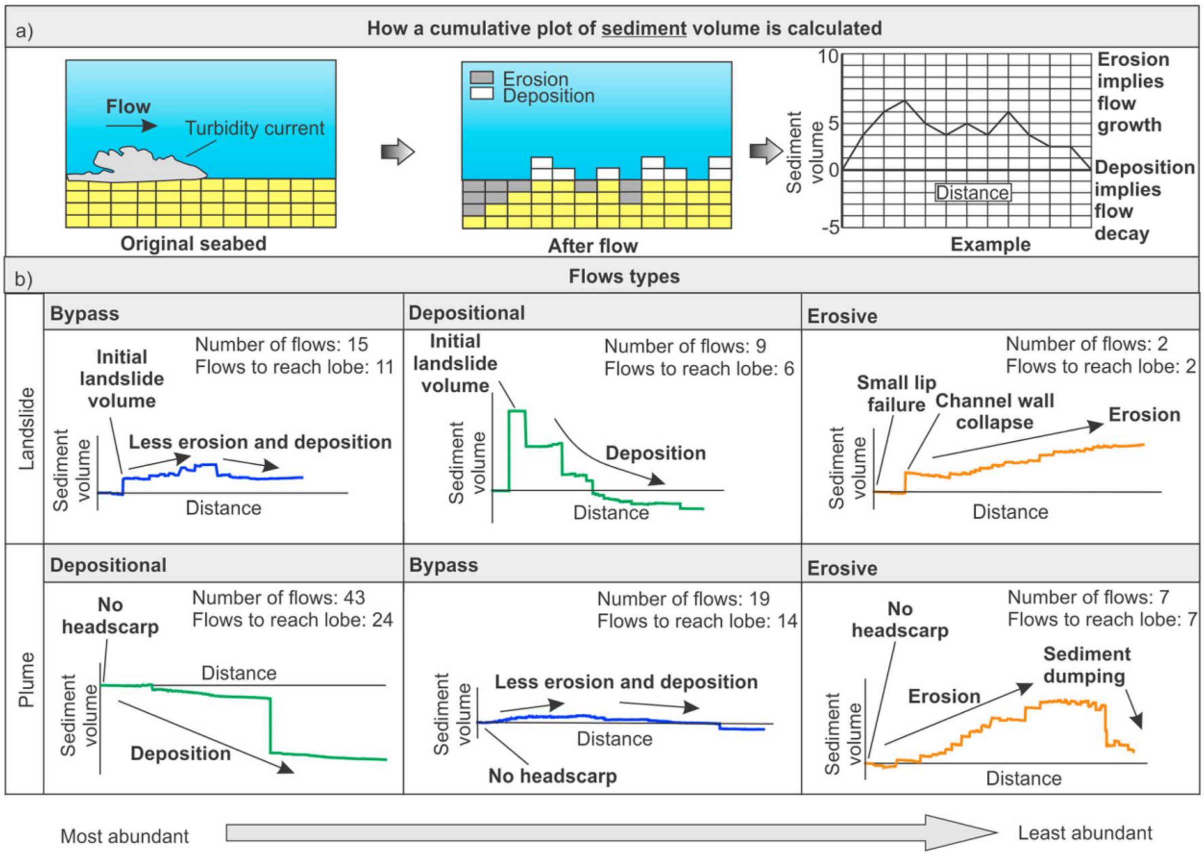

Figure 5: (A) Explanation of how cumulative plots for turbidity current erosion and deposition patterns are calculated. (B) Event types classified according to their initial trigger (landslide or settling from plume) and are then ranked by their abundance as either net depositional, net bypassing, or net erosional in terms of flow volume. The cumulative profiles depicted are not shown to scale. Flow volume is calculated using the initial landslide volume (plume events start with zero volume), and cumulative amounts of sediment eroded or deposited along the flow pathway. The number of events of each type are noted, as are the number of those events that reach the lobe.

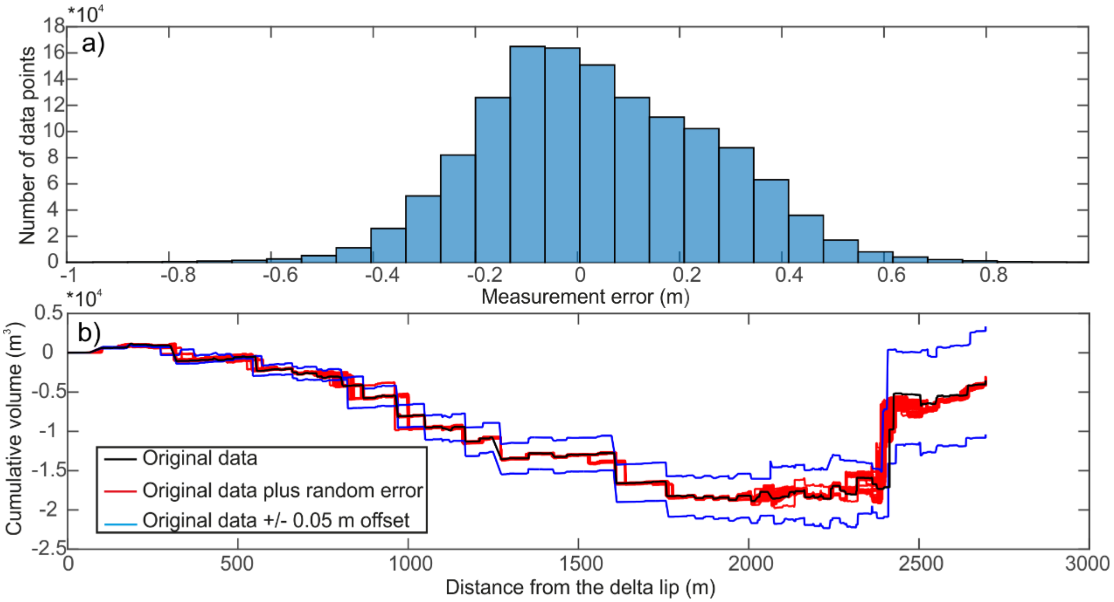

*Figure 6: Estimation of error in the volume calculations. **a)** The distribution of difference map offset values during ten days that lacked any turbidity current activity. The data show that the error is roughly normally distributed with a mean offset of 4 cm and a standard deviation of 23 cm. **b)** Estimation of the effect of these errors on the cumulative volumes. The red curves show 100 realisations of the original data plus randomly attributed normally distributed errors with a standard deviation of 23 cm. The blue curves indicate the cumulative error resulting from a +/- 5 cm offset. The black curve shows the original data.*

The flow trigger is defined using the presence or absence of a visible head scar near the delta lip in the difference maps, which typically have a vertical resolution of a few tens of centimetres. Given that events initiate in water depths below 60m and the vertical resolution is 0.2% water depth, the worst-case scenario is that a head scar thinner than 12 cm would not be recognized. As the delta top was surveyed only every 3 or 4 days, this means that the headwall region of some landslides may not have been surveyed on some days, yielding an underestimation of initial landslide volume. This occurred for 6 out of a total of 26 landslide events (Fig. 7).

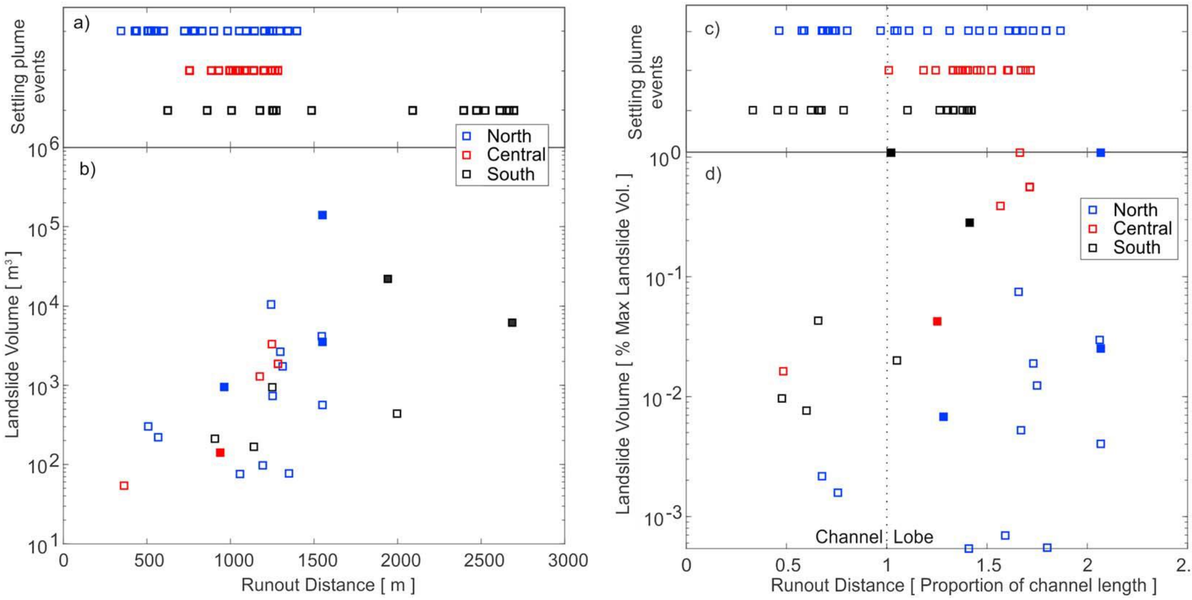

Figure 7: a) The runout distance of plume-triggered turbidity currents, which originate from the north, central and southern channels. Note that these three channels have different lengths, and longer channels may favor longer runout. b) Relationship between initial landslide volume and runout distance, subdivided for events starting in the north, central and southern channels. c) Normalized runout of plume-triggered turbidity currents. d) Normalized volume and runout of landslide events. Solid squares indicate a landslide whose initial volume is underestimated due to a missing headwall on one of the survey pairs because the water at the delta lip was too shallow to survey.

Runout is measured as the distance from the first to last contour that shows discernible (typically >0.25 m) bathymetric change (Fig. 1c–1e). We note that flows may have runout further but failed to cause resolvable change to the seafloor. Additionally, mass balance of many of the events is not equal and is the result of the resolution of the data.

2.4 Results

2.4.1 Trigger Mechanism and Flow Frequency

Events inferred to be triggered by settling from river plumes account for 73% of the flow events, while landslides and their associated turbidity currents account for the remaining 27% of events (Fig. 5).

2.4.2 Trigger Mechanism and Flow Behaviour

The 95 flows that we analyse (Fig. 8) exhibit six distinct combinations of behaviour (bypass, deposition, and erosion) and trigger (landslide or plume trigger) (Figure 5b). All combinations can reach the lobe, which is defined as the area where flow exits the channel and expands.

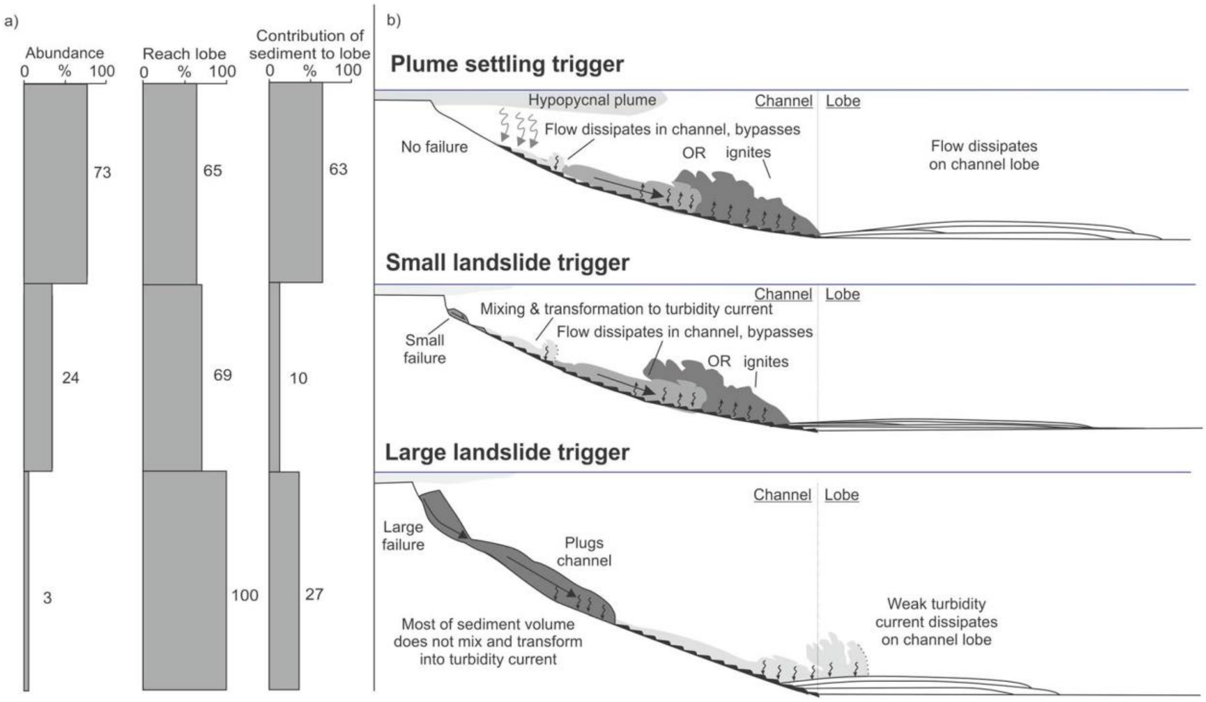

Figure 8: A summary of flow behaviors at Squamish Delta. A) The bar charts represent the abundance of flows from plume events (top), small landslides (<10,000 m3) (middle), and large landslides (>10,000 m3) (bottom), percentage of these flows that reach the lobe, and the relative contribution of those flows to deposition on the lobe. B) Cartoons summarizing the typical flow evolution of turbidity currents triggered by sediment settling from surface plumes, and by small or large landslides.

The most common landslide events display net-bypassing behaviour; near-equal volumes of sediment are eroded from the stoss and lee slopes of each bed form, resulting in little net change in suspended sediment; they have a headscarp of variable volume. The second-most common landslide events are net depositional; they typically, although not always, result from the largest volume landslides. The cumulative profiles of net-depositional landslide events show exponential decay of cumulative volume, and negligible volumes of erosion in comparison. Net erosive landslides are relatively rare; they are highly erosive events that begin with a small headscarp and tend to occur in conjunction with additional failures along the channel (Fig. 9).

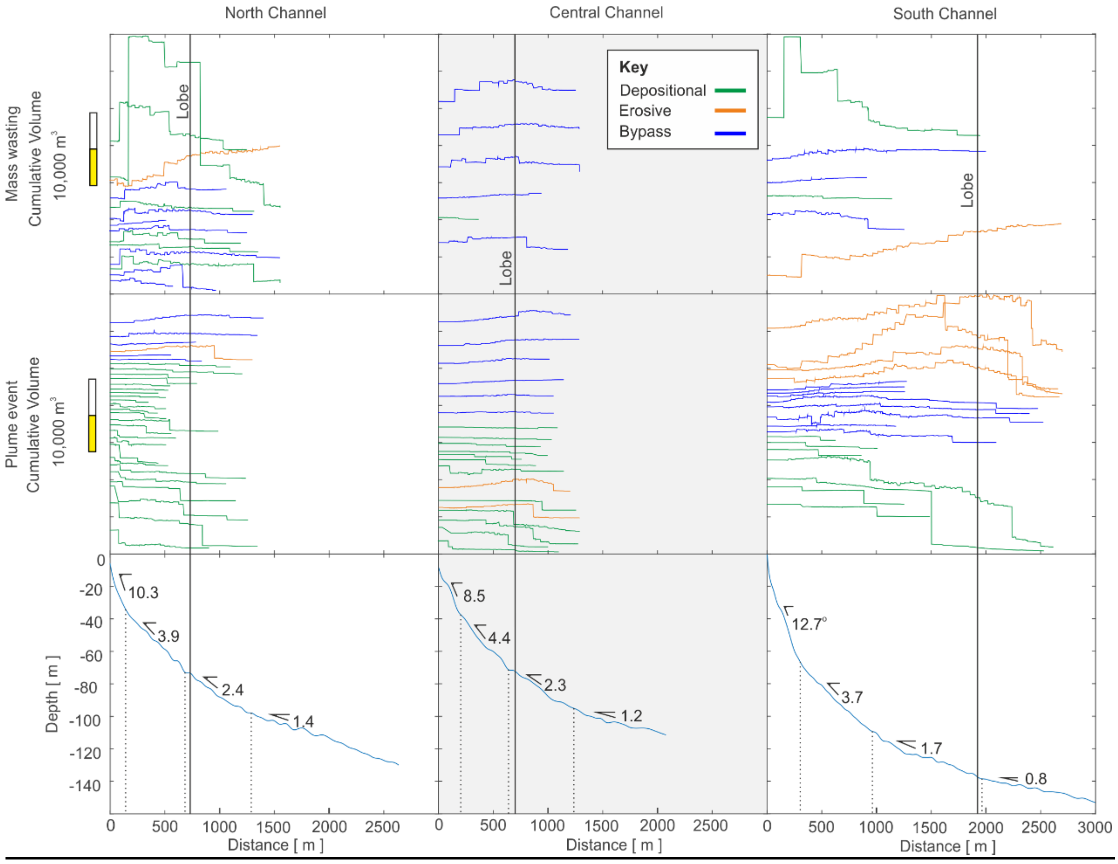

Figure 9: Plots showing cumulative change in sediment volume with distance in events. Channel termination depicted by a vertical line labelled 'Lobe'. These volumes include initial landslide volume (if landslide triggered), and subsequent erosion and deposition documented by changes in seafloor bathymetric maps. The plots show A) landslide-triggered events, and B) events triggered by settling from surface plumes, which occurred in the northern central and southern channels. Colour coding shows net-depositional (green), net-erosional (orange), and mainly bypassing (blue) events. And this colour coding is consistent with Figure 4. C) Bathymetric profiles along the northern, central and southern channels, showing changes in gradient (in degrees) and the position of the channel-lobe transition (vertical black lines).

The most common settling plume events are net depositional, the second-most common settling plume events exhibit bypassing behaviour, and the least common settling plume events are erosive, accounting for only ~10% of plume events. The erosive plume events have long runout distances and always reach the channel lobe where they deposit the majority of their sediment. Erosive settling plume events begin to lose erosive power while still within the channel, but do not begin to deposit large amounts of sediment until they reach the lobe. Erosive settling plume events tend to coincide with peaks in river discharge (Fig. 10).

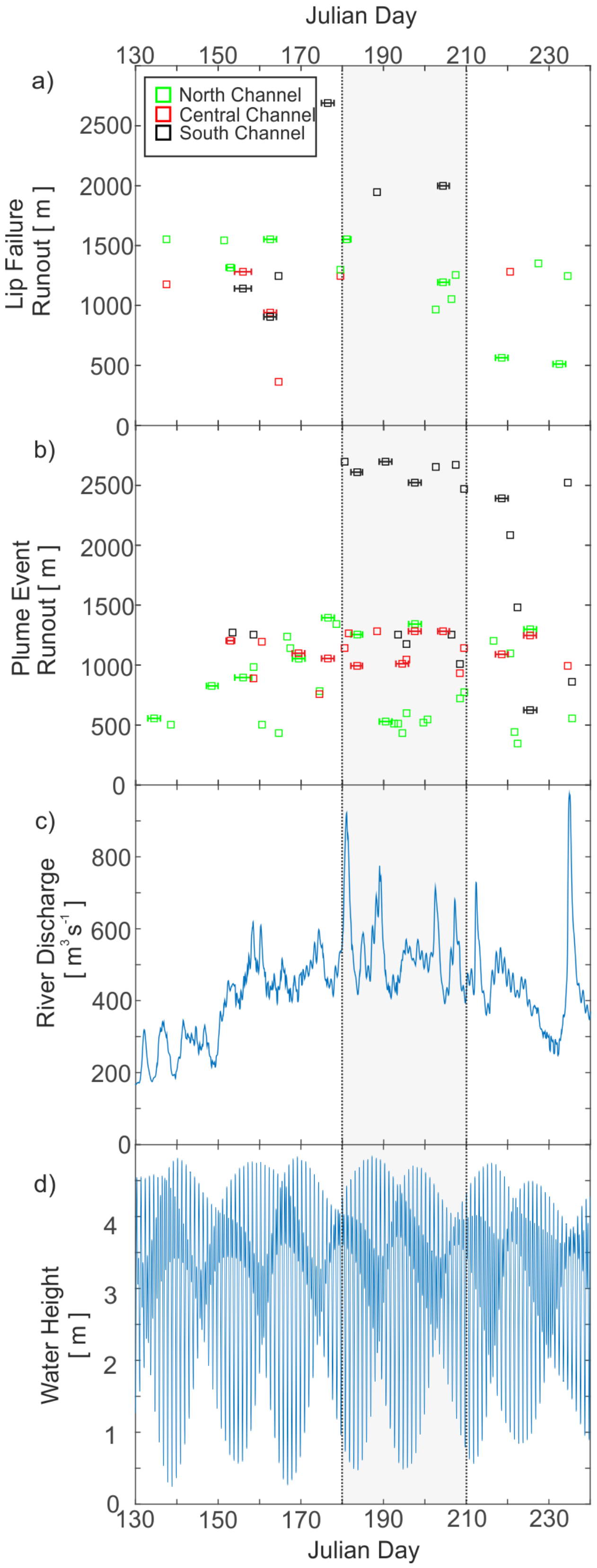

*FIGURE 10: **A)** LANDSLIDE RUNOUT DISTANCE VERSUS THE DAY ON WHICH THE EVENT OCCURRED. **B)** PLUME EVENT RUNOUT DISTANCE THE DAY ON WHICH IT OCCURRED. **C)** RIVER DISCHARGE DURING THE SURVEY PERIOD. **D)** WATER HEIGHT DURING THE SURVEY PERIOD SHOWING TIDAL CHANGES. WHISKERS ON A AND B CORRESPOND TO THE FIRST AND SECOND SURVEY OF A SURVEY PAIR. GREY SHADING INDICATES A PERIOD OF*

HIGHER RIVER DISCHARGES WHICH COINCIDED WITH A NUMBER OF LONG RUNOUT SETTLING PLUME AND LANDSLIDE EVENTS.

2.4.3 Trigger Mechanism and Runout Distance

The longest runout flows are not caused by a single particular trigger (Fig. 5, 7), although long runout events are usually associated with peaks in river discharge (Fig. 10). Landslide events show no clear relationship between landslide volume and runout; some of the largest landslides have short runout distances and create channel-plugging deposits (Fig. 9). Runout distances are affected by channel length, which varies for the northern, southern and central channels (Fig. 7, 9). Additionally, landslide volume could be affected by the delta lip configuration, which varies for the different channels.

In order to consider whether channel length or relative landslide volume has an influence on runout distance, in Figure 7 we show the data in both the absolute and normalized format. The runout length has here been normalized by the channel length, and the landslide volume has been normalized by the maximum observed landslide volume in that channel. The shorter northern and central channels display greater normalized runout distances than the longer southern channel. The scatter in relationship between landslide volume and runout is enhanced by normalizing the initial volume and runout. This highlights that shorter channels experience a greater number of events reaching the channel lobe, relative to longer channels.

Settling plume events are the most common turbidity current trigger. Settling plume events are the least effective at reaching the lobe, but because of their relative abundance, they contribute the most sediment to the lobe. This highlights the importance of plume events in progradation of the channel-lobe system.

2.5 Discussion

2.5.1 Which Trigger Mechanism Forms the Most Frequent Turbidity Currents and Transports the Most Sediment?

We find that plume events are surprisingly the most frequent turbidity current trigger on the Squamish Delta. Previous work suggests that landslides (Obelcz et al., 2017; Prior et al., 1981) and hyperpycnal flows (Dietrich et al., 2016; Mulder et al., 2003) are the most important turbidity current trigger on deltas (Piper & Normark, 2009), while here we found that plume events and landslides transport similar net volumes of total sediment during the survey period, depositing 385,000 m^3 and 330,000 m^3 of sediment, respectively. It might be expected that settling plume events would transport less sediment owing to their dilute origins (Parsons et al., 2001), but this is not the case.

2.5.2 Which Trigger Mechanism Reworks Sediment the Most and has the Greatest Effect on Delta Sculpting?

A lower percentage of plume-triggered events reach the lobe relative to landslide-triggered events. However, plume events are more frequent, produce more erosive flows, and contribute more sediment to the lobe than landslide events. Plume-triggered events therefore rework the most sediment within the time frame of the survey period. This highlights the importance of plume events in lobe-building and channel extension, while landslides largely appear to contribute sediment to the delta front. This is in contrast to the literature that suggests that landslides (Obelcz et al., 2017; Prior et al., 1981) and hyperpycnal flows (Dietrich et al., 2016; Mulder et al., 2003) are the most common sediment transport mechanisms on river deltas.

The apparent mobility of plume-triggered events, relative to landslides, may be a result of the initial high density of a landslide-triggered event, compared to the more dilute plume-triggered events. The ability of any turbidity current to erode sediment, and self-accelerate, depends on the near-bed sediment concentration (Eggenhuisen et al., 2017; Parker et al., 1986). Turbulence is dampened if the sediment concentration is too high. Landslides have been shown to struggle to disintegrate and become turbulent (Felix & Peakall, 2006), and these events may deposit most of their sediment or bypass (Sequeiros et al., 2009). As a result, dense landslide-triggered flows may not be able to erode sediment and therefore the volume of sediment in suspension will decay with distance. Overall landslide-triggered turbidity currents rework the bed less, across the survey period, than plume-triggered turbidity currents because they occur less frequently.

2.5.3 The Relationship Between Trigger and Turbidity Current Runout

We find that the turbidity current trigger does not dictate runout distance. Terrestrial landslides show a strong relationship between increased volume and longer runout (Dade & Huppert, 1998). At the Squamish Delta, events that comprise an initial landslide and associated turbidity current exhibit a poor relationship between volume and runout (Fig. 7). This may be partly because runout distance relates to the ability of the landslide to disintegrate and mix with ambient fluid to form a turbidity current (Felix & Peakall, 2006). The core of larger landslides may be shielded from mixing with ambient water thus inhibiting disaggregation. Smaller landslides may be able to disintegrate more effectively and produce a turbidity current that can then travel further. However, plume-derived turbidity currents at Squamish Delta commonly exhibit long runouts, although this is partly because they are common in the longer southern channel (Fig. 5, 7). Long runout plume events also tend to be erosive events. Plume events originate from the dilute river plume (Hughes Clarke et al., 2012), and this low initial concentration may enable them to maintain turbulence that suspends sediment enabling long runout (Sequeiros et al., 2009).

2.5.4 Wider Implications

It was previously considered that extreme events such as earthquakes (Goldfinger, 2011), river floods (Mulder et al., 2003), and delta collapses (Girardclos et al., 2007) triggered the large-scale turbidity currents required to build channel lobes. However, in this study we find that plume events cause the most seafloor change, contribute the most sediment to the channel lobe, and are most hazardous for seafloor infrastructure, at least over short (3–4 month) time scales. Mechanisms similar to the plume settling process described here have been observed in other locations, including offshore from the Sepik River (Kineke et al., 2000), and Fraser River (Lintern et al., 2016). Sediment concentrations and fluxes at the Squamish Delta, and Sepik or Fraser Rivers, are not unusual (Fig. 3). While the frequency and importance of plume-triggered turbidity currents remains to be tested in a wider range of settings, the implications of this work are important. Flows that reach the depositional lobes do not need to be triggered by landslides, earthquakes, or hyperpycnal floods. We show for the first time that settling from surface river plumes can sometimes dominate the triggering of submarine flows, and offshore sediment fluxes.

2.6 Acknowledgements

The data used to produce the plots in this paper are available online at https://data.nodc.noaa.gov/cgi-bin/iso?id=gov.noaa.nodc:0169399. Jamie L. Hizzett is funded jointly by National Environmental and Research Council (NERC) Centre for Doctoral Training (CDT) in Oil and Gas and the University of Southampton. During the period of data acquisition, John Hughes Clarke was supported by the Natural Sciences and Engineering Research Council (Canada) and the sponsors of the Chair in Ocean Mapping at the University of New Brunswick. Esther J. Sumner was supported by the Natural Environment Research Council projects NE/M017540/1. Matthieu J.B. Cartigny was supported by the Natural Environment Research Council projects NE/P009190/1, NE/M017540/1, and NE/M007138/1. Peter J. Talling was supported by the Natural Environment Research Council projects NE/N012798/1, NE/P009190/1, NE/M017540/1, and NE/M007138/1. Michael A. Clare was supported by the Natural Environment Research Council projects NE/N012798/1 and NE/P009190/1. We thank the crew of the CSL Heron who collected the data used in this report.

Chapter 3: Mud clast armouring and its implications for turbidite systems

This chapter is a reproduction of a text accepted in the *Journal of Sedimentary Research*.

Jamie L. Hizzett[1,2], Esther J. Sumner[2], Matthieu J. B. Cartigny[3], and Michael A. Clare[1].

[1] National Oceanography Centre, University of Southampton, Waterfront Campus, Southampton, UK, [2]Ocean and Earth Science, National Oceanography Centre Southampton, University of Southampton, Southampton, UK, [3]Departments of Earth Science and Geography, University of Durham, Durham, UK

Abstract

Seafloor sediment density flows are the primary mechanism for transporting sediment to the deep sea. These flows are important because they pose a hazard to seafloor infrastructure and deposit the largest sediment accumulations on Earth. The cohesive sediment content of a flow (i.e., clay) is an important control on its rheological state (e.g., turbulent or laminar); however, how clay becomes incorporated into a flow is poorly understood. One mechanism is by the abrasion of (clay-rich) mud-clasts. Such clasts are common in deep-water deposits, often thought to have travelled over large (more than tens of kilometers) distances. These long travel distances are at odds with previous experimental work that suggests that mud-clasts should disintegrate rapidly through abrasion. To address this apparent contradiction, we conduct laboratory experiments using a counter rotating annular flume to simulate clast transport in sediment density flows. We find that as clay clasts roll along a sandy floor, surficial armouring develops and reduces clast abrasion and thus enhances travel distance. For the first time we show armouring to be a process of renewal and replenishment, rather than forming a permanent layer. As armouring reduces the rate of clast abrasion, it delays the release of clay into the parent flow, which can therefore delay flow transformation from turbidity current to debris flow. We conclude that armoured mud-clasts can form only within a sandy turbidity current; hence where armoured clasts are found in debrite deposits, the parent flow must have undergone flow transformation further up slope.

3.1 Introduction

The clay content of submarine sediment density flows is a fundamental control on their rheology and the resulting flow dynamics. However, the mechanisms by which clay is ingested into submarine sediment density flows, particularly by the disaggregation of mud-clasts, remain poorly understood. Understanding the dynamics of submarine sediment density flows is important, because they transport sediment and organic carbon to the deep sea (Galy et al., 2007), pose a potential hazard to seafloor infrastructure (Chi et al., 2012), and their deposits represent some of the most important hydrocarbon reservoirs on Earth (Stow and Johansson, 2000). Determining how such flows behave is key to determining how and where they transport sediment, accurately assessing the threat posed to seafloor structures, and determining the quality of hydrocarbon reservoirs formed by their deposits (Bruschi et al., 2006; Zakeri, Hoeg, et al., 2008; Baas et al., 2011; Haughton et al., 2009; Sumner et al., 2009).

Research over the past 15 years has revealed that sediment density flows may switch between turbulent and laminar regimes and that this “transformation” can strongly affect the geometry and nature of the resultant deposits, as well as the flow itself (Haughton et al., 2009; Talling et al., 2013). In this paper we recognize that turbidity currents and debris flows are two end-member states of the spectrum of submarine, gravity-driven sediment density currents. We define turbidity currents as dilute, typically Newtonian flows in which fluid turbulence is the main particle support mechanism (Mulder and Alexander, 2001), and deposit sediment in a layer-by-layer fashion (Talling et al., 2004). Debris flows are typically laminar, and cohesive (Talling et al., 2012; Hermidas et al., 2018; Hampton, 1975; Kuenen, 1951; Lowe, 1988). The main particle support mechanisms in debris flows include yield strength, pore pressure, particle buoyancy, and grain-to-grain interactions (Talling et al., 2012). Hybrid flows occur when turbidity currents transform into debris flows (or vice versa). Turbidity currents transform when there is sufficient cohesive sediment available to damp turbulence and transform the flow into a debris flow (Sumner et al., 2009; Baas et al., 2011; Haughton et al., 2003; Talling et al., 2004). The overall flow event (turbidity current and debris flow) is referred to as a hybrid flow. The resulting deposit, which comprises a turbidite juxtaposed with a debrite that is ”genetically linked” (i.e., a linked debrite; Fig. 9; Haughton et al., 2003; Jackson and Johnson, 2009; Talling, 2013) is called a hybrid deposit. The incorporation of cohesive sediment into flows has been shown to be an important control on flow rheology, governing when and where flows transform (Baas et al., 2011; Sumner et al., 2009). For instance, a flow may begin as a fully turbulent turbidity current, but through the incorporation of even relatively small amounts (< 1% vol.) of additional cohesive sediment, turbulence can become damped, leading to transformation into a debris flow (Baas et al., 2011; Sumner et al., 2009; Haughton et al., 2009; Talling, 2013; Fisher, 1983; Patacci, Haughton, and McCaffrey, 2014). Despite the important role that cohesive sediment plays in the behavior and transformation of sediment density currents, the mechanisms by which mud (and thus clay) is incorporated into and mixed within such flows remain poorly constrained.

One mechanism proposed for the incorporation of cohesive sediments is the direct entrainment of fluid muds from the seafloor. These unconsolidated muds typify much of the global ocean floor (Kineke et al., 1996) and are easily remobilized by sediment density currents (Schieber et al., 2010), readily becoming mixed throughout the flow (Kranenburg and Winterwerp, 1997). However, the presence of more consolidated mud-clasts, which are often found in sediment-density-current deposits (e.g., Southern et al., 2015), indicates that ingestion and mixing of fluid mud is not the only mechanism to incorporate clay into a flow. Mud-clasts may originate from matrix disintegration (i.e., during the early stages of a landslide; Stevenson et al., 2018), or may be plucked from the seafloor by an erosional flow (i.e., rip-up clasts; Patacci et al., 2014; Fonnesu et al., 2016). Mud-clasts are also known as mud balls (Bell, 1940), clay pebbles (Nossin, 1961), clay galls (Pettijohn, 1957), intra formational clasts (Smith, 1972; Mueller et al., 2017), till balls (Goldschmidt, 1994), intraclasts (Chang and Grimm, 1999), and mud lumps (Pantin, 1967). Once incorporated into a flow, mud-clasts are subsequently abraded as they are rolled along the bed by the density current, resulting in the release of clays into the flow (Bell, 1940; Smith, 1972), which can cause flow transformation (Baas et al., 2011; Sumner et al., 2009; Haughton et al., 2009). Mud-clasts in subaerial environments typically travel between several hundred meters and a few kilometers (Bell, 1940; Smith, 1972). This contrasts with observations of mud-clasts in deep-water deposits that are inferred to have travelled over tens of kilometers or more, although their actual transport distances are often unclear (Table 1). This may be a function of differences between marine and fluvial environments, including the nature of the material in the rip-up clasts e.g., dry versus saturated clays. We thus limit comparisons with fluvial environments and concentrate on marine environments. Several factors affect how far a mud-clast may travel, including initial clast water content (Smith, 1972; Mather et al., 2008; Schieber et al., 2010), bed composition (Hermidas et al., 2018), initial size (Smith, 1972), clast hardness (Schieber, 2016; Stevenson et al., 2018), the presence of extracellular-polymeric substances (EPS; Malarkey et al., 2015), and clast armouring (Bell, 1940; Smith, 1972).

3.1.1. Mud-clast Armouring

Mud-clast armouring is observed in many modern environments, including river channels (Bell, 1940; Little, 1982; Mather et al., 2008), lakes (Dickas and Lunking, 1968), coastal environments (Stanley, 1969; Tanner, 1996), continental shelves (Goldschmidt, 1994), submarine channels (Stevenson et al., 2018), and even city streets following heavy rain (Ojakangas and Thompson, 1977). The armour is composed of sand and/or gravels that adhere to the soft outer surface of the mud-clast as it rolls along the substrate (Bell, 1940; Chun et al., 2002). Armour tends to be one grain in thickness (Bell, 1940), but it can penetrate a mud-clast by up to three grain thicknesses (Chun et al., 2002).

Importantly, the armour is considered to form a permanent protective layer in ephemeral fluvial environments (Bell, 1940). Armoured mud-clasts have been observed in a number of deep marine settings (Table 1). Despite the number of studies citing the presence of armoured clasts, the number of studies that cite the presence of mud-clasts that are not armoured is much greater. As with clast transport generally, armour development may depend on factors such as the stickiness (i.e., initial water content; Smith, 1972; and the presence of EPS; Malarkey et al., 2015), and the size of the clast relative to the surrounding sediment (Bell, 1940), and clast hardness (Schieber et al., 2010, 2016). Previous experiments have examined the abrasion of air-dried dried mud chips, simulating clasts sourced from subaerial desiccated mud (Smith, 1972), sand-size lithified mudstone (Schieber et al., 2016), and submillimeter- to centimeter-size water-rich kaolinite rip-up fragments (Schieber et al., 2010). However, in the submarine environment, landslides can consist of a variety of sediments at (Stevenson et al., 2018) various stages of consolidation (i.e., a range of shear strengths; Fig. 1).

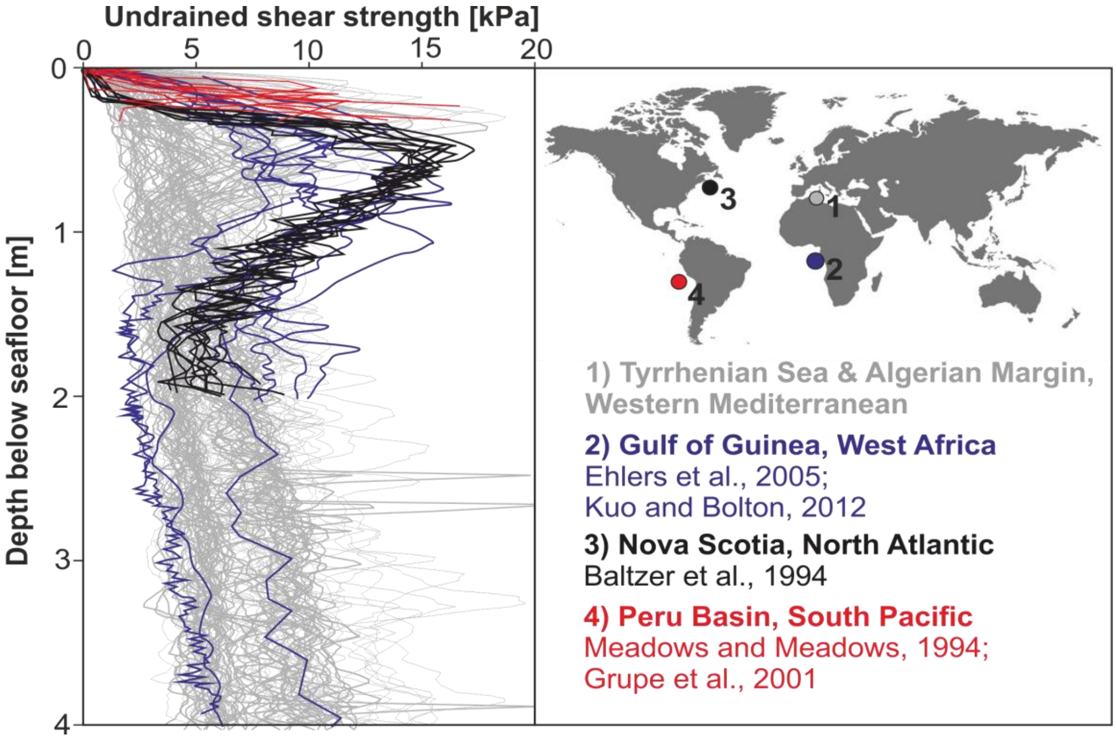

Figure 1: The range in undrained-shear-strength profiles of various seafloor muds from around the globe.

Previous studies have tested the transportation distance of muds at either end of the shear-strength scale - lithified mud (Schieber et al., 2016) as well as mud with a high water content (Schieber et al., 2010). However, no studies have tested the transport-survival prospects of a mud or clay clast of intermediate shear strength (simulating a clast sourced from 1 - 2 m burial depth; Fig. 1), nor has any previous study tested armouring under controlled conditions. It is also often unclear how far clasts in outcrops have travelled (Table 1). The mechanisms responsible for the development of the armour, the importance of the armour for moderating clast abrasion rates, and thus the role that armoured mud-clasts play in the transformation of turbidity currents are poorly understood.

Ancient examples

	Geographical location	Travel distance	Armouring	Clast size trends	Inferred flow type	References
Outcrops	Annot sandstone, France	Thought to be several kilometers. Origin of clasts unknown.	Armoured	Up to 80 cm	Turbidity current	Stanley, 1964
	Bed 1, Marnoso-Arenacea Formation, Italy	~ 40 km. Origin of clasts unknown.	Not mentioned	Decrease with distance. Clasts > 25 cm only extend up to 20 km along bed transect, smaller sizes extend to ~ 50 km along bed transect	Hybrid flow	Sumner et al., 2012
	Bed 5, Marnoso-Arenacea Formation, Italy	~ 10 km, possibly up to 80 km. Origin of clasts unknown.	Not mentioned	Clasts up to 10 - 25 cm diameter at 80 km along bed transect. Clasts > 25 cm cease after 20 km along bed transect.	Hybrid flow	Sumner et al., 2012
	Huanghae Formation, China	Proximal to the slope failure region	Armoured	20 - 40 cm	Debris flow	Chun et al., 2002
	Mayaro Formation, Trinidad	Unknown	Armoured	Clast size not mentioned	Turbidity current	Dasgupta and Buatois, 2012
	Miocene Austral Foreland Basin, Chile	Up to 700 m	Some armoured	Up to 15 cm diameter	Turbidity current	Ponce and Carmona, 2011
	Monterey Formation, California, USA	Unknown	Not mentioned	Clasts up to 1 cm diameter	Turbidity current or debris flow	Chang and Grimm, 1999
	Oligocene Fusaru Sandstone and Lower Dysodilic Shale, Romania	Unknown	Not mentioned	Centimeter-scale	Turbidity current	Sylvester and Lowe, 2004
	Polish Carpathians	Up to tens of kilometers	Some armoured	Up to ~ 30 cm	Turbidity current	Felix et al., 2009
	West Crocker Fan, NW Borneo	Probably several tens of kilometers, although exact origin unknown	Not mentioned	Up to 2 m in diameter	Turbidity current / debris flow	Jackson et al., 2009

Cores	Bed 5, Agadir basin, NW Africa	~ 25 km	Not mentioned	Clasts 5 - 10 cm in diameter	Hybrid flow	Stevenson et al., 2014; Sumner et al., 2012
	Britannia Formation, North Sea, UK continental shelf	Up to 100 km	Some armoured	Clasts > 15 cm diameter	Hybrid flow	Haughton et al., 2003
	Modern Examples					
	Geographical location	**Maximum travel distance**	**Armouring**	**Clast size trends**	**Inferred flow type**	**References**
Cores	Cook Strait, New Zealand	Unknown	Not mentioned	Clasts < 5 cm in diameter	Turbidity current	Pantin, 1967
	Grand Banks deposit, Newfoundland, Canada.	> 100 km	Armoured	Clasts < 7 cm in diameter	Turbidity current	Stevenson et al., 2018
	Sur Landslide, USA	Up to 100 km	Some armoured	Clasts 5 cm in diameter	Debris flow	Gutmacher and Normark, 2002

TABLE 1: COMPARISON OF MUD-CLAST TRAVEL DISTANCES RELATIVE TO THEIR ARMOURED STATE, CLAST SIZE TRENDS, AND INFERRED FLOW TYPES.

3.1.2. Aims of This Study

We seek to understand how non-lithified clay clasts abrade in a sand-rich turbulent flow and the importance of armouring in modulating the abrasion of mud-clasts. First, we aim to understand the mechanism(s) by which mud-clasts become armoured and whether that armouring is permanent. Second, we determine how armouring affects clast abrasion, and quantify the distance that clasts with and without armour may be transported. As part of this aim, we specifically investigate how varying suspended-sediment concentration and angularity of the sediment in the flow may control clast abrasion. Finally, we consider the implications of clast armouring for flow transformation and the interpretation of deep-water deposits.

3.2. Methods

Our experiments were conducted in a recirculating, ring-shaped annular flume with rotating paddles and a counter rotating base. The annular flume has a radius of 0.53 m, the paddles are 10 cm long, and the channel is 0.23 m deep to the base of the paddles and is 0.145 m wide (Fig. 2A, B). The flume has a total capacity of 160 liters, in which we used fresh water (Fig. 2A, B). The Perspex floor of the annular flume was lined with D_{50} 158 µm angular Silverbond® sand (by gluing). Secondary circulation was minimized by rotating the base of the tank in the direction opposite to that of the paddles (Sumner et al., 2009). Secondary circulation was considered to be minimised when there was an even deposit of sediment across the width of the channel. Annular flumes have been used in previous studies to simulate long-duration flows (e.g. Smith, 1972), and can generate flows with velocities and bed shear stresses comparable to those of natural turbidity currents (Kuenen, 1966; Sumner et al., 2008) and as a result can suspend sediment of a size similar to that of sediment found in natural deposits. We test the effect that different flow and sediment parameters have on clast abrasion, specifically: flow velocity, sediment angularity, and suspended-sediment concentration.

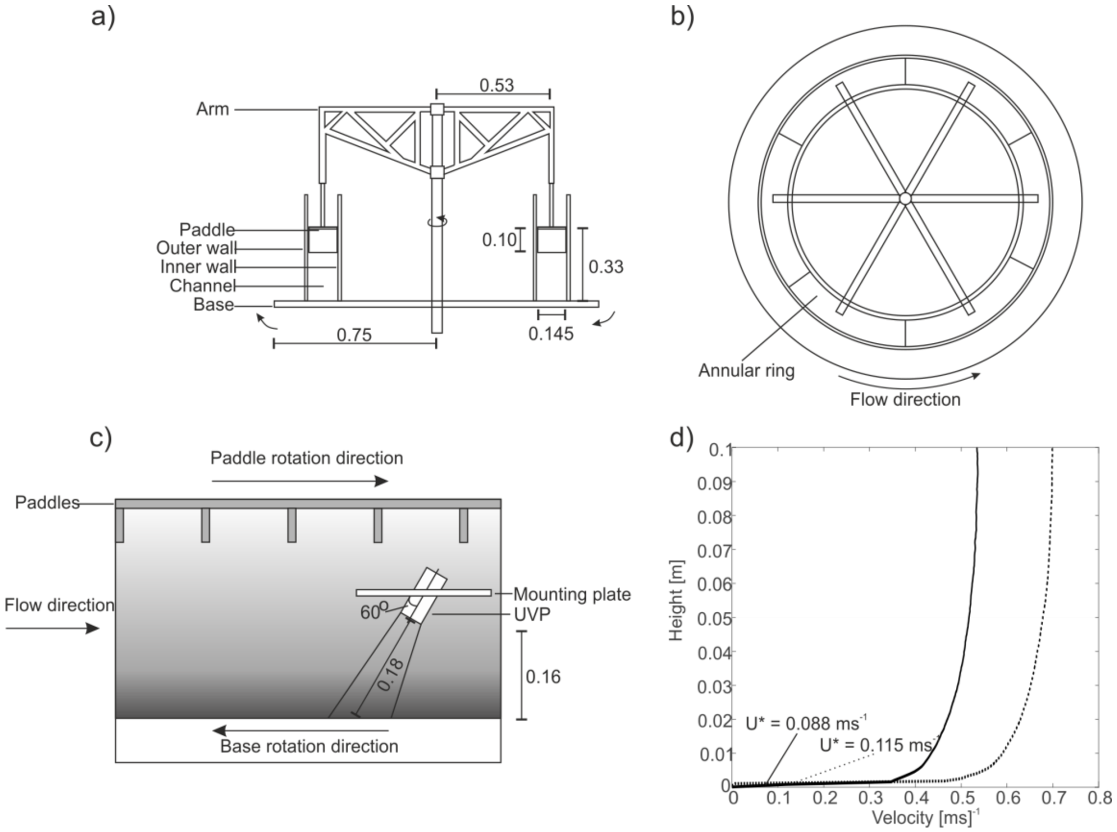

FIGURE 2: EXPERIMENTAL SETUP SHOWING **A)** CROSS-SECTIONAL VIEW OF THE ANNULAR FLUME WITH DIMENSIONS, **B)** A PLAN VIEW OF THE ANNULAR FLUME, **C)** THE ORIENTATION OF THE UVP IN THE ANNULAR FLUME, **D)** THE VELOCITY PROFILE RECORDED BY THE UVP FOR THE FAST (GRAY DASH) AND SLOW (BLACK) FLUME SETTINGS.

3.2.1. Clay Clasts

Each experiment included ten cube-shaped clasts (8 cm^3) made of SCOLA air-drying modelling clay. Measurements made by a fall-cone penetrometer show that the clay clasts have undrained shear strengths of 17 - 40 kPa. These measurements are comparable to normally to lightly overconsolidated sediments found at and close (within 1 - 2 m depth) to the seafloor at a range of deep-sea sites worldwide (Fig. 1; e.g., Baltzer et al., 1994; Kuo and Bolton, 2013; Meadows & Meadows, 1994; Yin et al., 2016). Shear strength of the SCOLA clay was not degraded when clasts were remolded. SCOLA clay is composed of quartz (35%), illite smectite (39%), kaolinite (21%), and haematite (5%) (Yin et al., 2016). It is unclear how the stickiness of SCOLA clay would compare with a natural mud, which depends on the clay mineral, clay fraction, plasticity, moisture content, degree of consolidation, as well as shear strength (Kooistra et al., 1998). Therein lies a spectrum of natural variability, which would greatly affect the armouring mechanism being studied here. However, the advantage of using SCOLA clay over a naturally occurring mud is that the properties of the clay are reproducible (i.e., both in these experiments and in further experiments).

3.2.2. Flow Conditions

In the experiments two flow velocities were simulated, 0.5 and 0.7 ms^{-1}, which were found to be the approximate thresholds for sliding and rolling (respectively) of the clasts on a smooth flume floor. The flow velocities used in our experiments produce similar shear stresses ($u^* > 0.09$ ms^{-1}) to those of natural sediment gravity flows (Straub and Mohrig, 2008; Cartigny et al., 2013; Fig. 2D) (Straub and Mohrig, 2008; Cartigny et al., 2013; Fig. 2D). Shear velocity is estimated using

$$U * = U_{max} k \left[\ln\left(\frac{h_{max}}{0.1\ D_{90}}\right) \right]^{-1} \tag{1}$$

Where k is the von Kármán constant (0.4). We assume a logarithmic velocity profile between the bed and the velocity maximum (Van Rijn, 1993). We used two sediment types with different angularities: rounded (75 - 250 µm ballotini), and angular (125 - 250 µm Silverbond® sand). Runs with bulk sediment concentrations of 0%, 1%, and 10% were performed. However, due to the carrying capacity of the flows, not all of the sediment became suspended. An aggraded bed of up to 1 cm was observed during the 1% bulk sediment experiments, which represents approximately 20% of the sediment added to the flume. A sediment wave the length of the flume of 1 cm to 7 cm height was observed during the 10% bulk sediment experiments, which represents approximately 50% of the sediment added to the flume. Flow profiles were measured using a 1 MHz ultrasonic velocity profiler (UVP) (Fig. 2D). Flow measurements were conducted in independent experimental runs, without the addition of clay clasts, to avoid interaction between the clasts and the UVP probe. In these independent runs, the UVP probe was fixed at 160 mm above the bed and set at an incidence angle of 60^o normal to the flow (De Leeuw et al., 2016) with a sediment concentration of 1% angular sand. The velocity was averaged over five minutes. In order to calculate clast travel distance, we use video evidence to determine particle velocity by timing particle movements between vertical pillars on the flume tank. The particle velocity was approximately 85% of the maximum fluid velocity. This value is higher than some previously published values, as the counter-rotating annular flume produces a velocity maximum that is only 7 cm from the bed (Fig. 2).

3.2.3. Experimental Procedure

Experiments were run for one hour. Ten clasts were used in each experiment to provide multiple data points per experiment. Preliminary experiments demonstrated that there was no difference in the rate and type of abrasion with one clast, or ten clasts in the flow. The clasts were cut to size using a cheese wire, and their size was measured using calipers. The clasts were then placed at regular spatial intervals around the channel of the flume tank. Each experiment was conducted at either the slow or fast velocity (0.5 or 0.7 ms^{-1} respectively). Every ten minutes, the flow was stopped and the clay clasts were retrieved and weighed, photographed, and returned to the flume at regular spatial intervals. After one hour the clay clasts were removed and allowed to dry. During experiments that included suspended sediment, the sediment was allowed to settle out at the end of the ten-minute sample period, and the clasts were put back in on top of the bed. A subsample of angular sediment was removed from the armour of two clasts for analysis using a Hitatchi TIM-1000 scanning electron microscope (SEM).

3.3. Results

3.3.1. Armouring Mechanisms

Clasts became more rounded and smaller as the experiments progressed (Figs. 3, 4). In experiments with sediment, clasts became armoured within the first ten minutes of the experiment as they rolled along the substrate (Fig. 5). These clasts then transitioned through four morphological stages as they abraded (Figs. 4, 6). In stage 1, the cube-shaped clasts were observed to roll or bounce along the bed. When the clasts were removed after ten minutes, they had become either barrel shaped (stage 2) or subrounded (stage 3). During stage 2, the clasts were barrel shaped and armoured only along the minor axis, and not the barrel tops and bottoms, which were also softer than the rest of the clast. Stage 2 was observed only in the 10%-sediment-concentration experiments, and was probably not observed in other experiments due to this stage being shorter than the ten-minute measurement period. In stage 3, the clasts became subrounded (but not fully spherical) and armoured around all axes; the softened tops and bottoms of the barrel shaped clasts had abraded. In stage 4, the clasts were both rounded and armoured. The clasts continued to abrade, and the rate of abrasion declined with decreasing size and increasing sphericity. The latter two stages occupied 57 – 85% of each experiment. In all experiments except the 10%-concentration experiments, the clasts had reached stage 4 by the end of the one-hour experiment. The exceptions to this were the 10% angular sand experiments, in which clasts abraded the slowest and had attained only stage 3 by the end of the experiment. SEM images of sand grains that fell out of armoured clasts show that the sand grains have clay particles attached to them (Fig. 6).

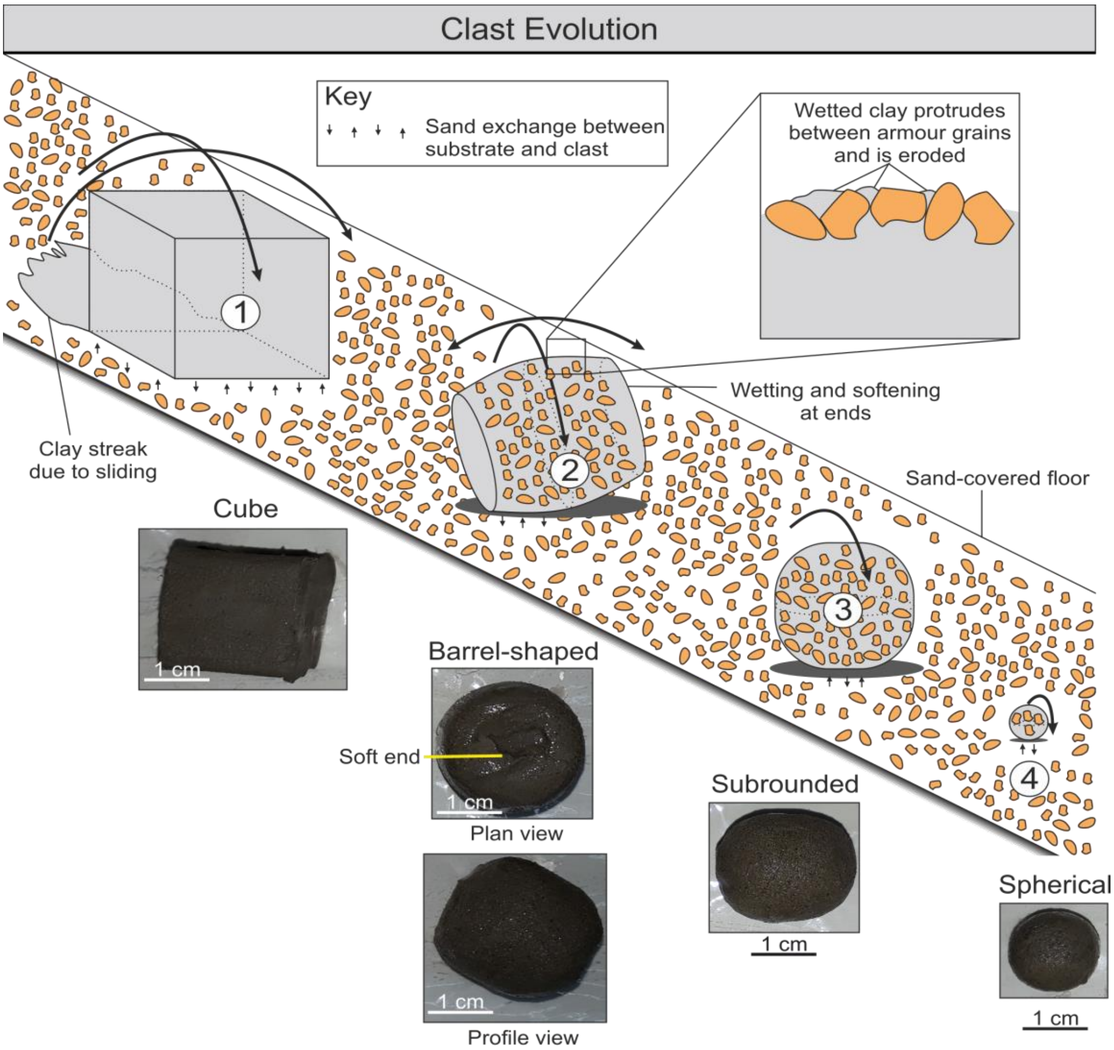

Stage 1: Cube
- Cube free to roll along either axis or slide along the bed
- Sand grains quickly adhere to the periphery of the clast as it rolls

Stage 2: Barrel-shape
- Clast primarily rolls along minor axis
- Exchange of armor grains between the clast and the substrate as wetting occurs between grains
- Wet clay is extruded and eroded between armour grains and plucked as grains fall from clast

Stage 3: Subrounded
- Barrel-shaped clast becomes increasingly spherical as barrel ends are abraded
- Rolling along any axis promotes complete armouring
- Exchange of armour grains and mass loss via extrusion continues

Stage 4: Spherical
- Erosion slows as clast becomes smaller and rounder
- Exchange of armour grains and mass loss via extrusion continues
- Armour remains attached to the clast until it is completely abraded

FIGURE 3: CLASTS AT VARIOUS STAGES OF THEIR EVOLUTION

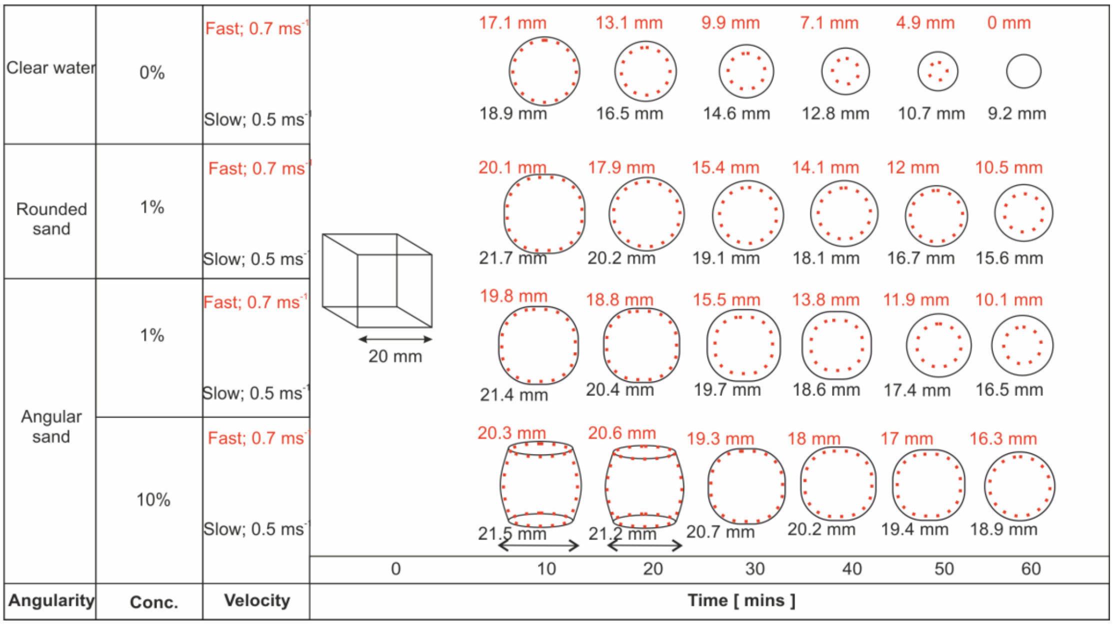

Figure 4: The average shape and length of the longest axis of the clasts through time. Red numbers indicate fast (~ 0.7 ms-1) flow averages, and black numbers indicate slow (~ 0.5 ms-1) flow averages.

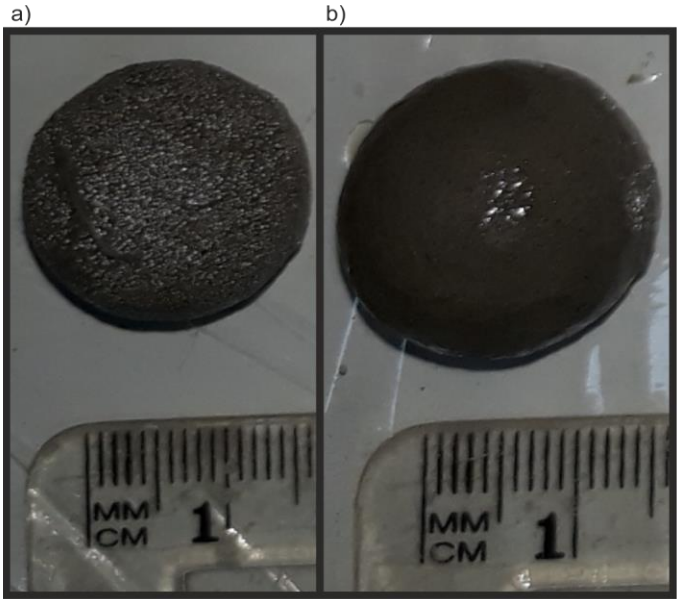

*Figure 5: **A)** A close-up photograph of an armoured clast. **B)** A close-up photograph of an unarmoured clast.*

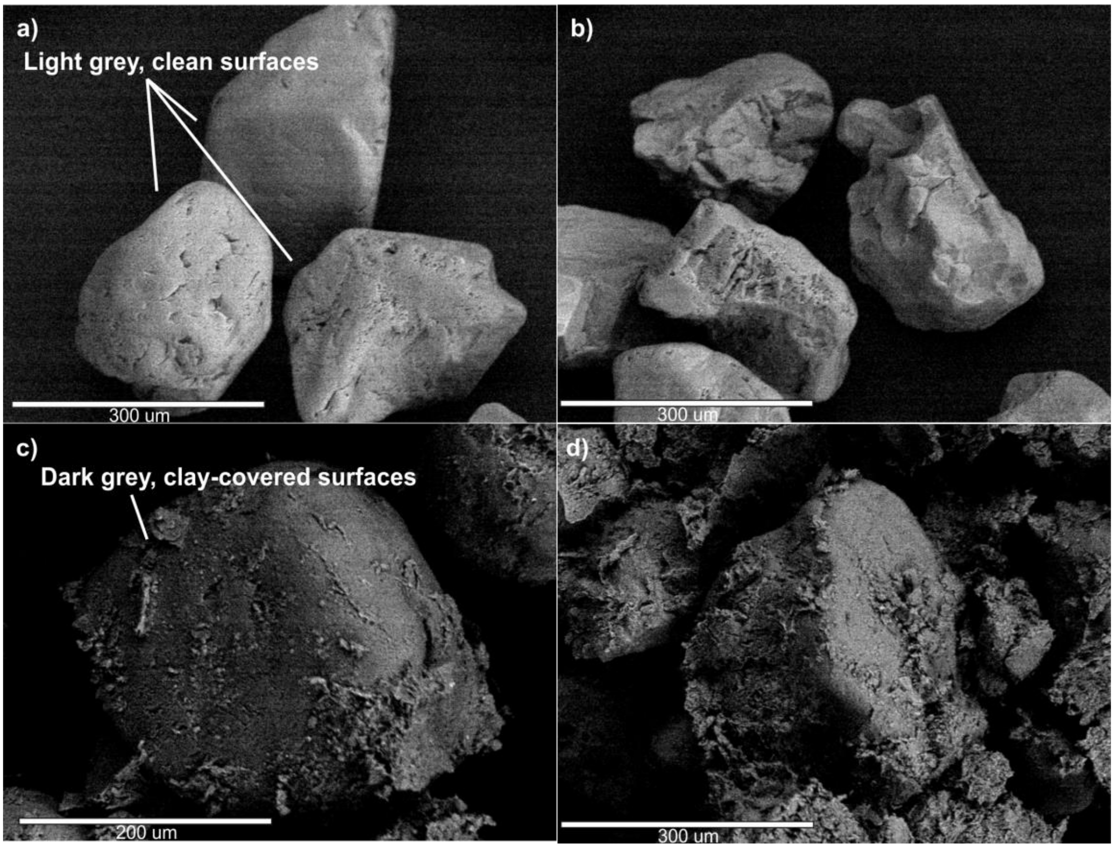

Figure 6: Scanning-electron-icroscope images of angular sediment grain samples. ***A - B)*** *Examples of angular sediment before the experiment,* ***C - D)*** *Examples of angular sediment taken from the periphery of an armoured clast. The grains clearly show clay that has adhered to the surface of the grains.*

3.3.2. Clast Travel Distance

Complete clast disintegration occurred in some, but not all experimental runs by the end of the one-hour measurement period (Fig. 7A, B). When normalized to weight and travel distance, the shape of the disintegration curves were found to be similar for most of the experiments, with the exception of experiments using 10% bulk angular sand (Fig. 7C). Experiments using 10% angular sand display a shallower normalized curve than the other experiments.

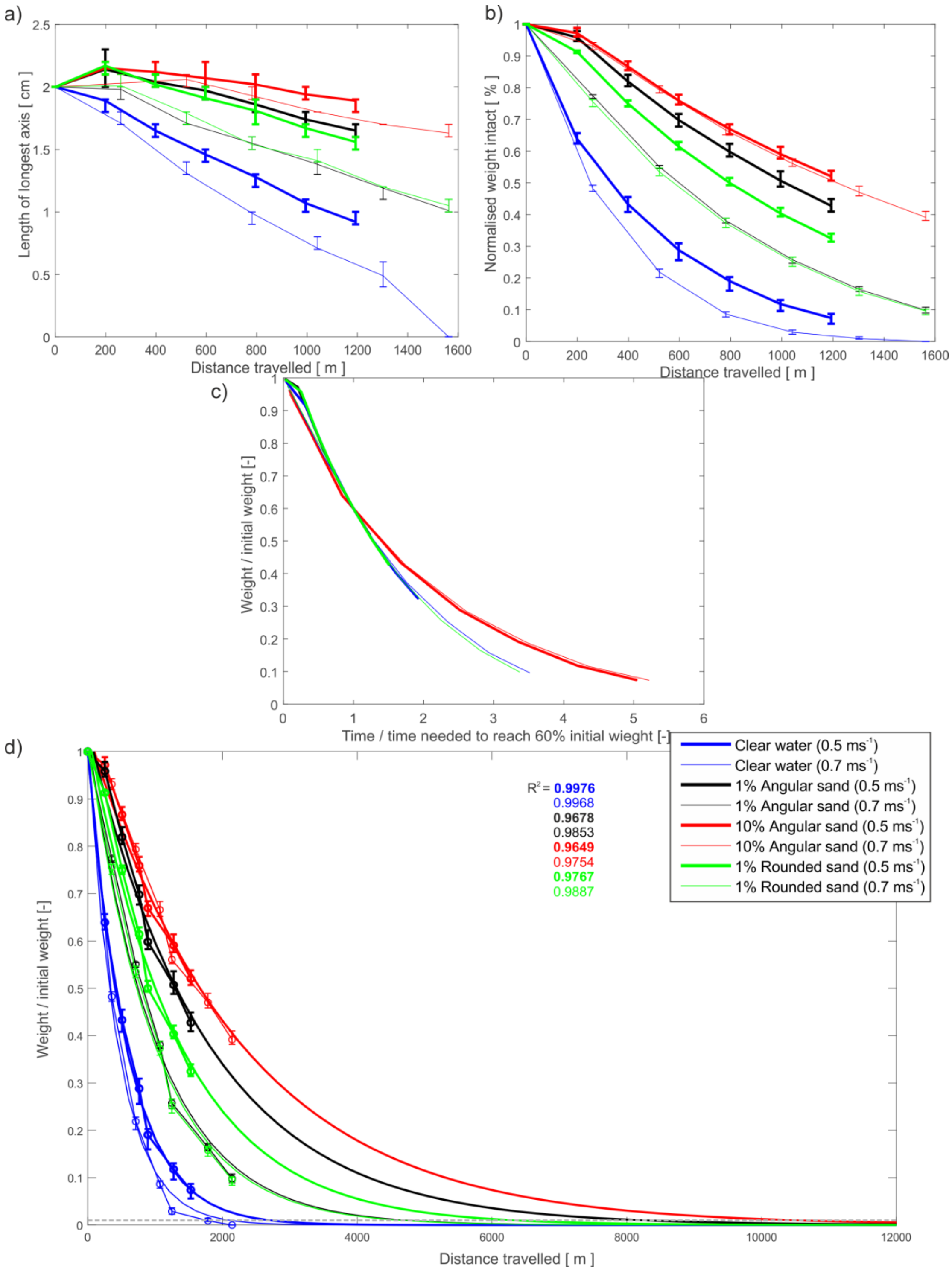

*Figure 7: **A)** The average length of the longest axis plotted against travel distance. **B)** Normalised average showing original clast weight plotted against travel distance. Error bars show the range of measurements. **C)** Normalized distance versus normalized weight showing that abrasion rates are broadly similar. **D)** The extrapolated distance the clasts would travel until they are destroyed by the flow. Extrapolated using an exponential function; exp(-a*x+b). The dashed gray line indicates the last point at which clasts were recovered in the 0.7 ms-1 clear-water experiment, and is used as an approximate travel distance.*

Clasts abraded most quickly in clear-water experiments, where they were gradually but completely destroyed over projected distances of < 2 km. Clay clasts developed armour following the addition of sand to the experiments. The development of armour coincided with a reduction in the rate of abrasion whereby armoured clasts travelled at least twice as far as unarmoured clasts. Abrasion was further reduced by decreasing flow velocity, increasing sediment concentration, and by using angular sand grains (rather than rounded sand grains). At the lowest velocity (0.5 ms^{-1}), at the highest sediment concentration (10%) and by using angular sand grains in the experiment the clasts travelled almost four times farther than unarmoured clasts (Fig. 7).

3.4. Discussion

The experiments show that clay clasts passed through four stages as they abraded: 1) cube-shaped, 2) barrel-shaped, 3) subrounded, and 4) rounded (Figs. 4, 6). Abrasion rate is controlled by flow velocity, bed hardness, and to a lesser extent the angularity of the armouring sand at lower flow velocities. Abrasion was slower and clasts passed through the four stages more slowly when velocity was lower, there was a thicker aggraded sand bed (softer substrate), and angular rather than rounded sediment was used in the experiment. In experiments that included sediment, clasts developed a layer of armour that was one grain thick (Figs. 3, 5). Unarmoured mud-clasts were abraded by a combination of impacting the bed (Bell, 1940; Smith, 1972), and wetting of the clast surface, reducing its shear strength (Smith, 1972), leading to increased likelihood of abrasion or dilution. We infer that an armoured mud-clast would still be able to lose volume via the wetting and abrasion, and the wetting and dilution methods described above, but this would occur only between armour grains, and thus at a lower rate for an unarmoured clast. The wetted clay between the armour grains would be extruded and eroded or diluted. In addition, clay is plucked from the clasts as the sand armour falls away and is subsequently replenished; this is evidenced by the presence of clays on the sand armour in SEM images (Fig. 6). Thus, we show that armouring increases the distance that clasts can be transported over a hard flume floor before they are destroyed, by up to several kilometers. We now discuss the process of mud-clast armouring and the transient nature of the armour observed during the experiments.

3.4.1. Armouring Mechanisms

Here we document that armouring occurs via rolling of cohesive clasts along a sandy substrate. During Stage 2 (barrel shape) of clast evolution the clasts were armoured around the exterior of the barrel, but the barrel tops and bottoms were soft and unarmoured. This indicates that the clasts roll along a preferential axis when not rounded, and that the clasts develop armour only on surfaces that come into contact with the substrate, rather than developing an armour via bombardment with sand grains from suspension. A naturally occurring unarmoured clast of a shear strength similar to that of our clasts may indicate a lack of rolling (i.e., suspension or matrix transport), or rolling along a non-granular bed (e.g., mud).

Our results oppose previous suggestions in fluvial environments that armouring is permanent, that falls away only as clasts become dry, and that armoured clasts abrade only as they impact upon boulders (Bell, 1940). We find that the armour is semipermanent, that clay is extruded and eroded or diluted, and that the individual grains that make up the armour are removed and replenished and remove particles of clay as they do so. We infer the armouring and abrasion mechanism from the presence of clay on the sand particles in SEM images, and from the fact that the clasts are always covered in sand when extracted for measuring yet they decrease in size through time. Therefore, in order to be maintained, the armour must be replenished from a granular substrate. The armouring process is therefore transient, and more dynamic than previously considered.

3.4.2. Armouring and Mud-clast Travel Distances

We now consider why some mud-clasts in natural systems appear to travel farther than those in our experiments, as illustrated by the potentially long-runout Grand Banks turbidity current that occurred in 1929, offshore Newfoundland.

The inferred travel distance of the armoured mud-clasts in the 1929 Grand Banks turbidity current is two orders of magnitude greater (> 400 km) than the findings of our experiments (2 - 12 km). Here we seek an explanation for this apparent discrepancy.

First we consider the size of the mud-clasts in the 1929 Grand Banks event compared to our laboratory experiment. The Grand Banks event transported > 150 km^3 of sediment (Piper and Aksu, 1987) in a series of submarine landslides with shear planes of 5 - 25 m depth (Piper et al., 1999). It is probable that some of the blocks were meters in size, which may have facilitated their long transport distance. However, if we compare our clear-water experiment with a similar experiment by Smith et al. (1972) that used larger clasts, we see that clast abrasion rates are much higher for larger clasts (Fig. 8). Therefore, whilst initial clasts size must have some effect on the distance that a clast can travel, it may not be as important as it first seems.

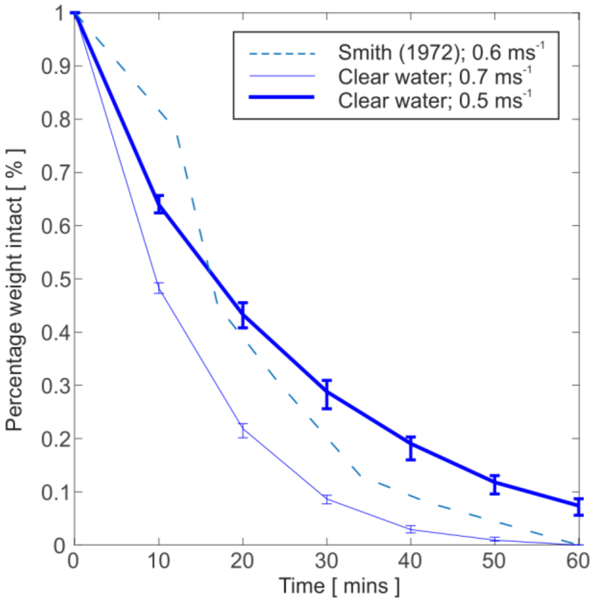

FIGURE 8: COMPARISON BETWEEN THE ABRASION RATE OF CLASTS IN CLEAR-WATER EXPERIMENTS OF SMITH (1972) AND THE CLEAR-WATER EXPERIMENTS PRESENTED HERE. THE CLASTS IN THE SMITH (1972) EXPERIMENT WERE 3 CM X 0.5 CM WHEREAS OUR CLASTS WERE 2 CM CUBOIDS.

Second, we consider the shear strength of the mud-clasts in the 1929 Grand Banks event compared to the clasts in our experiments. The initial water content (Smith, 1972) and the hardness of clasts (Lewin and Brewer, 2002) are important when considering abrasion rates. There are no known shear-strength measurements of clasts in the Grand Banks deposit, but near-seafloor muds around the Grand Banks region and offshore Nova Scotia have been shown to be overconsolidated (Clark and Landva, 1988; Baltzer et al., 1994). The Grand Banks shelf is a glacially modified margin (Piper et al., 1999), thus explaining the presence of highly consolidated seafloor muds due to past glacial loading. Other locations around the world also feature overconsolidated sediments, with an extreme example noted on the UK Continental Shelf where ice loading during the last glaciation has resulted in near-seafloor (< 5 m) undrained shear strengths in excess of 2500 kPa (Aldridge and Carrington, 2010). In addition, the shear plane of the Grand Banks landslide was 5 -

25 m deep (Piper et al., 1999), which is within the region of the overconsolidated muds found on the UK Continental Shelf (Aldridge and Carrington, 2010). The shear strength of the clasts produced during landslide disintegration may therefore have been greater than the shear strength of the clasts used in our experiments (17 - 40 kPa). Experimental studies have shown that higher-shear-strength substrates will resist erosion more than lower-strength ones (Winterwerp et al., 1992, 2012; Schieber et al., 2010; Schieber, 2016). In the same manner, higher shear strengths may therefore improve the durability of mud-clasts and facilitate a longer transport distance of the clasts, as inferred from the Grand Banks deposit.

Fourth, we consider the mode of transport of the mud-clasts in the 1929 Grand Banks event compared to our laboratory experiments. Field evidence suggests that rolling along the bed, rather than being in suspension, is important for promoting clast abrasion (Bell, 1940; Schwab et al., 1996; Talling et al., 2010). Clasts can travel hundreds of kilometers if they are encased in a debris flow (Schwab et al., 1996; Talling et al., 2010). Two mud-clasts were found in cores of the Grand Banks deposit, and both of them were armoured (Stevenson et al., 2018), indicating rolling along a sand-rich bed. The extreme travel distance of clasts in the Grand Banks density current can be explained by the downslope evolution of the density current. The density current began as a debris flow, and remained as such for the first 20 - 35 km of transport (Piper et al., 1999). Clasts in the flow at this stage would likely not have been armoured, but would have been protected by the surrounding debris flow. After the debris flow phase, the density current then transformed on steep slopes into a turbidity current (Piper et al., 1999). The turbidity current was shown to have attained a velocity of up to 19 ms^{-1} (Piper et al., 1999). Such a high velocity is likely to support mud-clasts in suspension, which would mean that they were not rolling during the high-velocity section of the journey. The clasts may have been fully suspended in the high-velocity flow. As the flow began to lose energy and decelerate on the more distal slopes, the clasts would have fallen out of suspension and rolled along the bed. In addition to the sequence of events, the average bulk sediment concentration of the Grand Banks density current is estimated to have been 2.7 - 5.5% (Stevenson et al., 2018). In our experiments we found a flow-averaged concentration of 1% to be suitable in supplying the clasts with sediment to replace dislodged armour particles. The combination of the transforming, fast flow, together with the high average sediment concentration, probably enabled the mud-clasts in the Grand Banks density current to attain their impressive transport distances.

Finally, we consider the nature of the substrate over which the clasts were carried (assuming that they were not necessarily in suspension) as our experiments suggest that bed hardness may affect transport distance. In real-world systems, such as the Grand Banks, the strength of the seafloor substrate is likely to vary and, in places (e.g., where it is muddy), may be considerably softer than the floor of our flume.

To summarize the Grand Banks case study: it is probable that the long travel distances can be explained by the large initial size and high shear strength of the clasts, and the soft nature of the seafloor substrate over which the flow travelled. Furthermore, it is possible that, given the velocity attained by the flow, the clasts were suspended for at least part of their journey, thus reducing their abrasion. It is likely that a combination of these factors resulted in the unusually long transport distances attained by clasts in the 1929 Grand Banks density current.

3.4.3 The Prevalence of Unarmoured Mud-clasts

There are a number of examples of armoured mud-clasts from deep marine settings, but the examples of unarmoured mud-clasts greatly outnumber these. Here we consider why this imbalance exists. The imbalance between armoured and unarmoured clast examples could be due to several reasons. A first reason could be due to the stickiness of the mud; mud-clasts that are very wet (e.g., mud with a high fluid content; Schieber et al., 2010) or clasts that are very hard (e.g., lithified or highly overconsolidated mud; Schieber 2016) may not be able to support an armour layer. A second reason for the relatively common occurrence of unarmoured mud-clasts could be that armour falls away once it can be no longer replenished. As the sediment gravity flow reaches the distal muddy fringes of the turbidite system, it will no longer be replenishing the armour and may simply lose its armour coating due to wetting and/or dilution effects. Furthermore, clasts transported across a soft (i.e., mud) floor would experience a potentially greatly reduced rate of abrasion (particularly compared to the hard flume floor of this study) and may be transported farther or even increase their mass by accreting additional mud, as well as having more opportunity to shed their armour. Finally, the average grain size of the system may be too fine for armouring to occur; mud-clasts can be armoured only by grains coarser than silt (Bell, 1940); if the system is too muddy, armour will not form.

3.4.4. Implications for Interpreting Clast-Bearing Sediment-Density-Current deposits

In this section we discuss how armouring of clasts may control where linked debrites develop, and how armoured mud-clasts may help in identifying linked debrites in outcrop.

Previous studies have identified that turbidity currents commonly transform into debris flows and deposit debrites towards the lateral or distal edges of turbidite systems (Kane and Pontén, 2012; Haughton et al., 2009; Fonnesu et al., 2015, 2016, 2018). However, it can be difficult to determine whether a debrite is part of a hybrid deposit when there is limited outcrop exposure. Distal flow transformation is promoted by the incorporation of clay, which is often associated with disaggregation of mud-clasts (Patacci, Haughton, and Mccaffrey, 2014). Armoured mud-clasts have been found in turbidites (Dasgupta and Buatois, 2012; Fonnesu et al., 2018; Stanley, 1964), hyperpycnites (Ponce and Carmona, 2011), and hybrid deposits (Felix et al., 2009; Haughton et al., 2003; Patacci, Haughton, and Mccaffrey, 2014). The presence of armoured mud-clasts in a debrite indicates up-dip transformation from a turbidity current to a debris flow, because rolling of the mud-clasts along a sandy bed is required in order for the sandy armour to develop (Fig. 9).

Turbidity currents transform into debris flows once a sufficient quantity of cohesive sediment is available in the flow, and once turbulence is low enough for the gelling of clay particles, which typically occurs as the flow decelerates (Baas et al., 2009; Sumner et al., 2009). Our experiments show that armouring reduces the rate of abrasion of mud-clasts and thus would reduce the rate of release of clay into a turbidity current. If a sufficient volume of clasts is present, then armouring could hinder the transformation of turbidity currents, and may contribute to hybrid deposits occurring preferentially in lateral and distal parts of turbidite systems (Fig. 9). We find in our experiments that clast armour is transient and requires replenishment from the substrate. Once the clast-bearing flow reaches the distal reaches of the fan it is likely to encounter mud-rich substrates, and clasts will no longer be able to replenish their armour. This may partly explain why unarmoured rather than armoured clasts are found most often.

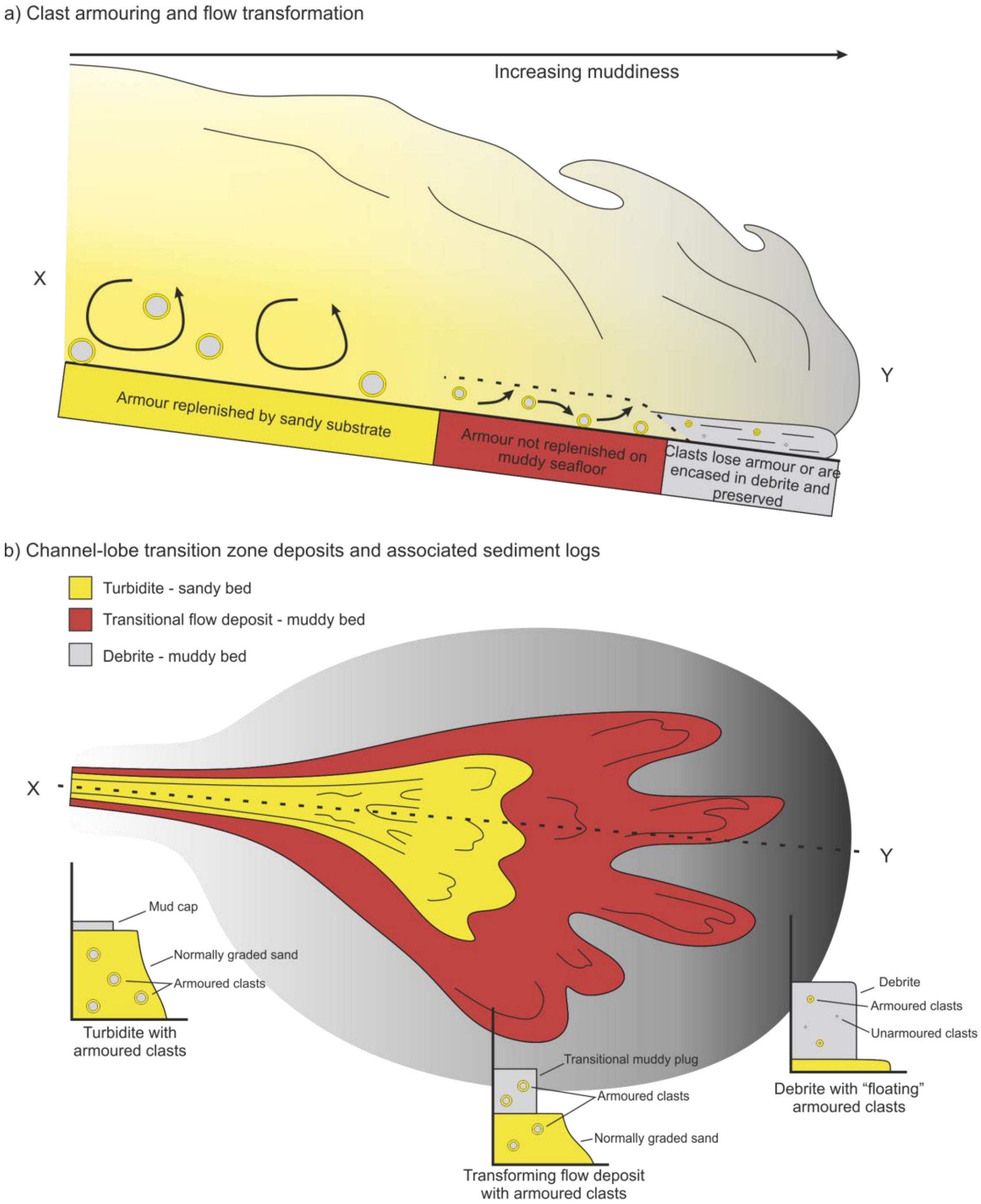

*FIGURE 9: SUMMARY FIGURE SHOWING **A)** A SCENARIO WHERE ARMOURED MUD-CLASTS ARE TRANSPORTED IN A TURBULENT FLOW, THE TRANSFORMATION OF THE FLOW INTO A DEBRIS FLOW, AND **B)** WHERE ARMOUR CAN OR CANNOT DEVELOP ON A SUBMARINE FAN, AS WELL AS THE PRESERVATION OF ARMOURED CLASTS IN THE LINKED DEBRITE.*

3.5. Conclusions

Our first aim was to understand the mechanism(s) by which mud-clasts become armoured and if that armouring is permanent. We find that clasts go through the same four stages of evolution regardless of the development of an armour layer, but the armour layer reduces the rate of abrasion. We provide the first direct evidence that armouring occurs by rolling clasts in a sandy substrate. We also show for the first time that clast armour is transient and undergoes continual replenishment from the bed. Unarmoured clasts may be indicative of a lack of rolling (travelled a short distance, travelled in suspension, or travelled as a floating outsize clast in a debris flow, for example), a lack of available sediment that can form armour (i.e., a muddy bed), or that the clay that forms the clast is too hard to support armour.

Our second aim was to determine how armouring affects clast abrasion and to quantify the distance clasts with and without armour can be transported. Without armour on a hard flume floor, 8 cm^3 cube-shaped clasts disintegrate within two kilometers. Following the addition of a 1% concentration of suspended sediment, an armour develops around clasts that more than doubles the distance they can travel. We find that the rate of abrasion further declines with increasing sediment concentration, thus increasing travel distance by more than four times the distance achieved by unarmoured clasts. A sandy substrate can help to improve the transport distance of a clay clast by providing an armour of sand. However, natural systems can have muddy substrates, which we did not consider in these experiments. Unarmoured clasts may travel farther on muddy rather than sandy substrates because the muddy substrate causes less erosion to the clast than a hard substrate. Additional experiments are required to investigate the transport distances achievable by mud-clasts over a muddy substrate, as well as of armoured mud-clasts over a muddy substrate.

Our final aim was to consider the implications of clast armouring for interpreting deep-water deposits and flow transformations. Our results suggest that the presence of armoured clasts in debrites may serve as a tool for identifying linked debrites. Our results also suggest that armouring may delay flow transformation and be partly responsible for the common occurrence of flow transformation in distal lobe environments at the point that the seabed becomes muddy, and therefore the sand armour can no longer be replenished.

Chapter 4: Could electrical resistivity tomography be used to measure dense basal layers in annular flumes?

Hizzett, J. L.[1,2], North, L.[2], Clare, M. A.[2], Cartigny, M. J. B.[3], Sumner, E. J.[1]

[1] Ocean and Earth Science, National Oceanography Centre Southampton, University of Southampton, European Way, Southampton, SO14 3ZH, United Kingdom.
[2] National Oceanography Centre, University of Southampton Waterfront Campus, European Way, Southampton, SO14 3ZH, United Kingdom.
[3] Departments of Earth Science and Geography, University of Durham, Durham, DH1 3LE, United Kingdom.

Abstract

Sediment density flows, like turbidity currents, flow along the ocean floor at often-high velocities and pose a hazard to submarine pipelines and telecommunications cables. Key to our understanding of how these flows work is improving our understanding of their internal structure – particularly near the seafloor where they can interact with seafloor infrastructure. The internal structure of sediment density flows remains poorly understood due to technological limitations; in particular, conventional measurement techniques cannot measure the high (> 20% by volume) sediment concentrations that may occur at the base of these flows. Field observations suggest that dense basal layers are common, but we have not yet been able to quantify their sediment concentrations. Even in experimental studies it has proven difficult to measure sediment concentration in dense basal layers because the physical presence of instruments can disrupt the sediment concentration profile. Here, we use a rotating annular flume to test whether a modified Electrical Resistivity Tomography technique could measure sediment concentrations in an experimental dense basal layer, and without disrupting the flow structure. The modified Electrical Resistivity Tomography method shows promise for measuring high sediment concentrations. However, the accuracy of the inversion of the measured resistivity to a sediment concentration profile depends to some degree on initial assumptions made by the user. Future studies will need to test these assumptions for a range of flows before this technique can be applied more widely.

4.1 Introduction

Turbidity currents are potentially fast (up to 20 ms$^{-1;}$ Piper et al., 1999), turbulent, sediment-laden gravity currents that travel along the ocean floor. These fast flows pose a threat to the ever-increasing amount of seafloor infrastructure such as submarine telecommunication cables and pipelines (Zakeri, 2009). It is the basal part of turbidity currents in particular that poses a hazard to submarine infrastructure, because the higher sediment concentration and consequently the highest velocities occur close to the base of these flows (Bruschi et al., 2006). Due to the vigorous nature of the flows and the high sediment concentrations, direct measurements of these dense basal layers are extremely rare (Paull et al., 2018). The absence of measurements of dense basal layers makes it difficult to validate existing models that describe the dynamics of these dense basal layers.

The potential thickness of dense basal layers has been debated (Hiscott, 1994; Sohn, 1997). Experimental work has shown that dense basal layers, driven by shear from an overriding low-density turbidity current, are on the order of millimetres to centimetres thick (Gao, 2008; Hiscott, 1994; Sumner et al., 2008; Cartigny et al., 2013). Fundamentally, the thickness of this layer depends on the Shields number (Shields, 1936) of the flow, and a theoretical thickness limit has been suggested to be on the order of tens of grain diameters (Hiscott, 1994), which is consistent with experimental observations (Dohmen-Janssen and Hanes, 2002; Sumer, 1996; Wilson, 1987). However, field observations show that relatively dense layers at the base of turbidity currents could be metres thick (Sumner and Paull, 2014; Hughes Clarke, 2016; Symons et al., 2017; Paull et al., 2018), and are typically overlain by a more dilute layer (Felix and Peakall, 2006; Symons et al., 2017). It may be that the metres-thick dense basal layer in natural flows is not driven by shearing of the overriding flow, but rather that these layers are self-driven and act as a modified grain flow (Lowe, 1976; Cartigny et al., 2013). Measuring the sediment concentration in dense basal layers is key to testing these contradicting hypotheses.

There are presently no sediment concentration measurements of dense basal layers of turbidity currents in experiments or on the ocean floor. Optical backscatter instruments (Hughes Clarke et al., 2014; Xu et al., 2014) or acoustic inversion techniques (Azpiroz-Zabala et al., 2017) have been used to measure sediment concentration in deep-sea turbidity currents. However, these techniques are not capable of measuring sediment concentrations of several percent by volume or higher, which characterise powerful turbidity currents (Stevenson et al., 2018) and dense basal layers (Bagnold, 1954; Postma et al., 1988). Sediment concentration measurements of experimental turbidity currents typically rely on intrusive techniques such as syphoning (Sequeiros et al., 2010; Baas et al., 2011; Pohl et al., 2020) or conductivity probes (Dick and Sleath, 1991; Dohmen-Janssen, 2002; Puleo et al., 2010; Lanckriet et al., 2014), which are problematic because these instruments disrupt the vertical structure of the dense basal layer. Experimental work suggests that close to the bed sediment concentrations decrease linearly upwards from 50-70% to 20-30%, whereas above this linear layer the concentration decreases with a power-law profile (Lanckriet et al., 2014). These trends are consistent with results of numerical models (Jiang, 1995) and laboratory investigations in open channel environments (Dick and Sleath, 1991).

Electrical Resistivity Tomography (ERT) is a non-intrusive technique that is able to measure high sediment concentrations of up to 60 - 70% (equivalent to a packed sedimentary bed; Schlaberg et al., 2006). The ERT technique is a scaled down and modified version of the technology used to measure density variation or structures in the Earth’s subsurface (Noel and Xu, 1991). Field resistivity measurement techniques use an array of electrodes to measure subsurface resistivity (Noel & Xu, 1991). Current is passed between a pair of electrodes and the differential potential (the amount of work an electrical current has to do to move between electrodes) across a pair of electrodes is measured (given in volts). The measured voltage then requires inversion into the desired units (e.g., density or sediment concentration). The voltage measured across a pair of electrodes is proportional to the density (or sediment concentration) of the object being measured, such as the Earth’s subsurface or a sediment concentration in a water column (Dyakowski et al., 2000). Inversion is a troublesome aspect of the ERT technique, because ERT is an ill posed problem (Polydorides and Lionheart, 2002), meaning that multiple solutions can be drawn from a single dataset. Conventional inversion software packages are inefficient and poorly model the electrodes in the inversion, which led to the development of the open-source Electrical Impedance and Diffuse Optical Reconstruction Software (EIDORS) project (Polydorides and Lionheart, 2002). ERT arrays have been used in the past for measuring settling sediment suspensions. In those cases, the electrode arrays were linear and laid flat on the floor of the tank or U-shaped and curved around the walls of the settling tank to produce 2D cross-sections of conductivity (Schlaberg et al., 2006). The flat array of Schlaberg et al., (2006) recorded considerable interference, which was caused by stratification within the settling clay suspension used in their experiments. The U-shaped array showed conductivity distortions when an object was placed towards the edges of the array. The conductivity signal became weaker towards the middle. These irregularities and distortions were due to an increased sensitivity resulting from the irregularly spaced electrodes used in the experiment (Schlaberg et al., 2006). ERT has not yet been used to measure a moving fluid, but holds potential for being a non-intrusive technique for measuring the high sediment concentrations found at the base of turbidity currents.

The overall aim of this chapter is to evaluate the ERT method, including the inversion software, for measurement of high concentration flows in a flume. We achieve this aim by answering the following questions:

- First, the chapter aims to test the sensitivity of the inversion from voltage to sediment concentration, by examining how variation of the parameters set within the inversion software affects the shape and absolute values of the resulting sediment concentration profiles.
- Second, the resulting sediment concentration profiles are compared with previous studies to validate the sediment concentration profiles produced by the experiments.
- Third, this chapter comments on the feasibility of measuring sediment concentrations in dense basal layers with the non-invasive ERT technique for measuring sediment concentrations above 20%, and further modifications to the method are suggested.

4.2 Methodology

In this section we begin by describing and explaining our choice of flume tank used in the experiments. We outline the flow velocity measurement apparatus, and the sediment used. We then introduce the modified ERT system and explain the experimental procedure. Finally, we explain how the resistivity inversion algorithm works.

An annular flume (Fig. 1) was used for this study because it enables generation of fast flows with a dense basal layer (Sumner et al., 2008). Annular flumes are ring-shaped flumes that generate a shear flow using rotating paddles (Booij, 2003). There are different types of annular flumes, some in which only the top ring and paddles rotate (e.g., Thompson et al., 2003) and others in which, in addition, the base counter rotates (e.g., Sumner et al., 2008). The annular flume used in this study has a counter rotating base and has a radius of 0.53 m. The channel is 0.33 m deep to the top of the paddles and 0.145 m wide, holding 160 litres of water (Fig. 1a). The paddles are 10 cm long. Two motors drive the base and the paddles for a user-defined duration, and can generate flows of up to 3.5 ms^{-1} (Sumner et al., 2008). The motors can be set to accelerate or decelerate linearly at a user-defined rate. The base counter-rotates to reduce secondary circulation of the fluid caused by centrifugal acceleration of the rotating flow (see below).

The advantage of using annular flumes over lock-exchange flume tanks (Felix et al., 2005; Felix & Peakall, 2006) is that annular flumes can generate much higher flow velocities (many metres per second rather than centimetres per second) and thus suspend sediment of a similar size to that found in nature (Bath Enright et al., 2017). Another advantage of using annular flumes over straight recirculating flumes (Baas and Best, 2008) is that you can recirculate the sediment-water mixture without destroying the dense basal layer and the structure (e.g. stratification) of the flow (Sumner et al., 2008).

The primary disadvantage to using an annular flume is the generation of a secondary circulation cell during experimentation. Secondary circulation effects disrupt the cross-channel shear stress profile, and thus the concentration, velocity, and turbulence profiles. Rotation of the flume generates a centrifugal effect on the flow and causes superelevation of the water towards the outside of the flume tank (Booij, 2003; Sumner et al., 2008). The hydrostatic pressure at the outer wall is therefore higher than the inner wall, causing water to flow from the outer wall to the inner wall (Booij, 2003). This heterogeneity in hydrostatic pressure generates a circulation cell that is inwardly directed at the base of the channel and outwardly directed towards the surface of the flow. In the counter-rotating annular flume used here a counter-rotating base is combined with the rotating paddles to generate a secondary circulation cell that flows in opposition to the secondary circulation cell caused by the paddles, thus reducing the effect of the basal secondary flow (Booij, 2003). The disadvantage of the counter-rotating flume is that is typically needs a calibration to link a rotation velocity of the flume to a flow velocity. Here we bypass the need for such calibration by installing a velocity sensor in the flume (Fig. 1).

4.2.1 Experimental Apparatus

To create the sediment suspension in the flume, we used 20 kg of angular kiln-dried sand with a D_{50} of 250 µm (Fig. 2). We used this quantity for sediment to avoid the formation of a stationary bed at our selected velocities. The velocities were selected to reproduce field-scale bed shear stresses of about 0.1 m/s (Straub and Mohrig, 2008; Cartigny et al., 2013). We chose fine to medium sand in these experiments because such grain sizes are commonly found in nature and used in other flume experiments (Sumner et al., 2008).

A single Metflow UVP-DUO 1MHz uDvp (ultrasonic Doppler velocity profiler) transducer with an active diameter of 20 mm was used to measure flow velocity. We used the flow data to calculate velocity profiles ~150 mm downstream of the ERT (Fig. 1b, Table 1). We use two different velocities in the experiments; 0.7 ms^{-1} and 0.75 ms^{-1} for comparison. These velocities were chosen because they produced shear velocities similar to those measured in turbidity currents; $u^* \approx 0.09 - 0.1$ ms^{-1} (Cartigny et al., 2013), and were able to suspend most of the sediment whilst allowing a thin (centimetre-thick) basal layer to develop. The uDvp transducer was fixed 160 mm above the bed and set at an incidence angle of 60° normal to the flow (De Leeuw et al., 2016). The transducer recorded flow velocity at 299 depths through the water column, and the sampling interval was set to its minimum of 173 ms (Table 1).

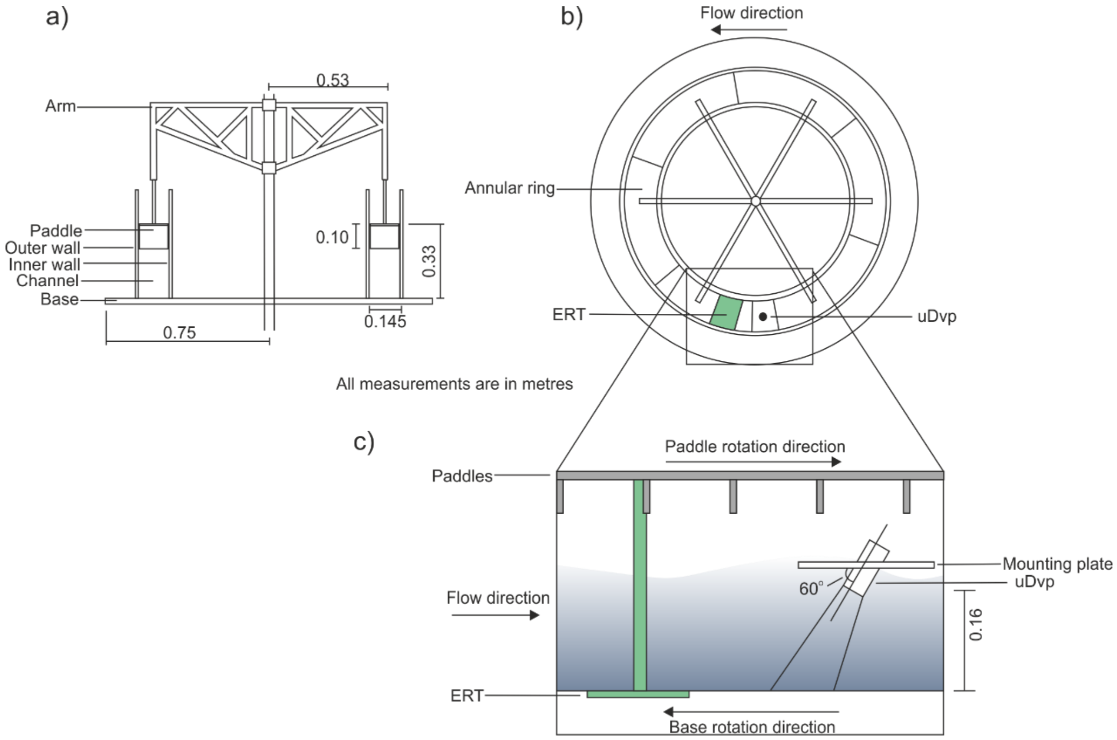

Figure 1: **a)** Schematic of the annular flume used in the experiment, **b)** aerial view of the annular flume with locations of the ERT and UDVP (after Sumner et al., 2008), **c)** in-profile configuration of the ERT and UDVP.

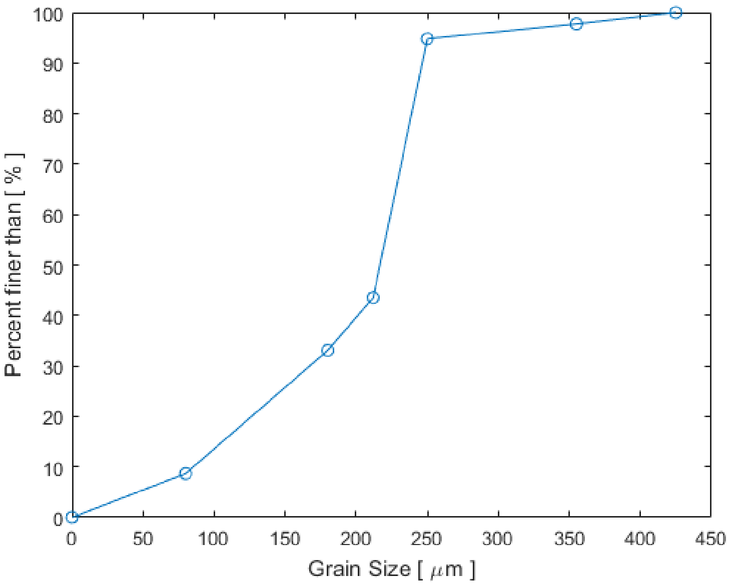

Figure 2: Grain size distribution in a 153g subsample of sand from the sand used in the experiments, measured using sieves.

Active diameter of instrument	20 mm
Number of bins	299
Number of profiles	1200-1400
Sampling speed	173 ms
Sound speed	1500 m/s
Velocity resolution	8.719 - 10.068 mm/s
Minimum velocity	-1288 to -1116 mm/s
Maximum velocity	1107 to 1278 mm/s
Max. Depth	252 mm
Probe Angle	60°
Beam divergence half-angle	2.2°
Probe Frequency	1 MHz
Number of cycles	30
Number of repetitions	512
Minimum measurement distance	3.75 mm
Maximum measurement distance	227.25 mm
Bin length	0.75 mm
Bin width	22.5 mm

Table 2: The parameters of the uDvp used in the experiments.

Sediment concentration was inferred with a modified version of an Electrical Resistivity Tomography (ERT) array. The ERT was positioned ~20 cm upstream of the uDvp, so that the ERT measurements were not disrupted by the presence of the uDvp (Fig. 1c). The ERT probe lay flush with the bed and walls of the flume and did not disrupt the flow stratification profile (Fig. 3).

4.2.2 Electrical Resistivity Tomography Design

The ERT system used in this experiment is a modified version of a rock physics ERT system developed at the National Oceanography Centre Southampton (North et al., 2013). Previous experiments used regularly spaced linear arrays of electrodes but highlighted that electrode sensitivity was highest when spaced closely together (Schlaberg et al., 2006). In this experiment the ERT electrode array consists of two sub-arrays of 16 parallel gold strip electrodes each, placed back to back, with logarithmic spacing (Fig. 3). The electrodes are closely spaced in the centre of the flume, which increases the measurement sensitivity of the expected high sediment concentration close to the bed in the centre of the flume. Focusing measurements in the centre of the flume also reduces the influence of the walls and the intersection at the flume wall and flume base where measurement distortions (thus concentration profile distortions) occur. Electrodes at the periphery of the array enable measurement of sediment concentration higher up in the water column due to the arcuate path followed by electricity between the probes (Fig. 3). The parallel arrangement of strip electrodes in the planar ERT electrode array helps to average out any variations in the downstream direction.

Tomography is typically used to produce 2D cross sections of the spatial variation in resistivity or conductivity. Irregular spacing of electrodes has been shown to produce a distorted visual representation of resistivity, due to the higher sensitivity where electrodes are closely spaced (Schlaberg et al., 2006). Here we use tomography to produce a one-dimensional sediment concentration profile.

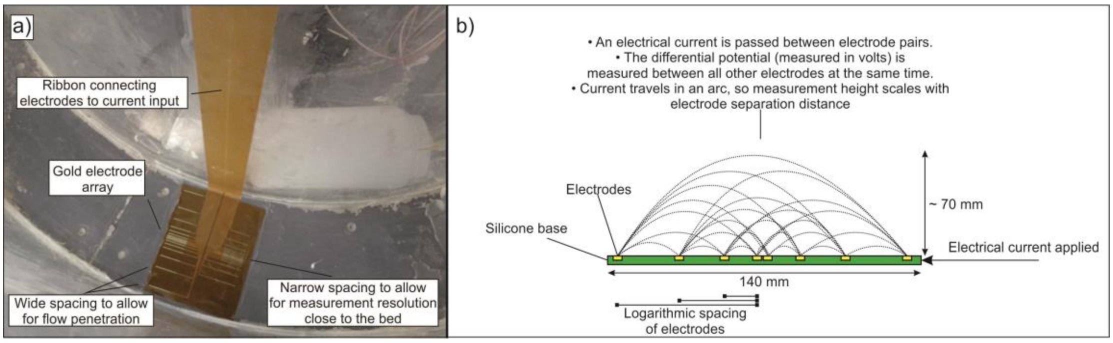

Figure 3: **a)** The ERT array used in this experiment in place in the annular flume, **b)** Illustration of the ERT highlighting electrical pathways during experiments.

The electrode pairs of the ERT system measure the differential potential (V) at a set current (I), which is converted to resistivity R using $R = V/I$. The measured resistivity then has to be converted into sediment concentration. Linear and power-law models have been proposed and tested to convert resistivity to sediment concentration (Landauer, 1952; Dick and Sleath, 1991; Lanckriet et al., 2013). Here we use the well-tested linear model (Dick and Sleath, 1991; Lanckriet et al., 2013):

$$\frac{r_f}{r_m} = 1 - C \tag{2}$$

where, r_f is the resistivity of the ambient fluid, r_m is the resistivity of the fluid-sediment mixture and C is the sediment concentration. A total of 208 voltage measurements were taken per cycle. The technique used to invert resistivity into a sediment concentration profile is described in Section 4.2.4.

4.2.3 ERT Calibration

The ERT was calibrated by installing the ERT in the annular flume and measuring the resistivity of seawater (2.2 ohms). The sand volume was then added to the annular flume and the resistivity of the packed bed (3.2 ohms) was measured. The seawater (i.e., 0% sediment concentration) and packed bed (i.e., maximum possible sediment concentration) were used to calibrate the linear model (Eqn. 2).

4.2.4 Experimental Procedure

During each run of the experiment the ERT and the uDvp were secured in the tank along with a 1% volumetric concentration of the kiln dried sand. The UDVP was set recording flow velocity before the annular flume was rotated. Once the flume had reached its maximum rotational velocity the ERT was activated from an external console. Resistivity and flow measurements were captured synchronously for a duration of five minutes. Average flow velocity was calculated, and an average sediment concentration was inferred using an inversion algorithm (See section 4.2.5).

4.2.5 Resistivity Inversion Algorithm

In this chapter, we aim to measure *sediment concentration* profiles within the flow; however, the ERT method measures the *differential potential (in volts)* between two electrodes. This is a common problem in geophysics where interpretation (e.g. physical properties of buried sediments) is required from remotely sensed measurements of the subsurface (Vardy et al., 2017). In such scenarios, an inverse model is often employed to provide the closest match between a theoretically computed dataset and the measured data (Provenzano et al., 2017). An inversion uses the actual results of measurements (e.g. differential potential), converted to resistivity, to infer the values of the parameters that characterise the system (e.g. sediment concentration; Tarantola, 2005)). We employ an inversion and an optimisation routine to iteratively reduce the difference between a predicted resistivity computed from a modelled distribution of sediment concentrations and our measurements of resistivity.

Here, theoretically predicted resistivity values are produced by a forward model using EIDORS software (Electrical Impedance and Diffuse Optical Tomography Reconstruction Software). EIDORS is open-source software that has been developed by research and industry communities that analyse a wide range of tomography and resistivity data (http://eidors3d.sourceforge.net/).

4.2.3.1 How the inversion was implemented

The implementation of the inversion is a modified version of the ERT inversion developed by North et al., (2013). The novel part is the implementation of the sediment concentration profile and its associated constraints.

Step 1 – Estimate the resistivity that would result from a theoretical sediment concentration profile (Forward Model)

First, a 3D finite element model was constructed using a mesh with approximately 10,000 elements. Within the model an initial theoretical sediment concentration profile was assumed, which was then inverted to define a ‘calculated’ resistivity series for comparison with the measured resistivity series. Several constraints were placed on sediment concentration at this stage to obtain a stable sediment concentration inversion. First, spatial variability in the sediment concentration was constrained to only vary with depth. Secondly, vertical sediment concentration profiles were constrained to comply with several boundary conditions: 1) the sediment concentration cannot be negative; 2) the sediment concentration cannot exceed 70%; and 3) sediment concentration profile is specified by a prescribed number of inflection points. Based on the initial sediment concentration profiles, the forward model calculates a series of resistivities for each electrode pair for a given applied current.

Step 2: Compile observed measurements from the ERT flume experiment (as-measured resistivity)

Second, a ‘measured’ resistivity series was compiled by converting the measured differential potential between each electrode pair into resistivity. The conversion from voltage to resistivity was achieved using: $R = V/I$. This produced a series of apparent resistivities with individual values corresponding to each electrode pair.

Step 3: Compute the difference between the predicted resistivity (Forward Model) and the measured resistivity

Third, we compared the resistivity from the Forward Model (Step 1) with the direct resistivity measurements (Step 2) to determine how closely the measured results match with the forward model. This comparison was defined as the *error* and was quantified by:

$$Error(i) = \sqrt{\sum_{i=1}^{i=208} (calculated\ resistivity(i) - measured\ resistivity(i))^2 + \alpha T} \qquad (3)$$

Here the smoothing term, αT, was employed to penalise non-smooth solutions as resistivity inversions can often yield initially highly irregular profiles. T quantifies the irregularity of the solution using Tikhonov regularisation, a method widely used in ill-posed problems with non-unique solutions (Wiik et al., 2015). The α is a scaling factor that was set manually with the aim of balancing the regularisation information and the measured data so that one is not over-represented in the output concentration profile (Wiik et al., 2015). Therefore low α values would yield little smoothing, but too low an α value would introduce instabilities into the inversion. This penalty was necessary to ensure that subsequent iterations of the forward model are not based on an initially unrealistic output and is used routinely in resistivity inversions (Dickin and Wang, 1996; Lavoué et al., 2010). In our case we used an α value of $1\text{x}10^{-4}$ because it produced smooth sediment concentration profiles.

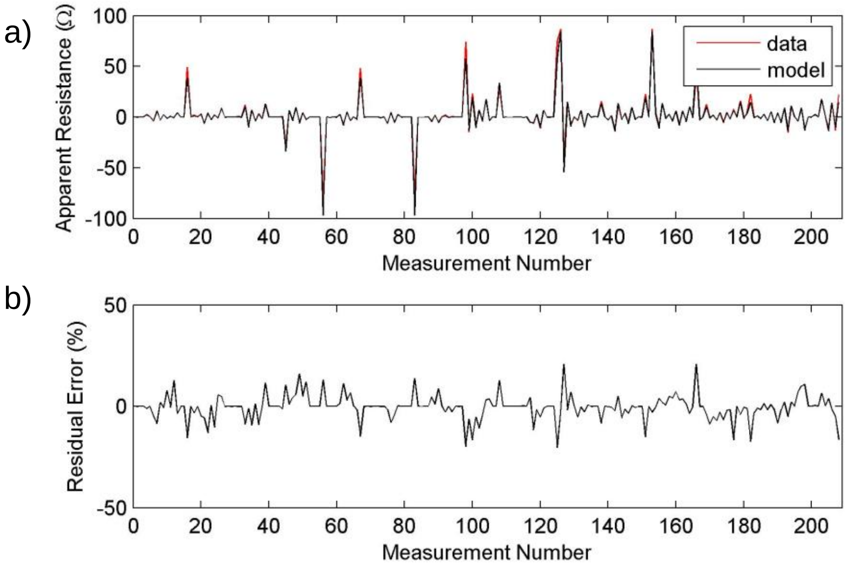

FIGURE 4: A) DIFFERENCE BETWEEN APPARENT RESISTANCE OF THE MODEL SERIES AND DATA SERIES AFTER THE ADDITION OF 3 INFLECTION POINTS USING AN α VALUE OF 1X10-4. B) RESIDUAL ERROR AS A PERCENTAGE DIFFERENCE BETWEEN THE MODEL AND DATA SERIES.

Step 4: Reduce the error using an optimisation routine

In order to find the output of the forward model that most closely matches the real measurements from the ERT flume experiment, we then implemented an optimisation routine in Matlab, known as the Nelder-Mead Simplex (Nelder and Mead, 1965; Marwala, 2010). This method has previously been successfully used in resistivity inversions to hunt for the lowest degree of error of a modelled output through an iterative variation of parameters (Hoverstein et al., 1982; Lambot et al., 2006). During the optimisation routine, some parameters were fixed; 1) the minimum sediment concentration - defined as clear water; 2) the height of the top and base of the flow; 3) the height and number of inflection points in the concentration profile. This optimisation provides a revised theoretical sediment concentration that is fed back into the Forward Model (Step 1) as another iteration of the model was run.

Step 5: Iterate Steps 1 to 4 to provide the solution that best matches the measured data

Steps 1 to 4 were repeated 20 times for the first inflection point and 50 times (the number of repetitions in this case was arbitrary) for each subsequent inflection point, and the error value (Eqn. 3) was computed to determine the model performance (Fig. 5). To test the model sensitivity, the model was run for one, two and three inflection points in the profile.

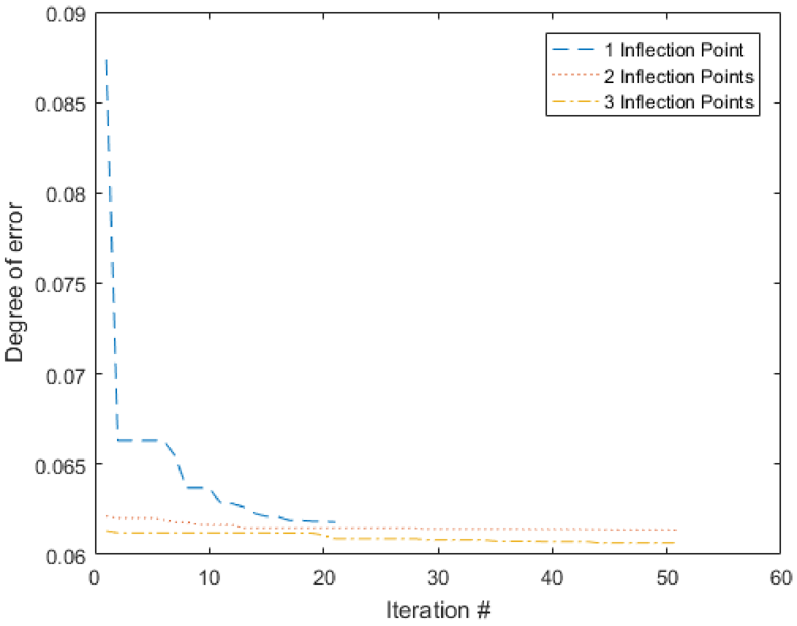

FIGURE 5: DECLINING DEGREE OF DIMENSIONLESS ERROR AS DEFINED IN EQUATION 3 BETWEEN THE MODEL AND THE DATA WITH EACH ITERATION OF THE INVERSION ALGORITHM.

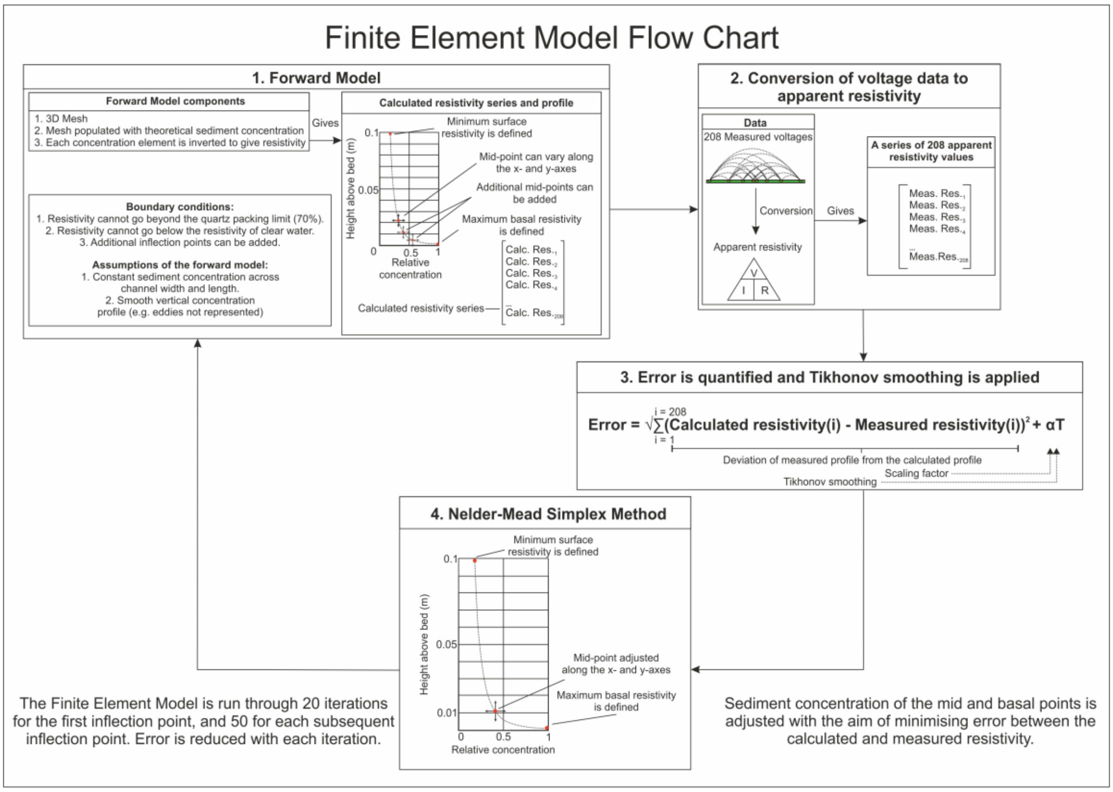

FIGURE 6: FLOW CHART DEPICTING THE PROCESS OF THE FINITE ELEMENT MODEL.

4.2.4 Calculation of the Particle Shields Number

In this paper we estimate the Shields parameter of each flow to compare the measured thickness of the dense basal layer with previous measurements and predictions (Wilson, 1987; Sumer et al., 1996; Dohmen-Janssen, 2002) as a way of validating the thickness reported by the ERT data inversion. The Shields parameter (τ_*) is defined as (Shields, 1936):

$$\tau_* = \frac{\tau}{(\rho_s - \rho) g D_{50}} \tag{4}$$

where τ is bed shear stress, ρ_s is the density of sediment, ρ is the fluid density, g is the gravitational constant (9.81 $ms^{-1}s^{-1}$), and D_{50} is the average grain size (250 µm). We estimate bed shear stress from the velocity profile using the least squares regression method (Yu and Tan, 2006):

$$\tau = k \frac{n \sum u_i \ln z_i - \sum u_i \sum \ln z_i}{n \sum \ln^2 z_i - (\sum \ln z_i)^2} \tag{5}$$

where k is the von Kármán's constant (0.405), n is the number of measuring points, u_i is the velocity measurement, and z_i is the height of the velocity measurement (Yu and Tan, 2006). All points must be within the logarithmic boundary layer (Yu and Tan, 2006).

4.3 Results

The overall aim of this study is to evaluate the ERT method for the measurement of dense basal layers in a flume. The first part of the results focuses on the sediment concentration profiles and their response to varying the prescribed number and location of the inflection points used in the inversion. The second part presents the velocity profiles and the associated bed shear stresses.

4.3.1 Sediment Concentration

Overall, we see that below the velocity maximum the sediment concentration decreases almost linearly with height from the bed, and above the velocity maximum the sediment concentration is constant with height. The ERT records a similar thickness for the dense basal layer (region of high sediment concentration) between the high and low velocity experiments (Fig. 7). The experiments are characterised by a similar (~ 63%) sediment concentration at the bed. The inflection points are plotted at the same height between experiments. The lowermost inflection point indicates a difference of ~6 % sediment concentration between the high velocity (~ 31%) and low velocity (~ 36%) experiments (Fig. 7b). Above the dense basal layer, the sediment concentration remains relatively constant for both experiments (< 3%). The low velocity experiments are characterised by relatively lower suspended sediment concentrations (~ 2%) compared to the high velocity experiments (~ 3%).

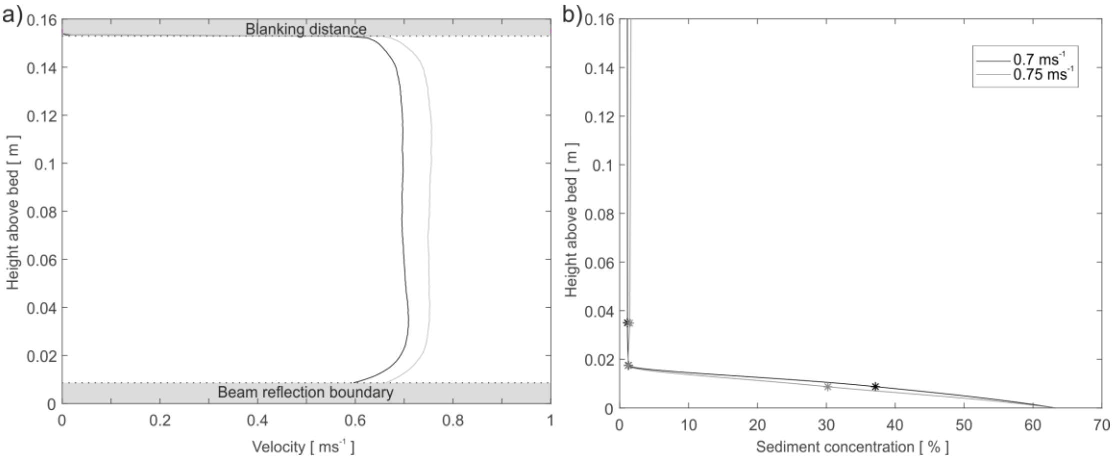

FIGURE 7: A) FLOW VELOCITY PROFILE MEASURED DURING EACH EXPERIMENT, B) SEDIMENT CONCENTRATION PROFILES MEASURED DURING EACH EXPERIMENT USING THREE INFLECTION POINTS IN THE INVERSION. THE INFLECTION POINTS ARE SHOWN AS STARS.

The first dependency analysed here is how the sediment concentration profiles respond to varying the number of inflection points in both the high velocity (0.75 ms^{-1}; Fig. 8a) and the low velocity experiments (0.7 ms^{-1}; Fig. 8b). If only a single inflection point is specified in the inversion, then the sediment concentration near the bed stays below the sediment concentration of a stationary bed, while the sediment concentration higher up in the flow remains relatively high (8 - 10%). When three inflection points are specified in the inversion the sediment concentration profile is characterised by a higher gradient, where the sediment concentration just above the bed approaches that of a stationary bed (60 - 70%), while the concentration higher up in the flow falls back to a few percent. Further addition of inflection points does not lead to any marked difference in the profile shape (Fig. 8).

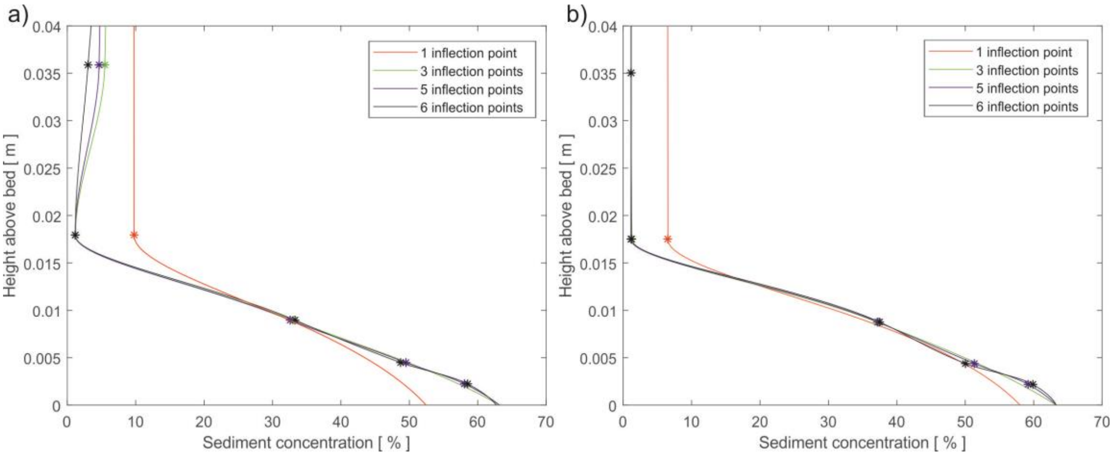

Figure 8: a) Sensitivity analysis of the number of inflection points for the high velocity (0.75 ms^{-1}) experiment, b) Sensitivity analysis of the number of inflection points for the low velocity (0.7 ms^{-1}) experiment. Inflection points are highlighted by stars.

The second dependency analysed here is how the sediment concentration profiles respond to varying heights of three inflection points (Table 2; Fig. 9). The densest part of the flow (above 30 - 40% concentration; Fig 9) is the most stable and sediment concentration estimates vary by up to 6%, with thickness estimates varying by up to 2.5 mm for any fixed height. The interface between the dense basal layer and the relatively dilute body of the flow are most sensitive to changes in inflection point height and vary by up to ~ 30% (e.g., Fig. 9b) sediment concentration, with thicknesses varying by up to 5 mm for any fixed height.

Anchor point [m]	Inflection point heights [m]	
0.035	0.018	0.070
	0.020	0.061
	0.015	0.082
0.025	0.013	0.050
	0.014	0.044
	0.011	0.059
0.017	0.009	0.034
	0.010	0.030
	0.007	0.040
0.01	0.005	0.020
	0.006	0.018
	0.004	0.023

Table 3: Positions of the inflection points in Figure 8. The anchor inflection point is the central inflection point. The anchor point is first divided to give one inflection point, and then multiplied by the same value to give another, totalling 3 inflection points for each sediment concentration profile.

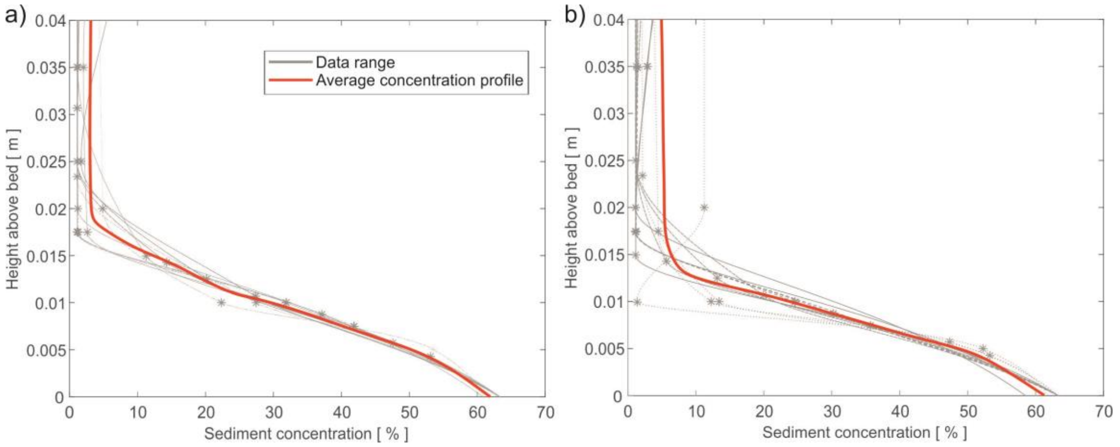

*Figure 9: Sensitivity analysis of the height of the inflection points highlighting the average sediment concentration profile (orange line) of the **a)** low velocity, and **b)** high velocity experiments. The data ranges are all variations of inflection point heights when using 3 inflection points (see table 2).*

4.3.2 Velocity Profiles and Bed Shear Stresses

During the experiment it was observed that most of the sediment was in suspension with a stationary layer a few grains thick on the base of the flume. The flow recorded by the uDvp shows a similar average velocity structure for each run (Fig. 9). There is a ~20 mm region at the base of the flow, below the velocity maximum, where the flow velocity begins to decay, and an upper region where the velocity is constant with height (Fig. 9a).

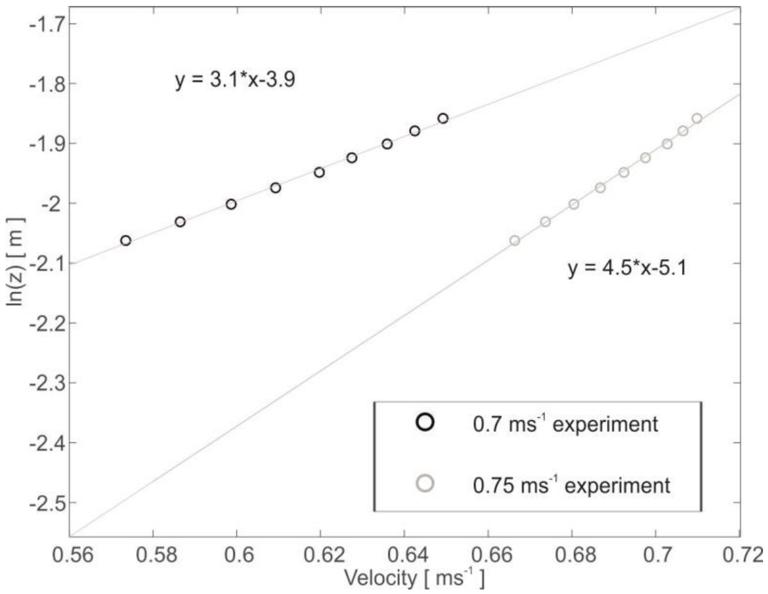

FIGURE 10: LINEAR CORRELATION FOR THE BOUNDARY LAYER OF THE VELOCITY PROFILES: $R^2 = > 0.99$.

From the velocity profiles we calculate the shear stress and a shear velocity (Eqn. 5), from which we can derive the Shield's number (Eqn. 4). The shear velocity was calculated to be between $u^* \approx 0.09 – 0.1$ ms^{-1}, and the Shields number was calculated to be between ~2.1 – 2.7 for the experiments presented here. We also estimate the level of any potential stationary bed by plotting the common logarithm (log10) of the height above bed against the velocity in the logarithmic layer (Fig. 10). From this we plot a linear regression to find the y-intercept to estimate the position of the bed (Van Rijn, 2011). The logarithm of the height above the bed correlated well ($R^2 > 0.99$) with the velocity at that height, indicating that our shear stress estimation was accurate. The linear regression to estimate bed height indicated the absence of a stationary bed, with an intercept of ~ 0 mm in the high velocity (0.75 ms^{-1}) experiments, and an intercept of ~ 0.1 – 0.3 mm in the low velocity (0.7 ms^{-1}) experiments (keeping in mind the D_{50} of 0.25 mm). This estimate is in agreement with visual observations.

4.4 Discussion

In this section we discuss the sensitivity of the sediment concentration profiles to the number and height of the inflection points specified in the inversion. Second, we compare the dense basal layer thickness recorded in our experiments with the thickness recorded in other experiments, and in nature. Third, we consider whether the ERT is a suitable apparatus for measuring dense basal layers in flows generated in a flume tank and provide suggestions for future modifications and further tests.

4.4.1 Sensitivity of the Sediment Concentration Profiles to Inversion Software Parameters

The first aim of this chapter is to test how sensitive the inversion from voltage to sediment concentration is to variations in the different parameters in the inversion software. Our results show that the inversion is not very sensitive to alterations in the number of inflection points defined in the software (Fig. 8) but is more sensitive to their position in the profile (Fig. 9). We find it is best to have at least three inflection points in the region of interest to work towards producing a sensible sediment concentration profile (Fig. 8). However, it is important that those inflection points are in the area with the highest sediment concentration gradient (Fig. 9; i.e., the top of the dense basal layer). Adjusting the height of the inflection points a number of times will produce a range of sediment concentration profiles from which an average can be drawn (Fig. 9). In these experiments we estimate the thickness of the dense basal layer using visual observations of the dense basal layer. If an approximation of the thickness of the dense basal layer is not available, then it would be best to initially introduce more than three inflection points at a range of heights in the profile. The additional inflection points at different positions will produce physically unrealistic variation (i.e., a region of relatively low sediment concentration beneath a region of relatively high sediment concentration or vice versa) in the sediment concentration profile but will indicate roughly the location where the changes in sediment concentration are most pronounced. Once the top level of the dense basal layer is known, then adding 3 - 5 inflection points around that level is likely to provide the best results.

4.4.2 Comparison of Sediment Concentration Profiles with Previous Measurements and Theory

The second aim of this chapter is to compare the results of the experiments to theoretical sediment concentration profiles, as well as measured sediment concentration profiles from previous experiments. First, we use the flow properties to predict dense basal layer thickness and compare theoretical predictions with our results, and then we compare our results to previously published sediment concentration profiles measured using alternative equipment.

Here we use flow properties to empirically estimate the height of the dense basal layer. Bed thickness estimates indicated no static bed, or maybe a very thin static bed (up to 0.3 mm, or 1 grain). We find the Shields parameter of the flows in this study to be 2.1 and 2.7, for the low and high velocity experiments respectively. Higher shear stress should give a thicker dense basal layer as more of the bed depth is mobilised (Wilson, 1987; Sumer, 1996; Dohmen-Janssen and Hanes, 2002). Based on the experimental results of Wilson (1987), Sumer (1996), and Dohmen-Janssen and Hanes (2002), our Shield's parameter values should produce a dense basal layer of approximately 20 - 40 grain thicknesses (Fig. 11). A D_{50} of 250 µm would give a 5 - 10 mm thick sheet flow layer. We record an average dense basal layer thickness of approximately 15 mm in the low velocity experiment, and 13 mm in the high velocity experiments (Fig. 9), which we define using the 9% concentration criteria of Bagnold to define the top of the dense basal layer (Bagnold, 1954). The decrease in the thickness of the basal layer with an increased bed shear stress is not consistent with previous models. The difference can be explained by the fact that sediment concentrations higher up in the flow (i.e., above the dense basal layer) are greater during the high velocity run. The decrease in thickness of the dense basal layer could be explained by a lower sediment availability at the base of the flow (i.e., a hard flume floor), in other words the higher velocities produce a less stratified sediment concentration profile. A 15 mm and 13 mm basal layer with a D_{50} of 250 µm would give a dense basal layer thickness of 60 and 52 grains (respectively), which is higher than predicted by previous studies. Our observations therefore indicate a dense basal layer that is slightly thicker than theoretically predicted. Turbulent 'sweeps' created by the paddles in the top of the flow could explain the thicker basal layer. Alternatively, the ERT technique may mask the top of the layer in such a way that it appears thicker. However, the measured thickness of the dense basal layer is consistent with the visual observation of the layer being about 0.02 m thick.

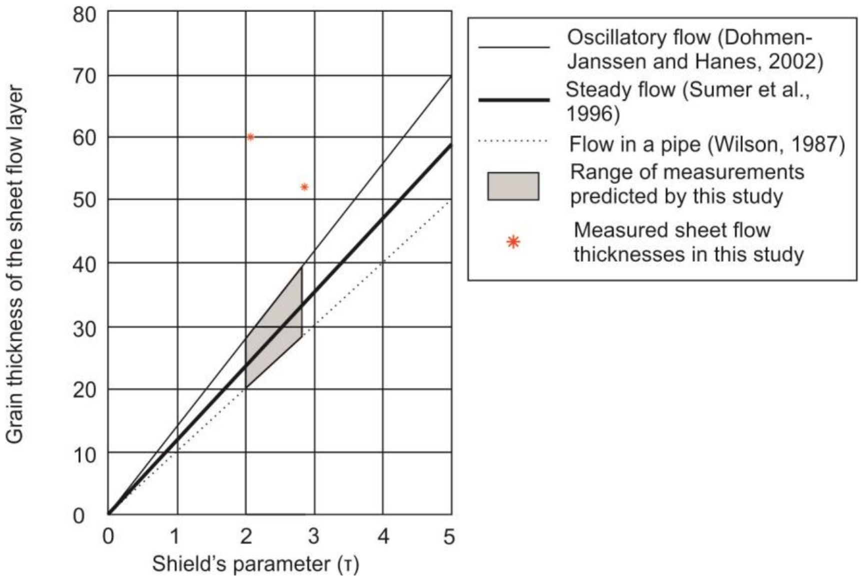

FIGURE 11: THE LINEAR RELATIONSHIP BETWEEN THE SHIELD'S PARAMETER AND THE GRAIN THICKNESS OF THE SHEET FLOW LAYER (After Wilson, 1987; Sumer et al., 1996; Dohmen-Janssen, 2002).

In addition to using flow properties to predict dense basal layer thickness, we can compare our results to other measured dense basal layers. Dense basal layers have been measured using conductivity probes in oscillatory flows (O'Donoghue and Wright, 2004; Lanckriet et al., 2014). The measured profiles have shown that sediment concentration decays abruptly with height above the bed from 50 - 70%, almost linearly, until around 20-30% concentration, and then decay with a power-law shape (Lanckriet et al., 2014). Our average profile is markedly similar to this description in that the average profile decays almost linearly to around 20-30% sediment concentration where the gradient changes (Fig. 9).

4.4.3 Suitability of the ERT for Measuring Dense Basal Layers in a Flume

The third aim of this chapter is to determine how suitable the ERT technique is for measuring dense basal layers in annular flumes. For a measuring device to be suitable, it must be both practical and reliable. This section outlines the achievements of the modified ERT design and the processing software, as well as offering some suggestions for future experiments.

The ERT was simple to install in the annular flume. The array lay flush with the bed of the flume tank and did not disrupt the flow. Other methods used to measure sediment concentration in fluid environments such as conductivity probes, or sediment syphons may be relatively impractical (Dick and Sleath, 1991), disrupt the flow (Sequeiros et al., 2010), or are not necessarily intended for monitoring fast fluid flows (Bolton et al., 2002; Lanckriet et al., 2014). Despite success in our relatively short-duration experiments, the gold electrodes of the ERT are rather fragile, and may suffer from abrasion in prolonged flows. The Printed Circuit Board (PCB) used by Schlaberg et al., (2006) with its tinned copper electrodes were hardier materials and may be more resilient to abrasion by prolonged or faster flows. Furthermore, the ERT is housed on electrical ribbon that must be fixed to a surface; this works well in a flume where the flume floor is stationary, but may be difficult to reliably implement in experiments (or natural settings) with a mobile bed. Assuming the ERT is fixed to a metal plate, scour around the plate will modify the flow and destabilise the ERT over time.

The ERT shows a dense basal layer in the region where the dense basal layer was observed, where it was inferred by the flow properties, and was close to the range predicted by other studies. Validation of the sediment concentration with an existing measurement technique, such as an ultrasonic high concentration meter (UHCM) or sediment syphons, would provide further validation of the results. UHCM and sediment syphons are routinely used in laboratory experiments to characterise sediment concentration although their physical presence may disrupt the flow (e.g., Felix et al., 2005; Felix and Peakall, 2006). A UHCM or sediment syphons could be used to compare the average concentration at a fixed height, and perhaps guide a control point in the finite element model. Validation would provide another measure to test the reliability of the measurements of the ERT presented here.

4.4.4 Suitability of the Processing Software

Here we use the open source software EIDORS v3.6. EIDORS is open for modification to make the inversion suitable for the purpose but requires considerable experience with electrical systems as well as with Matlab itself in order to use it effectively. However, being able to modify the source code in Matlab can also be viewed as a benefit because one can fully test the software to establish the sensitivity of the inversion to the modification of different parameters (in this case the number and position of the inflection points as needed to produce reasonable sediment concentration profiles from within a dense basal layer).

4.4.5 Wider Application of the Results and Recommendations for Future Studies

We find a relatively dense (up to ~65% concentration), thin (~13 - 15 mm) basal layer that is driven by a dilute overlying turbulent flow in all of the experiments. Previous studies have argued that the dense basal layer produced by a shear flow is indeed limited to millimetres regardless of flow scale (Wilson, 1987; Hiscott, 1994; Gao, 2008; Cartigny et al., 2013; Lanckriet et al., 2014; Patel et al., 2015). Here we show that under shear velocities of $u^* \approx 0.09 – 0.1$, which are comparable to natural flows and implies that shear velocity operates independently of scale (Straub and Mohrig, 2008; Cartigny et al., 2013), we generate dense basal layers of millimetres in thickness. This means that flows that are observed to generate a similar shear velocity to those recorded in these experiments would likely also be accompanied by a similar stratification and sediment concentration profile. Therefore, flows that are accompanied by a dense basal layer on the order of metres in thickness are unlikely to be driven by shear from the overlying flow. It is likely that the dense basal layer is the driving force and main component of the flow (e.g., Sumner and Paull, 2014; Hughes Clarke, 2016; Paull et al., 2018) and is likely to behave like a modified grain flow (Lowe, 1976; Cartigny et al., 2013).

Future studies may wish to explore the dynamics of thicker dense basal layers with a higher sediment concentration than the ones we simulate here, similar to those found in nature. This would further address the disagreement regarding the thickness of dense basal layers in turbidity currents. Those studies should not use an annular flume or any type of flume that implements a shear flow. A shear flow will always generate a basal layer on the order of millimetres to centimetres in thickness. An annular flume is useful for testing equipment in the development phase, but measurements of the concentration and velocity structure of natural turbidity currents are needed to overcome the incompatibility of shear-driven flume tanks, and the scaling issues of other experiments such as lock-exchange experiments (De Leeuw et al., 2016).

Chapter 5: Conclusions and future work

5.1 Conclusions

The aim of this thesis was to investigate how sediment density flows interact with the seafloor, and how this interaction can alter flow behaviour, and ultimately deposit characteristics. The chapters presented were targeting at specific research questions. The outcomes of this research are outlined in this section.

5.1.1. How does the trigger mechanism of the sediment density flow control seafloor interaction and flow evolution?

In chapter 2, I posed three questions: (1) which is the most common trigger mechanism for turbidity currents? (2) Which trigger mechanism generates turbidity currents that rework the most sediment and thus have the greatest effect on delta sculpting? And, (3) which trigger mechanism produces the longest runout flows and carries the most sediment to the lobes at the end of submarine channels?

The most common trigger mechanism for turbidity currents on the Squamish River delta during the study period was related to sediment settling from dilute (hypopycnal) river plumes (plume-triggered). Previous work suggested that landslides are the most common trigger of turbidity currents on river deltas, but we find this to not be the case. During the three-month survey period, more turbidity currents were triggered from settling river plumes than by landslides. No relationship was observed between trigger mechanism and flow run-out; however, the turbidity currents triggered by river plumes were found to be the most erosive. While both small and large submarine landslide-triggered flows were capable of reaching the lobe, plume-triggered flows were found to deliver the most sediment to the lobe (>60%) during the survey period. This study highlights the importance of previously under-appreciated settling from river plumes as a trigger for powerful and long run-out turbidity currents.

5.1.2. How do sediment density flows entrain fine cohesive sediment from the seafloor?

In Chapter 3 I posed three questions: 1) What are the mechanism(s) by which mud clasts become armoured and is that armouring permanent? 2) How does armouring affect clast abrasion, and what distance can clasts with and without armour be transported? And, 3) what are the implications of clast armouring for flow transformations and the interpretation of deep-water deposits?

The experiments document the first direct evidence that armouring occurs by rolling clasts in a sandy substrate and show that clast armour is transient, undergoing continual replenishment from the bed. Unarmoured clasts may be indicative of a lack of rolling (travelled a short distance, travelled in suspension, or travelled as a floating outsize clast in a debris flow, for example) or a lack of available sediment that can form armour (i.e. a muddy bed), or that the clay that forms the clast is too hard to support armour.

The experiments also show that, without armour on a hard flume floor, an 8 cm^3 cube-shaped clasts disintegrate within two kilometers. However, following the addition of a 1% concentration of suspended sediment, armour develops around clasts that more than doubles the distance they can travel. We find that the rate of abrasion further declines with increasing sediment concentration, thus increasing travel distance by more than four times the distance achieved by unarmoured clasts. A sandy substrate can help to improve the transport distance of a clay clast by providing an armour of sand. However, natural systems can have muddy substrates, which we did not consider in these experiments. Unarmoured clasts may travel farther on muddy rather than sandy substrates because the muddy substrate causes less erosion to the clast than a hard substrate. Additional experiments are required to investigate the transport distances achievable by mud-clasts over a muddy substrate, as well as of armoured mud-clasts over a muddy substrate.

Our results suggest that the presence of armoured clasts in debrites may serve as a tool for identifying linked debrites. Our results also suggest that armouring may delay flow transformation and be partly responsible for the common occurrence of flow transformation in distal lobe environments at the point that the seabed becomes muddy, and therefore the sand armour can no longer be replenished.

5.1.3. A novel design of electrical resistivity tomography for measuring dense near-bed layers in flume tanks

In Chapter 4, the overall aim was to evaluate the ERT method, including the inversion software, for measurement of high concentration flows in a flume. This was achieved by answering the following questions: 1) The chapter aims to test the sensitivity of the inversion from voltage to sediment concentration, by examining how variation of the parameters set within the inversion software affects the shape and absolute values of the resulting sediment concentration profiles. 2) The resulting sediment concentration profiles were compared with previous studies to validate the sediment concentration profiles produced by the experiments. 3) The chapter comments on the feasibility of measuring sediment concentrations in dense basal layers with the non-invasive ERT technique for measuring sediment concentrations above 20%, and further modifications to the method were suggested.

The sensitivity analysis of the inversion software showed that while the resultant sediment concentration profile is sensitive to the number and position of the inflection points imposed by the software, the height of the dense basal layer varies by +/- 2.5 mm of the average, with an average thickness of ~15 mm in a shear flow.

Our dense basal layer compared well with previously reported sheet flows. A Shields number between 2 and 2.7 with a D_{50} of 250 μm would give a predicted dense basal layer thickness of 20-40 granular thicknesses (5-10 mm). While our thickness is higher than the predicted thickness, it is on a similar order.

The ERT proved practical to install, being that it only required adhesive and did not visibly disrupt the flow profile. However, it is not clear how durable the design of the ERT hardware may be when used for prolonged periods. Our ERT uses gold electrodes printed on a ribbon cable. Other designs use tinned copper electrodes printed on PCB, which may be more rugged than the design we used. Furthermore, the ribbon cable would be difficult to deploy in settings with a mobile bed where a hard flume floor was not available for adhesion. Validation of the results using predictive tools worked well, but the method would benefit from further validation with sediment syphons or a UHCM to further test the reliability of the method. The EIDORS software offered the freedom to modify parameters that may otherwise be hidden in commercial software packages. However, the software was not simple to use and requires considerable experience with electrical systems as well as Matlab itself to be used effectively.

5.2 Future work

This section highlights potential areas for future work as a result of the chapters of this thesis.

5.2.1 Field monitoring of other river deltas

The plume settling mechanism is an under-appreciated trigger for sediment density flows, and it is still poorly understood. Results in this thesis highlight the importance of the plume trigger in generating long runout, erosive flows, at least on short (3-4 month) time scales. Improving our understanding of how the trigger works may prove valuable in furthering our understanding of river delta evolution as a whole.

The repeat bathymetric surveys of the Squamish River delta provided valuable insights into the frequency of different triggers, as well as the erosiveness and runout of the resultant sediment density flows. At the moment the dataset is the only one that exists that records successive bathymetric signatures of sediment density flows in such detail. It would be interesting to compare the results from the Squamish River delta with a similar study in another location. Likewise, it would be useful and interesting to compare the trigger against the runout and erosiveness with another active site where the triggers are different to the ones at Squamish (e.g. hyperpycnal flow in a lake).

5.2.2 Abrading clasts with different properties and different flow parameters

These experiments provided insights into the evolution of clay clasts and the importance of armour for transporting mud clasts long distances. However, there are other factors that may assist clast travel distances that the experiments did not explore. For example, is initial clast size important? Would a larger clast break up in the same way that the clasts in these experiments did? Would differently-shaped (i.e. larger, more/less angular) sand grains have a different affect on the rate of clast abrasion? How would a clay of a greater or lesser shear strength fare in a similar experiment?

5.2.3 Refining the ERT

In Chapter 4 I use the novel ERT design to infer the sediment concentration and thickness of the dense basal layer of a turbulent flow. However, the method is not without limitations, which are outlined in Section 4.4.3. At present the inverse problem of converting resistivity to a sediment concentration profile remains ill-posed. Until the problem of converting resistivity to sediment concentration is improved, the solution posed by the inversion technique remains non-unique although is within a narrow range (+/- 5 mm on a dense basal layer 13 - 15 mm in height). It would be invaluable to reliably measure the sediment concentration at the base of a sediment gravity flow without disturbing the flow path (i.e. with a further improved ERT).

Appendices

APPENDIX 1: BATHYMETRY PROCESSING MATLAB SCRIPT

```
clear all
close all



direc = dir('*.txt')
%%

for e = 1:93
    e
%% user imput
Vthst=0.4;        % specify contour threshold
filename= direc(e).name;       % specify the filename to be loaded

% Vthvec=[-Vthst*1000 -Vthst*5 -Vthst*3 -Vthst -Vthst/20 Vthst/200 Vthst/200 Vthst/20 Vthst
Vthst*3 Vthst*5 Vthst*1000];
Vthvec=[-Vthst*100  -Vthst Vthst/20  Vthst Vthst*20  Vthst*100];



%% import the raw data

daylabel=filename(6:8);        % extract three numbers that indicate the last day of the difference map
channellabel=filename(9);       % extract channel label

% import the difference map data (DM)
delimiter = ' ';
startRow = 7;
formatSpec =
'%f%f%f%f%f%f%f%f%f%f%f%f%f%f%f%f%f%f%f%f%f%f%f%f%f%f%f%f%f%f%f%f%f%f%f
%f%f%f%f%f%f%f%f%f%f%f%f%f%f%f%f%f%f%f%f%f%f%f%f%f%f%f%f%f%f%f%f%f%f%f
%f%f%f%f%f%f%f%f%f%f%f%f%f%f%f%f%f%f%f%f%f%f%f%f%f%f%f%f%f%f%f%f%f%f%f
%f%f%f%f%f%f%f%f%f%f%f%f%f%f%f%f%f%f%f%f%f%f%f%f%f%f%f%f%f%f%f%f%f%f%f
%f%f%f%f%f%f%f%f%f%f%f%f%f%f%f%f%f%f%f%f%f%f%f%f%f%f%f%f%f%f%f%f%f%f%f
%f%f%f%f%f%f%f%f%f%f%f%f%f%f%f%f%f%f%f%f%f%f%f%f%f%f%f%f%f%f%f%f%f%f%f
%f%f%f%f%f%f%f%f%f%f%f%f%f%f%f%f%f%f%f%f%f%f%f%f%f%f%f%f%f%f%f%f%f%f%f
%f%f%f%f%f%f%f%f%f%f%f%f%f%f%f%f%f%f%f%f%f%f%f%f%f%f%f%f%f%f%f%f%f%f%f
```

```
%f%f%f%f%f%f%f%f%f%f%f%f%f%f%f%f%f%f%f%f%f%f%f%f%f%f%f%f%f%f%f%f%f%f%f
%f%f%f%f%f%f%f%f%f%f%f%f%f%f%f%f%f%f%f%f%f%f%f%f%f%f%f%f%f%f%f%f%f%f%f
%f%f%f%f%f%f%f%f%f%f%f%f%f%f%f%f%f%f%f%f%f%f%f%f%f%f%f%f%f%f%f%f%f%f%f
%f%f%f%f%f%f%f%f%f%f%f%f%f%f%f%f%f%f%f%f%f%f%f%f%f%f%f%f%f%f%f%f%f%f%f
%f%f%f%f%f%f%f%f%f%f%f%f%f%f%f%f%f%f%f%f%f%f%f%f%f%f%f%f%f%f%f%f%f%f%f
%f%f%f%f%f%f%f%f%f%f%f%f%f%f%f%f%f%f%f%f%f%f%f%f%f%f%f%f%f%f%f%f%f%f%f
%f%f%f%f%f%f%f%f%f%f%f%f%f%f%f%f%f%f%f%f%f%f%f%f%f%f%f%f%f%f%f%f%f%f%f
%f%f%f%f%f%f%f%f%f%f%f%f%f%f%f%f%f%f%f%f%f%f%f%f%f%f%f%f%f%f%f%f%f%f%f
%f%f%f%f%f%f%f%f%f%f%f%f%f%f%f%f%f%f%f%f%f%f%f%f%f%f%f%f%f%f%f%f%f%f%f
%f%f%f%f%f%f%f%f%f%f%f%f%f%f%f%f%f%f%f%f%f%f%f%f%f%f%f%f%f%f%f%f%f%f%f
%f%f%f%f%f%f%f%f%f%f%f%f%f%f%f%f%f%f%f%f%f%f%f%f%f%f%f%f%f%f%f%f%f%f%f
%f%f%f%f%f%f%f%f%f%f%f%f%f%f%f%f%f%f%f%f%f%f%f%f%f%f%f%f%f%f%f%f%f%f%f
%f%f%f%f%f%f%f%f%f%f%f%f%f%f%f%f%f%f%f%f%f%f%f%f%f%f%f%f%f%f%f%f%f%f%f
%f%f%f%f%f%f%f%f%f%f%f%f%f%f%f%f%f%f%f%f%f%f%f%f%f%f%f%f%f%f%f%f%f%f%f
%f%f%f%f%f%f%f%f%f%f%f%f%f%f%f%f%f%f%f%f%f%f%f%f%f%f%f%f%f%f%f%f%f%f%f
%f%f%f%f%f%f%f%f%f%f%f%f%f%f%f%f%f%f%f%f%f%f%f%f%f%f%f%f%f%f%f%f%f%f%f
%f%f%f%f%f%f%f%f%f%f%f%f%f%f%f%f%f%f%f%f%f%f%f%f%f%f%f%f%f%f%f%f%f%f%f
%f%f%f%f%f%f%f%f%f%f%f%f%f%f%f%f%f%f%f%f%f%f%f%f%f%f%f%f%f%f%f%f%f%f%f
%f%f%f%f%f%f%f%f%f%f%f%f%f%f%f%f%f%f%f%f%f%f%f%f%f%f%f%f%f%f%f%f%f%f%f
%f%f%f%f%f%f%f%f%f%f%f%f%f%f%f%f%f%f%f%f%f%f%f%f%f%f%f%f%f%f%f%f%f%f%f
%f%f%f%f%f%f%f%f%f%f%f%f%f%f%f%f%f%f%f%f%f%f%f%f%f%f%f%f%f%f%f%f%f%f%f
%f%f%f%f%f%f%f%f%f%f%f%f%f%f%f%f%f%f%f%f%f%f%f%f%f%f%f%f%f%f%f%f%f%f%f
%f%f%f%f%f%f%f%f%f%f%f%f%f%f%f%f%f%f%f%f%f%f%f%f%f%f%f%f%f%f%f%f%f%f%f
%f%f%f%f%f%f%f%f%f%f%f%f%f%f%f%f%f%f%f%f%f%f%f%f%f%f%f%f%f%f%f%f%f%f%f
%f%f%f%f%f%f%f%f%f%f%f%f%f%f%f%f%f%f%f%f%f%f%f%f%f%f%f%f%f%f%f%f%f%f%f
%f%f%f%f%f%f%f%f%f%f%f%f%f%f%f%f%f%f%f%f%f%f%f%f%f%f%f%f%f%f%f%f%f%f%f
%f%f%f%f%f%f%f%f%f%f%f%f%f%f%f%f%f%[^\n\r]';

importDM= fopen(filename,'r'); % import difference map
DMch = textscan(importDM, formatSpec, 'Delimiter', delimiter, 'MultipleDelimsAsOne', true,
'EmptyValue' ,NaN,'HeaderLines' ,startRow-1, 'ReturnOnError', false);      %
DM = [DMch{1:end-1}];

% import the corner coordinates (CC)
startRow = 3;
endRow = 4;
formatSpec =
'%*s%f%*s%*s%*s%*s%*s%*s%*s%*s%*s%*s%*s%*s%*s%*s%*s%*s%*s%*s%*s%*s%*s%*s
%*s%*s%*s%*s%*s%*s%*s%*s%*s%*s%*s%*s%*s%*s%*s%*s%*s%*s%*s%*s%*s%*s%*s%*s
%*s%*s%*s%*s%*s%*s%*s%*s%*s%*s%*s%*s%*s%*s%*s%*s%*s%*s%*s%*s%*s%*s%*s%*s
```

```
%*s%*s%*s%*s%*s%*s%*s%*s%*s%*s%*s%*s%*s%*s%*s%*s%*s%*s%*s%*s%*s%*s%*s%*s
%*s%*s%*s%*s%*s%*s%*s%*s%*s%*s%*s%*s%*s%*s%*s%*s%*s%*s%*s%*s%*s%*s%*s%*s
%*s%*s%*s%*s%*s%*s%*s%*s%*s%*s%*s%*s%*s%*s%*s%*s%*s%*s%*s%*s%*s%*s%*s%*s
%*s%*s%*s%*s%*s%*s%*s%*s%*s%*s%*s%*s%*s%*s%*s%*s%*s%*s%*s%*s%*s%*s%*s%*s
%*s%*s%*s%*s%*s%*s%*s%*s%*s%*s%*s%*s%*s%*s%*s%*s%*s%*s%*s%*s%*s%*s%*s%*s
%*s%*s%*s%*s%*s%*s%*s%*s%*s%*s%*s%*s%*s%*s%*s%*s%*s%*s%*s%*s%*s%*s%*s%*s
%*s%*s%*s%*s%*s%*s%*s%*s%*s%*s%*s%*s%*s%*s%*s%*s%*s%*s%*s%*s%*s%*s%*s%*s
%*s%*s%*s%*s%*s%*s%*s%*s%*s%*s%*s%*s%*s%*s%*s%*s%*s%*s%*s%*s%*s%*s%*s%*s
%*s%*s%*s%*s%*s%*s%*s%*s%*s%*s%*s%*s%*s%*s%*s%*s%*s%*s%*s%*s%*s%*s%*s%*s
%*s%*s%*s%*s%*s%*s%*s%*s%*s%*s%*s%*s%*s%*s%*s%*s%*s%*s%*s%*s%*s%*s%*s%*s
%*s%*s%*s%*s%*s%*s%*s%*s%*s%*s%*s%*s%*s%*s%*s%*s%*s%*s%*s%*s%*s%*s%*s%*s
%*s%*s%*s%*s%*s%*s%*s%*s%*s%*s%*s%*s%*s%*s%*s%*s%*s%*s%*s%*s%*s%*s%*s%*s
%*s%*s%*s%*s%*s%*s%*s%*s%*s%*s%*s%*s%*s%*s%*s%*s%*s%*s%*s%*s%*s%*s%*s%*s
%*s%*s%*s%*s%*s%*s%*s%*s%*s%*s%*s%*s%*s%*s%*s%*s%*s%*s%*s%*s%*s%*s%*s%*s
%*s%*s%*s%*s%*s%*s%*s%*s%*s%*s%*s%*s%*s%*s%*s%*s%*s%*s%*s%*s%*s%*s%*s%*s
%*s%*s%*s%*s%*s%*s%*s%*s%*s%*s%*s%*s%*s%*s%*s%*s%*s%*s%*s%*s%*s%*s%*s%*s
%*s%*s%*s%*s%*s%*s%*s%*s%*s%*s%*s%*s%*s%*s%*s%*s%*s%*s%*s%*s%*s%*s%*s%*s
%*s%*s%*s%*s%*s%*s%*s%*s%*s%*s%*s%*s%*s%*s%*s%*s%*s%*s%*s%*s%*s%*s%*s%*s
%*s%*s%*s%*s%*s%*s%*s%*s%*s%*s%*s%*s%*s%*s%*s%*s%*s%*s%*s%*s%*s%*s%*s%*s
%*s%*s%*s%*s%*s%*s%*s%*s%*s%*s%*s%*s%*s%*s%*s%*s%*s%*s%*s%*s%*s%*s%*s%*s
%*s%*s%*s%*s%*s%*s%*s%*s%*s%*s%*s%*s%*s%*s%*s%*s%*s%*s%*s%*s%*s%*s%*s%*s
%*s%*s%*s%*s%*s%*s%*s%*s%*s%*s%*s%*s%*s%*s%*s%*s%*s%*s%*s%*s%*s%*s%*s%*s
%*s%*s%*s%*s%*s%*s%*s%*s%*s%*s%*s%*s%*s%*s%*s%*s%*s%*s%*s%*s%*s%*s%*s%*s
%*s%*s%*s%*s%*s%*s%*s%*s%*s%*s%*s%*s%*s%*s%*s%*s%*s%*s%*s%*s%*s%*s%*s%*s
%*s%*s%*s%*s%*s%*s%*s%*s%*s%*s%*s%*s%*s%*s%*s%*s%*s%*s%*s%*s%*s%*s%*s%*s
%*s%*s%*s%*s%*s%*s%*s%*s%*s%*s%*s%*s%*s%*s%*s%*s%*s%*s%*s%*s%*s%*s%*s%*s
%*s%*s%*s%*s%*s%*s%*s%*s%*s%*s%*s%*s%*s%*s%*s%*s%[^\n\r]';

importDM= fopen(filename,'r');
importCC= textscan(importDM, formatSpec, endRow-startRow+1, 'Delimiter', delimiter,
'MultipleDelimsAsOne', true, 'HeaderLines', startRow-1, 'ReturnOnError', false);
CCch1= cellfun(@(x) num2cell(x), importCC, 'UniformOutput', false);
CCch2= [CCch1{1:end-1}];
CC= cell2mat(CCch2);

% clear all unneeded variables
clearvars -except DM CC Vth daylabel channellabel Vthst Vthvec filename e direc

%% filter out bad points and replace all -9999 values with 0
```

```
DM= flipud(DM);


[sy, sx]=size(DM);
for i=1:sy
   for j=1:sx
        if DM(i,j)>20
          DM(i,j)=0;
        elseif DM(i,j)<-20
          DM(i,j)=0;
        end
   end
end


%% create matching vector and matrices for x and y


xDMloc = 1:2:(sx*2);       % create local x vector
yDMloc = 1:2:(sy*2);       % create local x vector


xDM = xDMloc + CC(1)-4.0980*10^6;   % transfer to New Brunswick coordinates
yDM = yDMloc + CC(2)-4.1210*10^6;   % transfer to New Brunswick coordinates




Xmat=repmat(xDM,length(yDM),1);
Ymat=repmat(yDM,length(xDM),1)';


xDMvec=reshape(Xmat,[],1);
yDMvec=reshape(Ymat,[],1);
DMvec=reshape(DM,[],1);




%% plot data
figure
contourf(xDM,yDM,DM,Vthvec)
hold on
colorbar
% xlim([600 2400])
% ylim([500 1100])
%% Generate the contours and split them in individual contours
```

```
CM=contourc(xDM,yDM,DM,Vthvec);     % extract contour matrix using the specified threshold
values
C=contourdata(CM);                  % divide the contour matrix in individual contour, and store it in a
structure

%% Find all the difference values, the x & y locations of all points within each individual contour

for i=1:length(C);                                  % loop that steps through all the contours
   if (i==1 | i==100 | i==400 | i==600 | i==800 | i==1000 | i==1200 | i==1400)
      i;
   end
   for j=1:length(Vthvec);
      %if (C(i).level==Vthvec(j) & j==1);                           % is the contour equal to the negative
threshodl value
      %    in=inpolygon(xDMvec,yDMvec,C(i).xdata,C(i).ydata);     %extract all points with this
contour
      %    eval(['Xin.D1c' num2str(i) '=xDMvec(in);']);            %find all x values of the points within
the contour
      %    eval(['Yin.D1c' num2str(i) '=yDMvec(in);']);            %find all y values of the points within
the contour
      %    eval(['DMin.D1c' num2str(i) '=DMvec(in);']);            %find all difference map values within
the contour
      %    eval(['Xin.Dc' num2str(i) '=Xin.D1c' num2str(i) '(DMin.D1c' num2str(i) '<Vthvec(1));']);
%find all x values of the points within the contour where the difference (DM) is indeed larger than Vth
(this prevent islands with in contour)
      %    eval(['Yin.Dc' num2str(i) '=Yin.D1c' num2str(i) '(DMin.D1c' num2str(i) '<Vthvec(1));']);
%find all y values of the points within the contour where the difference (DM) is indeed larger than Vth
(this prevent islands with in contour)
      %    eval(['DMin.Dc' num2str(i) '=DMin.D1c' num2str(i) '(DMin.D1c' num2str(i) '<Vthvec(1));']);
%find all DM values of the points within the contour where the difference (DM) is indeed larger than
Vth (this prevent islands with in contour)
      %    eval(['DMDS(' num2str(i) ')=sum(DMin.Dc' num2str(i) ')*4;']);            %sum all  DM values
within the contour and multiply by area (2x2m)
      %    eval(['XDm(' num2str(i) ')=mean(Xin.Dc' num2str(i) ');']);            % extract mean x value for
this contour
      %    eval(['YDm(' num2str(i) ')=mean(Yin.Dc' num2str(i) ');']);            % extract mean y value for
this contour
      %    eval(['Ym(' num2str(i) ')=nanmean(Yin.Dc' num2str(i) ');']);            % extract mean y value
for this contour and place in a erosion and deposition matrix
```

```
    %    eval(['Xm(' num2str(i) ')=nanmean(Xin.Dc' num2str(i) ');']);            % extract mean x value for this contour and place in a erosion and deposition matrix
    %    eval(['DMS(' num2str(i) ')=sum(DMin.Dc' num2str(i) ');']);            % extract mean DM value for this contour and place in a erosion and deposition matrix
    if (C(i).level==Vthvec(j) & j<length(Vthvec) & Vthvec(j)<0);                              % is the contour equal to the negative threshodl value
        in=inpolygon(xDMvec,yDMvec,C(i).xdata,C(i).ydata);     %extract all points with this contour
        eval(['Xin.D1c' num2str(i) '=xDMvec(in);']);            %find all x values of the points within the contour
        eval(['Yin.D1c' num2str(i) '=yDMvec(in);']);            %find all y values of the points within the contour
        eval(['DMin.D1c' num2str(i) '=DMvec(in);']);            %find all difference map values within the contour
        eval(['Xin.Dc' num2str(i) '=Xin.D1c' num2str(i) '(DMin.D1c' num2str(i) '<Vthvec(' num2str(j) ') & DMin.D1c' num2str(i) '>Vthvec(' num2str(j-1) '));']);            %find all x values of the points within the contour where the difference (DM) is indeed larger than Vth (this prevent islands with in contour)
        eval(['Yin.Dc' num2str(i) '=Yin.D1c' num2str(i) '(DMin.D1c' num2str(i) '<Vthvec(' num2str(j) ') & DMin.D1c' num2str(i) '>Vthvec(' num2str(j-1) '));']);            %find all y values of the points within the contour where the difference (DM) is indeed larger than Vth (this prevent islands with in contour)
        eval(['DMin.Dc' num2str(i) '=DMin.D1c' num2str(i) '(DMin.D1c' num2str(i) '<Vthvec(' num2str(j) ') & DMin.D1c' num2str(i) '>Vthvec(' num2str(j-1) '));']);          %find all DM values of the points within the contour where the difference (DM) is indeed larger than Vth (this prevent islands with in contour)
        eval(['DMDS(' num2str(i) ')=sum(DMin.Dc' num2str(i) ')*4;']);            %sum all  DM values within the contour and multiply by area (2x2m)
        eval(['XDm(' num2str(i) ')=mean(Xin.Dc' num2str(i) ');']);            % extract mean x value for this contour
        eval(['YDm(' num2str(i) ')=mean(Yin.Dc' num2str(i) ');']);            % extract mean y value for this contour
        eval(['Ym(' num2str(i) ')=nanmean(Yin.Dc' num2str(i) ');']);            % extract mean y value for this contour and place in a erosion and deposition matrix
        eval(['Xm(' num2str(i) ')=nanmean(Xin.Dc' num2str(i) ');']);            % extract mean x value for this contour and place in a erosion and deposition matrix
        eval(['DMS(' num2str(i) ')=sum(DMin.Dc' num2str(i) ');']);            % extract mean DM value for this contour and place in a erosion and deposition matrix
    elseif (C(i).level==Vthvec(j) & j<length(Vthvec) & Vthvec(j)>0);                              % is the contour equal to the negative threshodl value
        in=inpolygon(xDMvec,yDMvec,C(i).xdata,C(i).ydata);     %extract all points with this contour
        eval(['Xin.D1c' num2str(i) '=xDMvec(in);']);            %find all x values of the points within the contour
```

```
        eval(['Yin.D1c' num2str(i) '=yDMvec(in);']);            %find all y values of the points within the contour
        eval(['DMin.D1c' num2str(i) '=DMvec(in);']);            %find all difference map values within the contour
        eval(['Xin.Dc' num2str(i) '=Xin.D1c' num2str(i) '(DMin.D1c' num2str(i) '>Vthvec(' num2str(j) ') & DMin.D1c' num2str(i) '<Vthvec(' num2str(j+1) '));']);            %find all x values of the points within the contour where the difference (DM) is indeed larger than Vth (this prevent islands with in contour)
        eval(['Yin.Dc' num2str(i) '=Yin.D1c' num2str(i) '(DMin.D1c' num2str(i) '>Vthvec(' num2str(j) ') & DMin.D1c' num2str(i) '<Vthvec(' num2str(j+1) '));']);            %find all y values of the points within the contour where the difference (DM) is indeed larger than Vth (this prevent islands with in contour)
        eval(['DMin.Dc' num2str(i) '=DMin.D1c' num2str(i) '(DMin.D1c' num2str(i) '>Vthvec(' num2str(j) ') & DMin.D1c' num2str(i) '<Vthvec(' num2str(j+1) '));']);           %find all DM values of the points within the contour where the difference (DM) is indeed larger than Vth (this prevent islands with in contour)
        eval(['DMDS(' num2str(i) ')=sum(DMin.Dc' num2str(i) ')*4;']);            %sum all  DM values within the contour and multiply by area (2x2m)
        eval(['XDm(' num2str(i) ')=mean(Xin.Dc' num2str(i) ');']);           % extract mean x value for this contour
        eval(['YDm(' num2str(i) ')=mean(Yin.Dc' num2str(i) ');']);           % extract mean y value for this contour
        eval(['Ym(' num2str(i) ')=nanmean(Yin.Dc' num2str(i) ');']);           % extract mean y value for this contour and place in a erosion and deposition matrix
        eval(['Xm(' num2str(i) ')=nanmean(Xin.Dc' num2str(i) ');']);           % extract mean x value for this contour and place in a erosion and deposition matrix
        eval(['DMS(' num2str(i) ')=sum(DMin.Dc' num2str(i) ');']);            % extract mean DM value for this contour and place in a erosion and deposition matrix
    %elseif (C(i).level==Vthvec(j) & j==length(Vthvec));                              % is the contour equal to the negative threshodl value
    %    in=inpolygon(xDMvec,yDMvec,C(i).xdata,C(i).ydata);      %extract all points with this contour
    %    eval(['Xin.D1c' num2str(i) '=xDMvec(in);']);            %find all x values of the points within the contour
    %    eval(['Yin.D1c' num2str(i) '=yDMvec(in);']);            %find all y values of the points within the contour
    %    eval(['DMin.D1c' num2str(i) '=DMvec(in);']);            %find all difference map values within the contour
    %    eval(['Xin.Dc' num2str(i) '=Xin.D1c' num2str(i) '(DMin.D1c' num2str(i) '>Vthvec(' num2str(j) '));']);            %find all x values of the points within the contour where the difference (DM) is indeed larger than Vth (this prevent islands with in contour)
```

```
    %   eval(['Yin.Dc' num2str(i) '=Yin.D1c' num2str(i) '(DMin.D1c' num2str(i) '>Vthvec('
num2str(j) '));']);            %find all y values of the points within the contour where the difference (DM)
is indeed larger than Vth (this prevent islands with in contour)
    %   eval(['DMin.Dc' num2str(i) '=DMin.D1c' num2str(i) '(DMin.D1c' num2str(i) '>Vthvec('
num2str(j) '));']);          %find all DM values of the points within the contour where the difference
(DM) is indeed larger than Vth (this prevent islands with in contour)
    %   eval(['DMDS(' num2str(i) ')=sum(DMin.Dc' num2str(i) ')*4;']);           %sum all  DM values
within the contour and multiply by area (2x2m)
    %   eval(['XDm(' num2str(i) ')=mean(Xin.Dc' num2str(i) ');']);           % extract mean x value for
this contour
    %   eval(['YDm(' num2str(i) ')=mean(Yin.Dc' num2str(i) ');']);           % extract mean y value for
this contour
    %   eval(['Ym(' num2str(i) ')=nanmean(Yin.Dc' num2str(i) ');']);           % extract mean y value
for this contour and place in a erosion and deposition matrix
    %   eval(['Xm(' num2str(i) ')=nanmean(Xin.Dc' num2str(i) ');']);           % extract mean x value
for this contour and place in a erosion and deposition matrix
    %   eval(['DMS(' num2str(i) ')=sum(DMin.Dc' num2str(i) ');']);           % extract mean DM value
for this contour and place in a erosion and deposition matrix
    end
  end
end

%% plot points and contour to check whether the points match the contours


% figure
% subplot(211)
% for i=1:length(C)
%     for j=1:length(Vthvec);
%         if (C(i).level==Vthvec(j))
%             %plot(C(i).xdata,C(i).ydata,'k');
%             %hold on
%             eval(['scatter(Xin.Dc' num2str(i) ',Yin.Dc' num2str(i) ',25,[1 ' num2str(j/length(Vthvec)) '
0]);']);
%             hold on
%         end
%     end
% end
%legend('erosion in red','deposition in blue >Vth','deposition >Vth/20 in black')


% subplot(212)
```

```
% for i=1:length(C)
%     for j=1:length(Vthvec);
%         if (C(i).level==Vthvec(j))
%             plot(C(i).xdata,C(i).ydata,'Color',[1 j/length(Vthvec) 0]);
%             hold on
%             eval(['scatter(Xin.Dc' num2str(i) ',Yin.Dc' num2str(i) ',25,[1 ' num2str(j/length(Vthvec)) ' 
0]);']);
%             hold on
%         end
%     end
% end

%% plot the mean values fo x & y to check they are in the correct location

% figure
% for i=1:length(C)
%     for j=1:length(Vthvec);
%         if (C(i).level==Vthvec(j))
%             plot(C(i).xdata,C(i).ydata,'Color',[1 j/length(Vthvec) 0]);
%             hold on
%             eval(['scatter(Xm(' num2str(i) '),Ym(' num2str(i) '),25,[1 ' num2str(j/length(Vthvec)) ' 0]);']);
%             hold on
%         end
%     end
% end



%% Check erosion versus deposition as a function of location (stars scale with volume, red=erosion & 
blue=deposition)

% figure
% for i=1:length(C)
%     for j=1:length(Vthvec);
%         if (C(i).level==Vthvec(j))
%             plot(C(i).xdata,C(i).ydata,'Color',[1 j/length(Vthvec) 0]);
%             hold on
%             eval(['scatter(Xm(' num2str(i) '),Ym(' num2str(i) '),(-DMS(' num2str(i) 
')+max(DMS))*10,"*","MarkerEdgeColor",[1 ' num2str(j/length(Vthvec)) ' 0]);']);
%             hold on
```

```
%         end
%     end
% end

%% load spline and plot spine together with data to check location

ChanLoc = filename(11);

if ChanLoc == 'n'
    load('NorSpline.mat')
    xy = struct('Position', {NorSpline(1:end).Position});
    loc=[NorSpline.Position];
elseif ChanLoc == 'c'
    load('CenSpline.mat')
    xy = struct('Position', {CenSpline(1:end).Position});
    loc=[CenSpline.Position];
elseif ChanLoc == 's'
    load('SouSpline.mat')
    xy = struct('Position', {SouSpline(1:end).Position});
    loc=[SouSpline.Position];
end




        n = 3;
    %xloc = loc(1 : n : end) + 760;
    %yloc = loc(2 : n : end) + 540;
    xloc = loc(1 : n : end)+ 1000;
    yloc = loc(2 : n : end)+ 1000;

    xNChan = min(xloc):max(xloc);
    xNChan = round(xNChan);
    yNChan = spline(xloc,yloc,xNChan);

    yNChan1 = fliplr(yNChan);
    xNChan1 = fliplr(xNChan);
```

```
%check location of the spline
contour(xDM,yDM,DM)
hold on
plot(xloc,yloc,'*k');
plot(xNChan1,yNChan1);

%% calculate distance from a fixed spline start point on the delta top to the centre of the contour

% calculate cummulative distance along the spline
for i = 1:length(xNChan1)
    if i == 1;
        gv(i) = 0;
    else
        gv(i) = sqrt(( xNChan1(i) - xNChan1(i-1) )^2 + (yNChan1(i) - yNChan1(i-1))^2) + gv(i-1);
    end
end

%if ChanLoc == 's'
%   gv=fliplr(gv);
%end

% find the nearest point on the spline for every contour
for j = 1:length(DMS)
   for i = 1:length(xNChan1);
        b(1,j) = Xm(j);
        b(2,j) = Ym(j);
        Distance(i) = sqrt(  (b(2,j)-yNChan1(i))^2   +    (b(1,j)-xNChan1(i))^2   );
   end
    [mini idx] = min(Distance);
    DistSpline(j) = gv(idx);
    Xspline(j) = xNChan1(idx);
    Yspline(j) = yNChan1(idx);
end

% check that the distance along the spline correlates roughly with the mean
% x position
% figure
% plot(DistSpline,Xm,'*')
```

```
%% Sort the contour and their volumes by distance along the spline

[DMdist DMorder] = sort(DistSpline);

DMScum = zeros(1,length(DistSpline));

for i = 1:length(DistSpline);
    DMSsort(i) = DMS(DMorder(i));
    Xmsort(i) = Xm(DMorder(i));
    Ymsort(i) = Ym(DMorder(i));
    if i > 1
        DMScum(i) = DMScum(i-1)+ DMSsort(i);
    end
end

%%
%
% figure
% subplot(311)
% plot(DMdist,DMScum,'-*')
% hold on
% set(gca,'XDir','reverse')
% grid on
%
% subplot(312)
% plot(DMdist,DMSsort,'-*')
% hold on
% set(gca,'XDir','reverse')

% subplot(313)
% for i=1:length(C)
%     for j=1:length(Vthvec);
%         if (C(i).level==Vthvec(j))
%             plot(C(i).xdata,C(i).ydata,'Color',[1 j/length(Vthvec) 0]);
%             hold on
%             eval(['scatter(Xm(' num2str(i) '),Ym(' num2str(i) '),(-DMS(' num2str(i) ')+max(DMS)),''*'',''MarkerEdgeColor'',[1 ' num2str(j/length(Vthvec)) ' 0]);']);
%             hold on
```

```
%        end
%     end
% end




eval([' '  filename(1:11)  '.Vol = DMSsort ']);


eval(['Vol ='  filename(1:11)  '.Vol;']);


U = find(Vol == 0);
Vol(U) = [];
FVal = Vol(find(Vol<0,15));




%eval(['FVal = find(' filename(1:11) '.Vol<0,15);']);
eval([' '  filename(1:11)  '.cumVol = (DMScum).*-1;']);
eval([' '  filename(1:11)  '.Dist = DMdist;']);
eval([' '  filename(1:11)  '.Xm = Xmsort;']);
eval([' '  filename(1:11)  '.Ym = Ymsort;']);
eval([' '  filename(1:11)  '.Xspline = Xspline;']);
eval([' '  filename(1:11)  '.Yspline = Yspline;']);
eval([' '  filename(1:11)  '.DM = DM;']);
%eval([' '  filename(1:11)  '.FVol = (min(' filename(1:11) '.Vol(FVal)).*-1);']);
eval([' '  filename(1:11)  '.FVol = (min(FVal));'])
eval([' '  filename(1:11)  '.DistDiff = max(' filename(1:11) '.Dist)-min(' filename(1:11) '.Dist);']);
eval([' '  filename(1:11)  '.MaxMinVol = max(DMScum)-min(DMScum);'])
eval([' '  filename(1:11)  '.MaxVol = min(DMScum);'])
eval([' '  filename(1:11)  '.Erosion = (sum(' filename(1:11) '.Vol(' filename(1:11) '.Vol<0))-('
filename(1:11) '.FVol));'])
eval([' '  filename(1:11)  '.Deposition = (sum(' filename(1:11) '.Vol(' filename(1:11) '.Vol>0))-('
filename(1:11) '.FVol));'])
eval([' '  filename(1:11)  '.SedChange =' filename(1:11) '.Deposition+' filename(1:11) '.Erosion+'
filename(1:11) '.FVol;'])


% save('Allevents.mat',filename(1:11),'-append')
```

```
clearvars -except e direc

end
```

APPENDIX 2: CLAY CLAST DATA AND PROCESSING SCRIPT.

```
%First two letters correspond to experiment type
%(i.e. cl = clear water, ls = low sand percent, hs = high sand percent)
%(i.e. lb = low ballotini percent, hb = high ballotini percent)
%'Lo' and 'hi' corresponds to the flow velocity (low or high, respectively)
%The letter on the end denotes whether the variable is the size (s) of
%the clast (in cm), or the weight (w) of the clast (in grams).
%So cl_lo_s means clear water, low velocity, clast size.
%NaN denotes when a clast was lost.
close all
clear all

%Clear water
cl_lo_s = [2 2 2 2 2 2 2 2 2 2; 1.9 1.9 1.9 1.9 1.9 1.9 1.9 1.9 1.9 1.8; 1.7 1.6 1.7 1.6 1.6 1.6 1.7 1.6 1.7 1.7; 1.5 1.4 1.4 1.5 1.5 1.5 1.4 1.5 1.4 1.5; 1.3 1.3 1.3 1.3 1.2 1.3 1.3 1.3 1.2 1.3; 1.1 1.1 1 1.1 1 1.1 1.1 1.1 1 1.1; 0.9 1 1 0.9 0.9 0.9 0.9 0.9 0.9 0.9];
```

```
cl_hi_s = [2 2 2 2 2 2 2 2 2 2; 1.8 1.7 1.7 1.7 1.7 1.7 1.7 1.7 1.7 1.7; 1.4 1.3 1.3 1.3 1.3 1.3 1.3 1.3 1.3
1.3; 1 1 1 1 1 1 1 0.9 1 1; 0.7 0.7 0.7 0.7 0.7 0.7 0.8 0.7 0.7 0.7; 0.4 0.5 0.5 0.5 0.5 0.4 0.5 0.6 0.5 NaN;
0 0 0 0 0 0 0 0 0 0];

cl_lo_w = [13.2 12.9 13.1 13.4 13.8 12.9 13.3 13.9 12.5 13; 8.2 8.7 8.8 8.9 8.2 9 7.8 8.3 8.4 8.1; 5.5 6.2
5.7 5.1 5.5 5.5 6.1 6 5.5 6.1; 4.1 3.6 3.8 4.3 4 3.6 3.7 3.2 4.1 3.7; 2.4 2.8 2.4 2.5 2.4 2 2.5 2.7 2.8 2.7;
1.5 1.6 1.5 1.4 1.8 1.2 1.8 1.5 1.7 1.6; 0.9 0.7 1.1 0.9 1 1.2 0.9 1.2 0.9 1];
cl_hi_w = [13.8 13.1 12.9 13.6 13.9 13.1 13.7 13.4 12.9 13.5; 6.1 6.4 6.8 6.6 6.7 6.2 6.4 6.5 6.1 6.8; 2.6
2.9 3.1 3.1 3.1 2.9 2.8 2.8 2.9 3.1; 1.2 1.2 1.1 1 1.2 1.1 1.2 1.3 1.2 1.1; 0.4 0.4 0.5 0.3 0.4 0.4 0.3 0.5
0.4 0.3; 0.1 0.1 0.1 0.1 0.1 0.2 0.2 0.1 0.1 NaN; 0 0 0 0 0 0 0 0 0 0];

%Low sand
ls_lo_s = [2 2 2 2 2 2 2 2 2 2; 2.1 2 2.1 2.3 2.2 2.2 2.1 2.1 2.1 2.2; 2 2 2.1 2.1 2 2 2 2 2.1 2.1; 2 1.9 2
1.9 2 2 2 1.9 2 2; 1.9 1.8 1.9 1.8 1.9 1.9 1.8 1.8 1.9 1.9; 1.7 1.8 1.8 1.7 1.8 1.8 1.7 1.7 1.7 1.7; 1.7 1.7
1.6 1.6 1.6 1.7 1.6 1.7 1.7 1.6];
ls_hi_s = [2 2 2 2 2 2 2 2 2 2; 2 1.9 2 2 2 2 2 2 2 1.9; 1.7 1.7 1.7 1.7 1.8 1.7 1.7 1.7 1.7 1.7; 1.6 1.6 1.5
1.5 1.5 1.5 1.6 1.5 1.6 1.6; 1.4 1.4 1.4 1.4 1.4 1.4 1.3 1.4 1.4 1.3; 1.2 1.2 1.1 1.2 1.2 1.2 1.2 1.2 1.2 1.2;
1 1 1 1.1 1 1 1 1 1 1];

ls_lo_w = [13.3 13.7 13.5 13.8 12.5 12.7 13.1 12.7 12.9 13.4; 12.3 12.1 12.6 13 13.5 11.9 12.2 12.7
12.5 13.4; 11.1 10.7 10.6 10.4 10.7 10.3 11.5 11.6 10.8 10.2; 8.9 8.6 9 9.1 9.9 9.8 8.6 9.3 9.1 9.6; 7.8
7.6 7.4 8.6 7.8 8.5 7.6 8.2 8 7.3; 6.2 7.4 6.6 6.7 6.6 7 6.5 6.2 7.2 6.4; 5.7 5.4 6.1 6.2 5.6 5.2 5.5 5.2 5.9
5.5];
ls_hi_w = [13.6 13.4 13.5 13.7 13.7 13.9 13.9 13.4 13.4 13.7; 10.4 10.6 10.5 10.5 10.8 10.8 10.5 10.4
10.4 10.6; 7.6 7.4 7.5 7.3 7.7 7.6 7.3 7.7 7.4 7.5; 5.2 5.4 5.3 5.4 5.2 5 5.1 5 5.2 5.1; 3.3 3.5 3.7 3.4 3.4
3.5 3.6 3.7 3.5 3.5; 2.2 2.3 2.1 2.3 2.2 2.4 2.2 2.3 2.1 2.3; 1.4 1.4 1.4 1.5 1.3 1.2 1.3 1.3 1.2 1.4];

%High Sand
hs_lo_s = [2 2 2 2 2 2 2 2 2 2; 2.1 2.2 2.1 2.2 2.2 2.1 2.1 2.1 2.2 2.2; 2.1 2 2.2 2.1 2.1 2.2 2.2 2.1 2.1
2.1; 2 2 2 2 2.1 2.1 2.2 2.1 2.1 2.1; 2.1 2 2 2.1 1.9 2 2 2 2 2.1; 1.9 2 1.9 2 1.9 1.9 2 2 1.9 1.9; 1.8 1.9 1.9
1.9 1.9 1.9 1.9 1.9 1.9 1.9];
hs_hi_s = [2 2 2 2 2 2 2 2 2 2; 2.1 2 2 2.1 2 2 2 2.1 2 2; 2.1 2.1 2 2 2 2.1 2.1 2.1 2.1 2; 2 2 1.9 1.9 1.9
1.9 1.9 1.9 1.9 2; 1.8 1.8 1.8 1.8 1.8 1.8 1.8 1.8 1.8 1.8; 1.7 1.7 1.7 1.7 1.7 1.7 1.7 1.7 1.7 1.7; 1.7 1.6
1.7 1.6 1.6 1.7 1.6 1.6 1.6 1.6];

hs_lo_w = [15.2 15.5 15.9 14.4 16.6 14.4 16.9 15.3 17.1 16.2; 14.2 16.9 14.8 15.9 16.3 13.9 16 14.9
14.9 15.3; 14.7 14.2 13.3 14.1 13.2 12.6 12.4 15.1 13.6 13.3; 12.8 13.3 10.9 12.3 10.8 12.4 11.9 11.6
12.1 11.5; 10.5 10.9 11.3 10.6 10.2 10.2 9.8 10.9 11.7 9.4; 8.9 9 9.4 9.3 8.6 9.8 10 8.3 10.5 9.3; 8.8 8.3
8.2 7.6 9.2 7.3 7.9 8.1 8.6 8];
```

```
hs_hi_w = [13.4 13.9 13.9 13.1 13.7 13.5 13.5 13.3 13.7 13; 12.6 12.4 12.7 12.1 12.5 13.1 12.4 13.1
12.6 12.2; 11.2 10.6 10.5 10.4 10.8 10.5 10.8 11.2 10.5 10.6; 8.8 9.5 8.9 8.8 8.8 9.1 8.8 9 9.4 8.8; 7.3
7.4 7.5 7.6 7.7 8 7.4 7.3 7.5 8; 6.4 6.3 6.4 6.4 6.3 6.1 6.1 6.1 6.8 6.6; 5 5.4 5.3 5.1 5.7 5.3 5.3 5.3 5 5.5];

%Low Ballotini
lb_lo_s = [2 2 2 2 2 2 2 2 2 2; 2.2 2.2 2.2 2.2 2.1 2.1 2.2 2.1 2.2 2.2; 2 2 2 2 2 2.1 2.1 2 2 2; 1.9 1.9 1.9
2 1.9 1.9 1.9 1.9 1.9 1.9; 1.8 1.7 1.8 1.8 1.8 1.9 1.8 1.9 1.8 1.8; 1.7 1.7 1.7 1.7 1.6 1.6 1.6 1.7 1.7 1.7;
1.6 1.5 1.5 1.6 1.5 1.6 1.6 1.6 1.5 1.6];
lb_hi_s = [2 2 2 2 2 2 2 2 2 2; 2 2 2 2 2.1 2 2 2 2 2; 1.8 1.8 1.8 1.8 1.8 1.8 1.8 1.8 1.8 1.7; 1.6 1.6 1.6
1.6 1.5 1.5 1.5 1.5 1.5 1.5; 1.4 1.4 1.4 1.4 1.4 1.4 1.4 1.4 1.4 1.5; 1.2 1.2 1.2 1.2 1.2 1.2 1.2 1.2 1.2 1.2;
1.1 1.1 1.1 1.1 1.1 1 1 1 1 1];

lb_lo_w = [14.3 13.6 13.6 14.7 14.8 15.4 14.5 15.9 14.3 14.2; 13.4 14.1 13.1 12.4 13 13.5 13.3 12.4
14.5 13; 10.6 10.8 10.2 11.7 12 10.6 10.2 10.7 11.2 11; 8.9 8.6 9.5 8.7 9.2 8.3 10 8.3 8.7 9.1; 6.7 7 8.2
7.1 7.5 7.2 6.7 7.4 7.8 7.1; 6 5.9 6.7 5.4 5.6 5.4 5.7 5.9 5.8 6.3; 5.1 4.5 4.7 4.5 4.7 5.4 4.3 4.7 4.9 4.4];
lb_hi_w = [13.9 13.1 13.7 13.8 13.2 13.3 13.4 13.2 13.4 13.8; 10.5 10.6 10 9.9 10.4 10.2 10.1 10.4 9.7
10.1; 7.3 7.5 7.5 7.1 7.6 6.9 7.1 7.2 6.9 7; 4.7 4.9 5.4 5.2 5 5.3 4.9 5.1 5 4.8; 3.7 3.6 3.3 3.2 3.6 3.5 3.3
3.4 3.3 3.1; 2.1 2 1.9 2.1 2.3 2.3 2.2 2.1 2.3 2; 1.3 1.1 1.3 1.3 1.2 1.4 1.2 1.4 1.4 1.3];



cl_lo_w = sort(cl_lo_w,2);
cl_hi_w = sort(cl_hi_w,2);
ls_lo_w = sort(ls_lo_w,2);
ls_hi_w = sort(ls_hi_w,2);
hs_lo_w = sort(hs_lo_w,2);
hs_hi_w = sort(hs_hi_w,2);
lb_lo_w = sort(lb_lo_w,2);
lb_hi_w = sort(lb_hi_w,2);

figure(1)
hold on
plot(cl_lo_w)
plot(cl_hi_w)
plot(ls_lo_w)
plot(ls_hi_w)
plot(hs_lo_w)
plot(hs_hi_w)
plot(lb_lo_w)
plot(lb_hi_w)
```

```
% plot(ls_1_s1)
% eval(['plot(cl_10_s' num2str(i) ')'])

%% Percent of cube in tact
[sy sx] = size(cl_lo_w);

for i = 1:sy
    for j = 1:sx

    cl_lo_wp(i,j) = cl_lo_w(i,j)./cl_lo_w(1,j);
    cl_hi_wp(i,j) = cl_hi_w(i,j)./cl_hi_w(1,j);
    ls_lo_wp(i,j) = ls_lo_w(i,j)./ls_lo_w(1,j);
    ls_hi_wp(i,j) = ls_hi_w(i,j)./ls_hi_w(1,j);
    hs_lo_wp(i,j) = hs_lo_w(i,j)./hs_lo_w(1,j);
    hs_hi_wp(i,j) = hs_hi_w(i,j)./hs_hi_w(1,j);
    lb_lo_wp(i,j) = lb_lo_w(i,j)./lb_lo_w(1,j);
    lb_hi_wp(i,j) = lb_hi_w(i,j)./lb_hi_w(1,j);
    end
end

%% Averages each row (in the second dimension)
Avg_cl_lo = nanmean(cl_lo_w,2); %Averages each row (in the second dimension)
Avg_cl_hi = nanmean(cl_hi_w,2);
Avg_ls_lo = nanmean(ls_lo_w,2);
Avg_ls_hi = nanmean(ls_hi_w,2);
Avg_hs_lo = nanmean(hs_lo_w,2);
Avg_hs_hi = nanmean(hs_hi_w,2);
Avg_lb_lo = nanmean(lb_lo_w,2);
Avg_lb_hi = nanmean(lb_hi_w,2);

Avg_cl_lop = nanmean(cl_lo_wp,2); %Percentages
Avg_cl_hip = nanmean(cl_hi_wp,2);
Avg_ls_lop = nanmean(ls_lo_wp,2);
Avg_ls_hip = nanmean(ls_hi_wp,2);
Avg_hs_lop = nanmean(hs_lo_wp,2);
Avg_hs_hip = nanmean(hs_hi_wp,2);
Avg_lb_lop = nanmean(lb_lo_wp,2);
Avg_lb_hip = nanmean(lb_hi_wp,2);
```

```
% Avg_ls_1 = nanmean(ls_1_w,2);

%% Percent of cube lost
%Clear water
Avg_cl_lopl = (Avg_cl_lop-1).*-1;
Avg_cl_hipl = (Avg_cl_hip-1).*-1;
Avg_ls_lopl = (Avg_ls_lop-1).*-1;
Avg_ls_hipl = (Avg_ls_hip-1).*-1;
Avg_hs_lopl = (Avg_hs_lop-1).*-1;
Avg_hs_lopl = (Avg_hs_lop-1).*-1;
Avg_lb_lopl = (Avg_lb_lop-1).*-1;
Avg_lb_lopl = (Avg_lb_lop-1).*-1;

%Rough bed
%Low percent sand
% Avg_ls_1pl = (Avg_ls_1p-1).*-1;
%High percent sand
%% Maximum and minimum range for each experiment
for i = 1:7
   %Maxima
   maxcllo(:,i) = (max(cl_lo_w,[],2)-Avg_cl_lo);%Data - Clear water, low speed
   maxclhi(:,i) = (max(cl_hi_w,[],2)-Avg_cl_hi);%Clear Water, high speed
   maxlslo(:,i) = (max(ls_lo_w,[],2)-Avg_ls_lo);%Low sand, low speed
   maxlshi(:,i) = (max(ls_hi_w,[],2)-Avg_ls_hi);%Low sand, high speed
   maxhslo(:,i) = (max(hs_lo_w,[],2)-Avg_hs_lo);%High sand, low speed
   maxhshi(:,i) = (max(hs_hi_w,[],2)-Avg_hs_hi);%High sand, high speed
   maxlblo(:,i) = (max(lb_lo_w,[],2)-Avg_lb_lo);%Low Ballotini, low speed
   maxlbhi(:,i) = (max(lb_hi_w,[],2)-Avg_lb_hi);%Low Ballotini, high speed

   maxcllop(:,i) = (max(cl_lo_wp,[],2)-Avg_cl_lop);%Percents
   maxclhip(:,i) = (max(cl_hi_wp,[],2)-Avg_cl_hip);%Same as above
   maxlslop(:,i) = (max(ls_lo_wp,[],2)-Avg_ls_lop);
   maxlship(:,i) = (max(ls_hi_wp,[],2)-Avg_ls_hip);
   maxhslop(:,i) = (max(hs_lo_wp,[],2)-Avg_hs_lop);
   maxhship(:,i) = (max(hs_hi_wp,[],2)-Avg_hs_hip);
   maxlblop(:,i) = (max(lb_lo_wp,[],2)-Avg_lb_lop);
   maxlbhip(:,i) = (max(lb_hi_wp,[],2)-Avg_lb_hip);

   %Minima
   %Clear water
```

```
    mincllo(:,i) = (Avg_cl_lo-min(cl_lo_w,[],2));%Data
    minclhi(:,i) = (Avg_cl_hi-min(cl_hi_w,[],2));
    minlslo(:,i) = (Avg_ls_lo-min(ls_lo_w,[],2));
    minlshi(:,i) = (Avg_ls_hi-min(ls_hi_w,[],2));
    minhslo(:,i) = (Avg_hs_lo-min(hs_lo_w,[],2));
    minhshi(:,i) = (Avg_hs_hi-min(hs_hi_w,[],2));
    minlblo(:,i) = (Avg_lb_lo-min(lb_lo_w,[],2));
    minlbhi(:,i) = (Avg_lb_hi-min(lb_hi_w,[],2));

    mincllop(:,i) = (Avg_cl_lop-min(cl_lo_wp,[],2));%Percents
    minclhip(:,i) = (Avg_cl_hip-min(cl_hi_wp,[],2));
    minlslop(:,i) = (Avg_ls_lop-min(ls_lo_wp,[],2));
    minlship(:,i) = (Avg_ls_hip-min(ls_hi_wp,[],2));
    minhslop(:,i) = (Avg_hs_lop-min(hs_lo_wp,[],2));
    minhship(:,i) = (Avg_hs_hip-min(hs_hi_wp,[],2));
    minlblop(:,i) = (Avg_lb_lop-min(lb_lo_wp,[],2));
    minlbhip(:,i) = (Avg_lb_hip-min(lb_hi_wp,[],2));
    %Rough bed
    %Low percent sand
%     minls1(:,i) = (Avg_ls_1-min(ls_1_w,[],2));
    %High percent sand
end

%% Plotting
% Average data with range as error bars
figure(2)
% plot(Avg_cl_1,'o')
hold on
errorbar(time1,Avg_cl_lo,mincllo(:,1),maxcllo(:,1),'LineWidth',2);
errorbar(time2,Avg_cl_hi,minclhi(:,1),maxclhi(:,1));
errorbar(time1,Avg_ls_lo,minlslo(:,1),maxlslo(:,1),'LineWidth',2);
errorbar(time2,Avg_ls_hi,minlshi(:,1),maxlshi(:,1));
errorbar(time1,Avg_hs_lo,minhslo(:,1),maxhslo(:,1),'LineWidth',2);
errorbar(time2,Avg_hs_hi,minhshi(:,1),maxhshi(:,1));
errorbar(time1,Avg_lb_lo,minlblo(:,1),maxlblo(:,1),'LineWidth',2);
errorbar(time2,Avg_lb_hi,minlbhi(:,1),maxlbhi(:,1));
% xlim([0 60])
xlabel('Distance travelled [ m ]')
ylabel('Weight [ grams ]')
```

```
legend('Clear water (Slow)','Clear water (Fast)','1% Sand (Slow)','1% sand (Fast)','10% sand (Slow)','10% sand (Fast)','1% Ballotini (Slow)','1% Ballotini (Fast)')

% %Error bar test
% figure(3)
% errorbar(time,Avg_cl_10,mincl10(:,1),maxcl10(:,1));
% hold on
% plot(time,Avg_cl_10,'-r')
% plot(time,cl_10_w,'*r')

% %Boxplots
% figure(4)
% boxplot(transpose(cl_1_w),'Colors','r')
% hold on
% boxplot(transpose(cl_5_w),'Colors','k')
% boxplot(transpose(cl_10_w),'Colors','b')

%Percent in tact
figure(5)
errorbar((time1),Avg_cl_lop,mincllop(:,1),maxcllop(:,1),'b','LineWidth',2)
hold on
errorbar((time2),Avg_cl_hip,minclhip(:,1),maxclhip(:,1),'b')
errorbar((time1),Avg_ls_lop,minlslop(:,1),maxlslop(:,1),'k','LineWidth',2)
errorbar((time2),Avg_ls_hip,minlship(:,1),maxlship(:,1),'k')
errorbar((time1),Avg_hs_lop,minhslop(:,1),maxhslop(:,1),'r','LineWidth',2)
errorbar((time2),Avg_hs_hip,minhship(:,1),maxhship(:,1),'r')
errorbar((time1),Avg_lb_lop,minlblop(:,1),maxlblop(:,1),'g','LineWidth',2)
errorbar((time2),Avg_lb_hip,minlbhip(:,1),maxlbhip(:,1),'g')
% errorbar(time,Avg_ls_1p,minls1p(:,1),maxls1p(:,1),'LineWidth',2)
ylabel('Percent intact [ % ]')
xlabel('Distance travelled [ m ]')
% xlim([0 70])
legend('Clear water (Slow)','Clear water (Fast)','1% Sand (Slow)','1% sand (Fast)','10% sand (Slow)','10% sand (Fast)','1% Ballotini (Slow)','1% Ballotini (Fast)')

%% Rates

for i = 1:length(Avg_cl_lop)-1;
```

```
    Avg_cl_lop_rate(i) = Avg_cl_lop(i) - Avg_cl_lop(i+1);
    Avg_cl_hip_rate(i) = Avg_cl_hip(i) - Avg_cl_hip(i+1);
    Avg_ls_lop_rate(i) = Avg_ls_lop(i) - Avg_ls_lop(i+1);
    Avg_ls_hip_rate(i) = Avg_ls_hip(i) - Avg_ls_hip(i+1);
    Avg_hs_lop_rate(i) = Avg_hs_lop(i) - Avg_hs_lop(i+1);
    Avg_hs_hip_rate(i) = Avg_hs_hip(i) - Avg_hs_hip(i+1);
    Avg_lb_lop_rate(i) = Avg_lb_lop(i) - Avg_lb_lop(i+1);
    Avg_lb_hip_rate(i) = Avg_lb_hip(i) - Avg_lb_hip(i+1);

end

figure(6)
plot(Avg_cl_lop_rate,'b','LineWidth',2)
hold on
plot(Avg_cl_hip_rate,'b')
plot(Avg_ls_lop_rate,'k','LineWidth',2)
plot(Avg_ls_hip_rate,'k')
plot(Avg_hs_lop_rate,'r','LineWidth',2)
plot(Avg_hs_hip_rate,'r')
plot(Avg_lb_lop_rate,'g','LineWidth',2)
plot(Avg_lb_hip_rate,'g')

figure(7)
errorbar(time,Avg_cl_lop,mincllop(:,1),maxcllop(:,1),'b','LineWidth',2)
hold on
errorbar(time,Avg_cl_hip,minclhip(:,1),maxclhip(:,1),'b')
errorbar(time,Avg_ls_lop,minlslop(:,1),maxlslop(:,1),'k','LineWidth',2)
errorbar(time,Avg_ls_hip,minlship(:,1),maxlship(:,1),'k')
errorbar(time,Avg_hs_lop,minhslop(:,1),maxhslop(:,1),'r','LineWidth',2)
errorbar(time,Avg_hs_hip,minhship(:,1),maxhship(:,1),'r')
errorbar(time,Avg_lb_lop,minlblop(:,1),maxlblop(:,1),'g','LineWidth',2)
errorbar(time,Avg_lb_hip,minlbhip(:,1),maxlbhip(:,1),'g')
% errorbar(time,Avg_ls_1p,minls1p(:,1),maxls1p(:,1),'LineWidth',2)
ylabel('Percent intact [ % ]')
xlabel('Distance travelled [ m ]')
% xlim([0 70])
legend('Clear water (Slow)','Clear water (Fast)','1% Sand (Slow)','1% sand (Fast)','10% sand
(Slow)','10% sand (Fast)','1% Ballotini (Slow)','1% Ballotini (Fast)')

%% interpolation station
```

```
x_given = 1:60; %Experiments last for 1 hour

cl_interphi = interp1(time,Avg_cl_hi,x_given,'linear'); %Interpolate points between weight measurements
cl_interplo = interp1(time,Avg_cl_lo,x_given,'linear');
hs_interphi = interp1(time,Avg_hs_hi,x_given,'linear');
hs_interplo = interp1(time,Avg_hs_lo,x_given,'linear');
ls_interphi = interp1(time,Avg_ls_hi,x_given,'linear');
ls_interplo = interp1(time,Avg_ls_lo,x_given,'linear');
lb_interphi = interp1(time,Avg_lb_hi,x_given,'linear');
lb_interplo = interp1(time,Avg_lb_lo,x_given,'linear');

cl_interphip = cl_interphi./max(cl_interphi); %Normalise interpolated weights
cl_interplop = cl_interplo./max(cl_interplo);
hs_interphip = hs_interphi./max(hs_interphi);
hs_interplop = hs_interplo./max(hs_interplo);
ls_interphip = ls_interphi./max(ls_interphi);
ls_interplop = ls_interplo./max(ls_interplo);
lb_interphip = lb_interphi./max(lb_interphi);
lb_interplop = lb_interplo./max(lb_interplo);

figure(8) %Make sure everything looks the same as the other weight figure
plot(x_given(1:30),cl_interphip(1:30))
hold on
plot(x_given(1:30),cl_interplop(1:30))
plot(x_given(1:30),hs_interphip(1:30))
plot(x_given(1:30),hs_interplop(1:30))
plot(x_given(1:30),ls_interphip(1:30))
plot(x_given(1:30),ls_interplop(1:30))
plot(x_given(1:30),lb_interphip(1:30))
plot(x_given(1:30),lb_interplop(1:30))



indclhi = find(cl_interphip>0.6); %Find the index of all weights above 60%
indclhi1 = cl_interphip(indclhi);
indcllo = find(cl_interplop>0.6);
indcllo1 = cl_interplop(indcllo);
indhshi = find(hs_interphip>0.6);
```

```
indhshi1 = hs_interphip(indhshi);
indhslo = find(hs_interplop>0.6);
indhslo1 = hs_interplop(indhslo);
indlbhi = find(lb_interphip>0.6);
indlbhi1 = lb_interphip(indlbhi);
indlblo = find(lb_interplop>0.6);
indlblo1 = lb_interplop(indlblo);
indlshi = find(ls_interphip>0.6);
indlshi1 = ls_interphip(indlshi);
indlslo = find(ls_interplop>0.6);
indlslo1 = ls_interplop(indlslo);

xclhi = 1:length(indclhi1); %Use the length of each array as the time dimension
xcllo = 1:length(indcllo1); %Each interpolated point equals 1 minute
xhshi = 1:length(indhshi1);
xhslo = 1:length(indhslo1);
xlbhi = 1:length(indlbhi1);
xlblo = 1:length(indlblo1);
xlshi = 1:length(indlshi1);
xlslo = 1:length(indlslo1);

figure(9) %Plot the data
plot((xclhi./max(xclhi)),indclhi1,'b') %Normalise the time
hold on
plot((xcllo./max(xcllo)),indcllo1,'b','LineWidth',2)
plot((xlshi./max(xlshi)),indlshi1,'k')
plot((xlslo./max(xlslo)),indlslo1,'k','LineWidth',2)
plot((xhshi./max(xhshi)),indhshi1,'r')
plot((xhslo./max(xhslo)),indhslo1,'r','LineWidth',2)
plot((xlbhi./max(xlbhi)),indlbhi1,'g')
plot((xlblo./max(xlblo)),indlblo1,'g','LineWidth',2)
xlabel('Corresponding Normalised Time [t/max(t)]')
ylabel('Normalised Weight > 60% [wt/max(wt)]')
title('Normalised weight >60% versus corresponding normalised time')
```

Appendix 3: Clay clast images

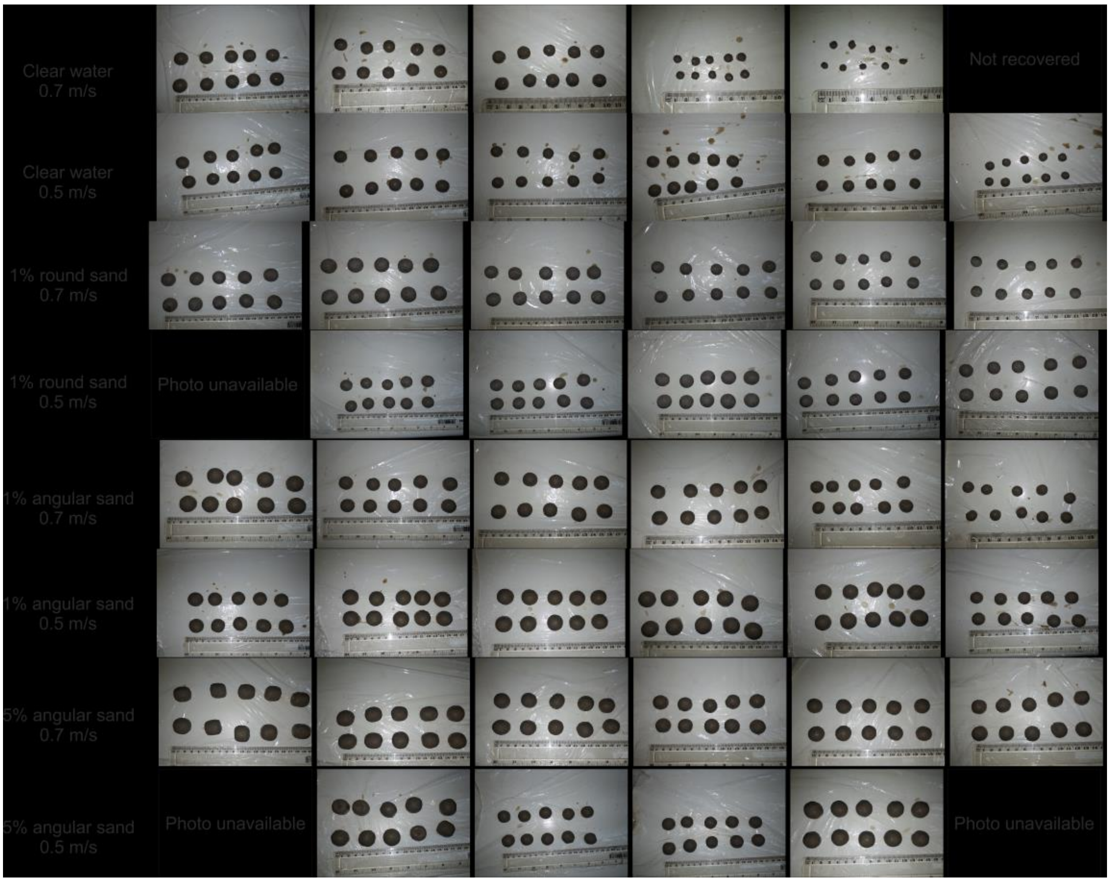

Appendix 4: UDVP Reynolds and Shields parameter script.

```
clear all
close all



%% Import data from text file.
% Script for importing data from the following text file:
%
%    E:\Dense Basal Layers\2014 Lab work\Test11.txt
%
% To extend the code to different selected data or a different text file,
% generate a function instead of a script.

% Auto-generated by MATLAB on 2018/02/27 15:39:03

%% Initialize variables.




for i = 5

filename = sprintf('Test%d.txt',i);
delimiter = '\t';

%% Read columns of data as text:
% For more information, see the TEXTSCAN documentation.
formatSpec =
'%*s%*s%s%s%s%s%s%s%s%s%s%s%s%s%s%s%s%s%s%s%s%s%s%s%s%s%s%s%s%s%s%s%
s%s%s%s%s%s%s%s%s%s%s%s%s%s%s%s%s%s%s%s%s%s%s%s%s%s%s%s%s%s%s%s%s%s
%s%s%s%s%s%s%s%s%s%s%s%s%s%s%s%s%s%s%s%s%s%s%s%s%s%s%s%s%s%s%s%s%s%
s%s%s%s%s%s%s%s%s%s%s%s%s%s%s%s%s%s%s%s%s%s%s%s%s%s%s%s%s%s%s%s%s%s
%s%s%s%s%s%s%s%s%s%s%s%s%s%s%s%s%s%s%s%s%s%s%s%s%s%s%s%s%s%s%s%s%s%
s%s%s%s%s%s%s%s%s%s%s%s%s%s%s%s%s%s%s%s%s%s%s%s%s%s%s%s%s%s%s%s%s%s
%s%s%s%s%s%s%s%s%s%s%s%s%s%s%s%s%s%s%s%s%s%s%s%s%s%s%s%s%s%s%s%s%s%
s%s%s%s%s%s%s%s%s%s%s%s%s%s%s%s%s%s%s%s%s%s%s%s%s%s%s%s%s%s%s%s%s%s
%s%s%s%s%s%s%s%s%s%s%s%s%s%s%s%s%s%s%s%s%s%s%s%s%s%s%s%s%s%s%s%s%s%
s%[^\n\r]';

%% Open the text file.
```

```
fileID = fopen(filename,'r');

%% Read columns of data according to the format.
% This call is based on the structure of the file used to generate this
% code. If an error occurs for a different file, try regenerating the code
% from the Import Tool.
dataArray = textscan(fileID, formatSpec, 'Delimiter', delimiter,  'ReturnOnError', false);

%% Close the text file.
fclose(fileID);

%% Convert the contents of columns containing numeric text to numbers.
% Replace non-numeric text with NaN.
raw = repmat({''},length(dataArray{1}),length(dataArray)-1);
for col=1:length(dataArray)-1
    raw(1:length(dataArray{col}),col) = dataArray{col};
end
numericData = NaN(size(dataArray{1},1),size(dataArray,2));

for col=[1,2,3,4,5,6,7,8,9,10,11,12,13,14,15,16,17,18,19,20,21,22,23,24,25,26,27,28,29,30,31,32,33,34,35,36,37,38,39,40,41,42,43,44,45,46,47,48,49,50,51,52,53,54,55,56,57,58,59,60,61,62,63,64,65,66,67,68,69,70,71,72,73,74,75,76,77,78,79,80,81,82,83,84,85,86,87,88,89,90,91,92,93,94,95,96,97,98,99,100,101,102,103,104,105,106,107,108,109,110,111,112,113,114,115,116,117,118,119,120,121,122,123,124,125,126,127,128,129,130,131,132,133,134,135,136,137,138,139,140,141,142,143,144,145,146,147,148,149,150,151,152,153,154,155,156,157,158,159,160,161,162,163,164,165,166,167,168,169,170,171,172,173,174,175,176,177,178,179,180,181,182,183,184,185,186,187,188,189,190,191,192,193,194,195,196,197,198,199,200,201,202,203,204,205,206,207,208,209,210,211,212,213,214,215,216,217,218,219,220,221,222,223,224,225,226,227,228,229,230,231,232,233,234,235,236,237,238,239,240,241,242,243,244,245,246,247,248,249,250,251,252,253,254,255,256,257,258,259,260,261,262,263,264,265,266,267,268,269,270,271,272,273,274,275,276,277,278,279,280,281,282,283,284,285,286,287,288,289,290,291,292,293,294,295,296,297,298,299]
    % Converts text in the input cell array to numbers. Replaced non-numeric
    % text with NaN.
    rawData = dataArray{col};
    for row=1:size(rawData, 1);
        % Create a regular expression to detect and remove non-numeric prefixes and
        % suffixes.
        regexstr = '(?<prefix>.*?)(?<numbers>([-]*(\d+[\,]*)+[\.]{0,1}\d*[eEdD]{0,1}[-+]*\d*[i]{0,1})|([-]*(\d+[\,]*)*[\.]{1,1}\d+[eEdD]{0,1}[-+]*\d*[i]{0,1}))(?<suffix>.*)';
```

```
        try
            result = regexp(rawData{row}, regexstr, 'names');
            numbers = result.numbers;

            % Detected commas in non-thousand locations.
            invalidThousandsSeparator = false;
            if any(numbers==',');
                thousandsRegExp = '^\d+?(\,\d{3})*\.{0,1}\d*$';
                if isempty(regexp(numbers, thousandsRegExp, 'once'));
                    numbers = NaN;
                    invalidThousandsSeparator = true;
                end
            end
            % Convert numeric text to numbers.
            if ~invalidThousandsSeparator;
                numbers = textscan(strrep(numbers, ',', ''), '%f');
                numericData(row, col) = numbers{1};
                raw{row, col} = numbers{1};
            end
        catch me
        end
    end
end


%% Replace non-numeric cells with NaN
R = cellfun(@(x) ~isnumeric(x) && ~islogical(x),raw); % Find non-numeric cells
raw(R) = {NaN}; % Replace non-numeric cells

%% Create output variable
eval(['Test' num2str(i) ' = cell2mat(raw);'])
%% Clear temporary variables
clearvars filename delimiter formatSpec fileID dataArray ans raw col numericData rawData row regexstr result numbers invalidThousandsSeparator thousandsRegExp me R;



eval(['Test1 = (Test' num2str(i) '(400:800,:))./-1000;'])
eval(['Test' num2str(i) 'Min = min(Test1(:,(1:228)));'])
```

```
eval(['Test' num2str(i) 'Max = max(Test1(:,(1:228)));'])
Test2 = mean(Test1,1);

for j=1:length(Test1);
   TurbData(j,:)=Test1(j,:)-Test2; % subtract the mean profile from each profile of the dataset
end

TurbDataAbs=(TurbData.^2).^(1/2);

MeanTurbProf=mean(TurbDataAbs);

eval(['MeanTurbProf' num2str(i) '= MeanTurbProf;'])



eval(['v' num2str(i) '= Test2(1:228);'])



for j = 1:228

   d(j) = 3.75+0.75*(j);

end



d2 = ((d.*cosd(30))-160)*-1;

logy = log(d2(218:228));
eval(['vhuCr' num2str(i) '= v' num2str(i) '(218:228);'])

nonan = 10;

eval(['num=nonan.*nansum(vhuCr' num2str(i) '.*logy)-nansum(vhuCr' num2str(i) ').*nansum(logy);'])
den=nonan.*nansum(logy.^2)-(nansum(logy)).^2;
eval(['uCr' num2str(i) '=num./(2.5*den);'])

eval(['cte' num2str(i) '=uCr' num2str(i) '^2./v' num2str(i) '.^2;'])
%% Calculation of Rep and Shield parameter
```

```
% Rep=u*particle diameter/seawater viscosity
% clear ('Rep','Shp');
Dp = 0.02;
%Dp = 0.00016; %grain size [m]
Vs=1.5*10^-6; %kinematic viscosity of seawater [m2/s]


eval(['Rep' num2str(i) '=uCr' num2str(i) '*Dp/Vs;'])

% Shield parameter Shp=u*^2/((sed density/seawater density-1)gravity
% constant*particle diameter
dsed = 1300;
%dsed=2650;%input('Density of sediment [gr/l]? ');
dsw=1027;%input('Density of seawater [gr/l]? ');
eval(['Shp' num2str(i) '=uCr' num2str(i) '.^2/((dsed/dsw-1)*9.81*Dp);'])





%%
%
% Rep = [Rep6 Rep8 Rep10 Rep11];
% Shp = [Shp6 Shp8 Shp10 Shp11];
%
%
% o = 'o';
%
% figure
% loglog(Rep,Shp,'o')
% xlim([0.1 1000]);
% ylim([0.001 10]);
% grid on
% % legend('Test06','Test08','Test10','Test11')
% xlabel('Re_p')
% ylabel('Sh_p')
%
%
% figure
```

```
% plot(v,d2,'-o')
% hold on
% plot(Test11Min(1:228),d2)
% plot(Test11Max(1:228),d2)
% % xlim([0.5 0.8])
% % ylim([0 30])
%
% figure
% semilogy(v(218:228),d2(218:228),'-o')
% xlim([0.4 0.7])
%
%
eval(['boundaryvel' num2str(i) '= v' num2str(i) '(218:228);'])
eval(['logz' num2str(i) '= log(d2(218:228));'])
dz= d2(218:228);
d = (d-9);
end

plot(v5,(d./1000))
ylim([0 0.17])
xlim([0 0.8])
xlabel('Velocity [ms^-^1]')
ylabel('Height [m]')
```

Bibliography

Aldridge, T.R., and Carrington, T.M., 2010, BP Clair phase 1 - Pile driveability and capacity in extremely hard till: Frontiers in Offshore Geotechnics II, ISFOG 2010 - Proceedings, p. 477–482, doi: doi:10.1201/b10132-60 10.1201/b10132-60.

Ayranci, K., Lintern, D.G., Hill, P.R., and Dashtgard, S.E., 2012, Tide-supported gravity flows on the upper delta front, Fraser River delta, Canada: Marine Geology, v. 326–328, p. 166–170, doi: 10.1016/j.margeo.2012.09.007.

Azpiroz-Zabala, M., Cartigny, M.J.B., Talling, P.J., Parsons, D.R., Sumner, E.J., Clare, M.A., Simmons, S.M., Cooper, C., and Pope, E.L., 2017, Newly recognized turbidity current structure can explain prolonged flushing of submarine canyons: Science Advances, v. 3, doi: 10.1126/sciadv.1700200.

Baas, J.H., and Best, J.L., 2008, The dynamics of turbulent, transitional and laminar clay-laden flow over a fixed current ripple: Sedimentology, v. 55, p. 635–666, doi: 10.1111/j.1365-3091.2007.00916.x.

Baas, J.H., Best, J.L., and Peakall, J., 2011, Depositional processes, bedform development and hybrid bed formation in rapidly decelerated cohesive (mud-sand) sediment flows: Sedimentology, v. 58, p. 1953–1987, doi: 10.1111/j.1365-3091.2011.01247.x.

Bagnold, R.A., 1954, Experiments on a Gravity-Free Dispersion of Large Solid Spheres in a Newtonian Fluid under Shear: Proceedings of the Royal Society A: Mathematical, Physical and Engineering Sciences, v. 225, p. 49–63, doi: 10.1098/rspa.1954.0186.

Baltzer, A., Cochonat, P., and Piper, D.J.W., 1994, In situ geotechnical characterization of sediments on the Nova Scotian Slope, eastern Canadian continental margin: Marine Geology, v. 120, p. 291–308, doi: 10.1016/0025-3227(94)90063-9.

Bath Enright, O.G., Minter, N.J., and Sumner, E.J., 2017, Palaeoecological implications of the preservation potential of soft-bodied organisms in sediment-density flows: testing turbulent waters: Royal Society Open Science, v. 4, p. 170212, doi: 10.1098/rsos.170212.

Bell, H.S., 1940, Armored mud balls: Their origin, properties and role in sedimentation: Geology, v. 48, p. 1–31.

Bolton, G.T., Qiu, C.H., and Wang, M., 2002, A novel Electrical Tomography Sensor for Monitoring the Phase Distribution in Industrial Reactors: Fluid mixing VII, p. 10–11.

Booij, R., 2003, Measurements and large eddy simulations of the flows in some curved flumes: v. 4, p. 37–41.

Bouma, A.H., 1962, Sedimentology of some flysch deposits: A graphic approach to facies interpretation: Amsterdam, Elsevier, 168 p.

Bruschi, R., Bughi, S., Spinazzé, M., Torselletti, E., and Vitali, L., 2006, Impact of debris flows and turbidity currents on seafloor structures: Norsk Geologisk Tidsskrift, v. 86, p. 317–336.

Carter, L., Gavey, R., Talling, P.J., and Liu, J.T., 2014, Insights into submarine geohazards from breaks in subsea telecommunication cables: Oceanography, v. 24, p. 58–67, doi: 10.5670/oceanog.2011.65.

Cartigny, M.J.B., Eggenhuisen, J.T., Hansen, E.W.M., and Postma, G., 2013, Concentration-Dependent Flow Stratification In Experimental High-Density Turbidity Currents and Their Relevance To Turbidite Facies Models: Journal of Sedimentary Research, v. 83, p. 1046–1064, doi: 10.2110/jsr.2013.71.

Chang, A.S., and Grimm, K.A., 1999, Speckled beds: distinctive gravity-flow deposits in finely laminated diatomaceous sediments, Miocene Monterey Formation, California: Journal of Sedimentary Research, v. 69, p. 122–134, doi: 10.2110/jsr.69.122.

Chi, K., Zakeri, A., and Hawlader, B., 2012, Impact drag forces on pipelines caused by submarine glide blocks or out-runner blocks, *in* Yamada, Y., Kawamura, K., Ikehara, K., Ogawa, Y., Urgeles, R., Mosher, D., Chaytor, J., and Strasser, M. eds., Submarine Mass Movements and Their Consequences, Dordrecht, Springer Netherlands, p. 429–440, doi: 10.1007/978-94-007-2162-3.

Chun, S.S., Choe, M.Y., and Chough, S.K., 2002, Armored mudstone boulders in submarine debris-flow deposits, the Hunghae Formation, Pohang Basin: An evidence for the large-scale slumping of adjacent area of a submarine channel or scar wall: Geosciences Journal, v. 6, p. 215–225, doi: 10.1007/BF02912692.

Clare, M.A., Hughes Clarke, J.E., Talling, P.J., Cartigny, M.J.B., and Pratomo, D.G., 2016, Preconditioning and triggering of offshore slope failures and turbidity currents revealed by most detailed monitoring yet at a fjord-head delta: Earth and Planetary Science Letters, v. 450, p. 208–220, doi: 10.1016/j.epsl.2016.06.021.

Dade, W.B., and Huppert, H.E., 1998, Long-runout rockfalls: Geology, v. 26, p. 803–806, doi: 10.1130/0091-7613(1998)026<0803:LRR>2.3.CO.

Dasgupta, S., and Buatois, L., 2012, Unusual occurrence and stratigraphic significance of the Glossifungites ichnofacies in a submarine paleo-canyon — Example from a Pliocene shelf-edge delta, Southeast Trinidad: Sedimentary Geology, v. 269–270, p. 69–77, doi: 10.1016/j.sedgeo.2012.06.004.

Dick, J.E., and Sleath, J.F.A., 1991, Velocities and concentrations in oscillatory flow over beds of sediment: Journal of Fluid Mechanics, v. 233, p. 165, doi: 10.1017/S0022112091000447.

Dickas, A.B., and Lunking, W., 1968, The origin and destruction of armored mud balls in a fresh-water lacustrine environment, Lake Superior: Journal of Sedimentary Petrology, v. 38, p. 1366–1370, doi: https://doi.org/10.1306/74D71B9F-2B21-11D7-8648000102C1865D.

Dickin, F., and Wang, M., 1996, Electrical resistance tomography for process applications: Meas. Sci. Technol., v. 7, p. 247-–260, doi: 10.1088/0957-0233/7/3/005.

Dietrich, P., Ghienne, J.-F., Normandeau, A., and Lajeunesse, P., 2016, Upslope-Migrating Bedforms In A Proglacial Sandur Delta: Cyclic Steps From River-Derived Underflows? Journal of Sedimentary Research, v. 86, p. 113–123, doi: 10.2110/jsr.2016.4.

Dohmen-Janssen, C.M., 2002, Sheet flow dynamics under monochromatic nonbreaking waves: Journal of Geophysical Research, v. 107, p. 13–21, doi: 10.1029/2001JC001045.

Dyakowski, T., Jeanmeure, L.F.C., and Jaworski, A.J., 2000, Applications of electrical tomography for gas – solids and liquid – solids flows — a review: Powder Technology, v. 112, p. 174–192, doi: 10.1016/S0032-5910(00)00292-8.

Eggenhuisen, J.T., Cartigny, M.J.B., and De Leeuw, J., 2017, Physical theory for near-bed turbulent particle suspension capacity: Earth Surface Dynamics, v. 5, p. 269–281, doi: 10.5194/esurf-5-269-2017.

Felix, M., Leszczyński, S., Ślaczka, A., Uchman, A., Amy, L., and Peakall, J., 2009, Field expressions of the transformation of debris flows into turbidity currents, with examples from the Polish Carpathians and the French Maritime Alps: Marine and Petroleum Geology, v. 26, p. 2011–2020, doi: 10.1016/j.marpetgeo.2009.02.014.

Felix, M., and Peakall, J., 2006, Transformation of debris flows into turbidity currents: mechanisms inferred from laboratory experiments: Sedimentology, v. 53, p. 107–123, doi: 10.1111/j.1365-3091.2005.00757.x.

Felix, M., Sturton, S., and Peakall, J., 2005, Combined measurements of velocity and concentration in experimental turbidity currents: Sedimentary Geology, v. 179, p. 31–47, doi: 10.1016/j.sedgeo.2005.04.008.

Fisher, R., 1983, Flow transformations in sediment gravity flows: Geology, v. 11, p. 273–274.

Fonnesu, M., Felletti, F., Haughton, P.D.W., Patacci, M., and McCaffrey, W.D., 2018, Hybrid event bed character and distribution linked to turbidite system sub-environments: The North Apennine Gottero Sandstone (north-west Italy): Sedimentology, v. 65, p. 151–190, doi: 10.1111/sed.12376.

Fonnesu, M., Haughton, P., Felletti, F., and McCaffrey, W., 2015, Short length-scale variability of hybrid event beds and its applied significance: Marine and Petroleum Geology, v. 67, p. 583–603, doi: 10.1016/j.marpetgeo.2015.03.028.

Fonnesu, M., Patacci, M., Haughton, P.D.W., and Felletti, F., 2016, Hybrid event beds generated by local substrate delamination on a confined basin floor: Journal of Sedimentary Research, v. 86, p. 929–943.

Galy, V., France-Lanord, C., Beyssac, O., Faure, P., Kudrass, H., and Palhol, F., 2007, Efficient organic carbon burial in the Bengal fan sustained by the Himalayan erosional system: Nature, v. 450, p. 407–410.

Gao, P., 2008, Transition between Two Bed-Load Transport Regimes : Saltation and Sheet Flow: Journal of Hydraulic Engineering, v. 134, p. 340–349, doi: 10.1061/(ASCE)0733-9429(2008)134:3(340).

Girardclos, S., Schmidt, O., Sturm, M., Ariztegui, D., Pugin, A., and Anselmetti, F., 2007, The 1996 AD delta collapse and large turbidite in Lake Brienz: Marine Geology, v. 241, p. 137–154.

Goldfinger, C., 2011, Submarine paleoseismology based on turbidite records: Annual Review of Marine Science, v. 3, p. 35–66.

Goldschmidt, P.M., 1994, Armoured and unarmoured till balls from the Greenland Sea floor: Marine Geology, v. 121, p. 121–128.

Haflidason, H., Sejrup, H.P., Nygård, A., Mienert, J., Bryn, P., Lien, R., Forsberg, C.F., Berg, K., and Masson, D., 2004, The Storegga Slide: Architecture, geometry and slide development: Marine Geology, v. 213, p. 201–234, doi:

10.1016/j.margeo.2004.10.007.

Hampton, M.A., 1975, Competence of fine-grained debris flows: Journal of Sedimentary Petrology, v. 45, p. 834–844.

Haughton, P.D.W., Barker, S.P., and McCaffrey, W.D., 2003, “Linked” debrites in sand-rich turbidite systems - Origin and significance: Sedimentology, v. 50, p. 459–482, doi: 10.1046/j.1365-3091.2003.00560.x.

Haughton, P., Davis, C., McCaffrey, W., and Barker, S., 2009, Hybrid sediment gravity flow deposits - Classification, origin and significance: Marine and Petroleum Geology, v. 26, p. 1900–1918, doi: 10.1016/j.marpetgeo.2009.02.012.

Heezen, B.C., and Ewing, M., 1952, Turbidity currents and submarine slumps, and the 1929 Grand Banks earthquake: American Journal of Science, v. 250, p. 849–873.

Hermidas, N., Eggenhuisen, J.T., Jacinto, R.S., Luthi, S.M., Toth, F., and Pohl, F., 2018, A Classification of Clay-Rich Subaqueous Density Flow Structures: Journal of Geophysical Research, v. 123, p. 945–966, doi: 10.1002/2017JF004386.

Hickin, E.J., 1989, Contemporary Squamish River sediment flux to Howe Sound, British Columbia: Canadian Journal of Earth Sciences, v. 26, p. 1953–1963, doi: https://doi.org/10.1139/e89-165.

Hiscott, R.N., 1994, Traction-Carpet Stratification in Turbidites-Fact or Fiction? Journal of Sedimentary Research, v. A64, p. 204–208.

Hoverstein, G.M., Dey, A., and Morrison, H.F., 1982, Comparison of five least-squares inversion techniques in resistivity sounding: Geophysical Prospecting, v. 30, p. 688–715.

Hughes Clarke, J.E., 2016, First wide-angle view of channelized turbidity currents links migrating cyclic steps to flow characteristics: Nature Communications, v. 7, p. 11896, doi: 10.1038/ncomms11896.

Hughes Clarke, J.E., Brucker, S., Muggah, J., Hamilton, T., Cartwright, D., Church, I., and Kuus, P., 2012, Temporal progression and spatial extent of mass wasting events on the Squamish prodelta slope, *in* Landslides and Engineered Slopes: Protecting Society through Improved Understanding, v. 122, p. 1091–1096.

Hughes Clarke, J.E., Marques, C.R. V., and Pratomo, D., 2014, Imaging Active Mass-Wasting and Sediment Flows on a Fjord Delta, Squamish, British Columbia: Springer Internaitonal Publishing, p. 249–260, doi: 10.1007/978-3-319-02904-7.

Jackson, C., and Johnson, H.D., 2009, Sustained turbidity currents and their interaction with debrite-related topography; Labuan Island, offshore NW Borneo, Malaysia: Sedimentary Geology, v. 219, p. 77–96, doi: 10.1016/j.sedgeo.2009.04.008.

Jackson, C., Zakaria, A.A., Johnson, H.D., Tongkul, F., and Crevello, P.D., 2009, Sedimentology, stratigraphic occurrence and origin of linked debrites in the West Crocker Formation (Oligo-Miocene), Sabah, NW Borneo: Marine and Petroleum Geology, v. 26, p. 1957–1973, doi: 10.1016/j.marpetgeo.2009.02.019.

Jiang, Z., 1995, The motion of sediment–water mixtures during intense bedload transport: computer simulations: Sedimentology, v. 42, p. 935–945.

Kane, I.A., and Pontén, A.S.M., 2012, Submarine transitional flow deposits in the Paleogene Gulf of Mexico: Geology, v. 40, p. 1119–1122, doi: 10.1130/G33410.1.

Kineke, G.C., Sternberg, R.W., Trowbridge, J.H., and Geyer, W.R., 1996, Fluid-mud processes on the Amazon continental shelf: Continental Shelf Research, v. 16, p. 667–696, doi: 10.1016/0278-4343(95)00050-X.

Kineke, G.C., Woolfe, K.J., Kuehl, S.A., Milliman, J.D., Dellapenna, T.M., and Purdon, R.G., 2000, Sediment export from the Sepik River, Papua New Guinea: Evidence for a divergent sediment plume: Continental Shelf Research, v. 20, p. 2239–2266, doi: 10.1016/S0278-4343(00)00069-8.

Kooistra, A., Verhoef, P.N.W., Broere, W., Ngan-Tillard, D.J.M., and van Tol, A.N., 1998, Appraisal of stickiness of natural clays from laboratory tests: Delft, Netherlands, 101–113 p.

Kostaschuk, R. a., Stephan, B. a., and Luternauer, J.L., 1993, Suspended sediment concentration in a buoyant plume: Fraser River, Canada: Geo-Marine Letters, v. 13, p. 165–171, doi: 10.1007/BF01593190.

Kranenburg, C., and Winterwerp, J.C., 1997, Erosion of fluid mud layers: Journal of Hydraulic Engineering, v. 123, p. 504–511, doi: 10.1061/(ASCE)0733-9429(1997)123:6(512).

Kuenen, H., 1966, Experimental turbidite lamination in a circular flume: The Journal of Geology, v. 74, p. 523–545.

Kuenen, H., 1951, Properties of turbidity currents of high density (J. L. Hough, Ed.): Society of Economic Paleontologists and Mineralogists, v. 2, 14–33 p.

Kuenen, H., and Migliorini, C.I., 1950, Turbidity Currents as a Cause of Graded

Bedding: Geology, v. 58, p. 91–127.

Kuo, M., and Bolton, M., 2013, The nature and origin of deep ocean clay crust from the Gulf of Guinea: Géotechnique, v. 63, p. 500–509, doi: 10.1680/geot.10.P.012.

Lambot, S., Slob, E.C., Vanclooster, M., and Vereecken, H., 2006, Closed loop GPR data inversion for soil hydraulic and electric property determination: Geophysical Research Letters, v. 33, p. 1–5, doi: 10.1029/2006GL027906.

Lanckriet, T., Puleo, J.A., Masselink, G., Turner, I.L., Conley, D., Blenkinsopp, C., and Russell, P., 2014, Comprehensive Field Study of Swash-Zone Processes. II: Sheet Flow Sediment Concentrations during Quasi-Steady Backwash: Journal of Waterway, Port, Coastal, and Ocean Engineering, v. 140, p. 29–42, doi: 10.1061/(ASCE)WW.1943-5460.0000209.

Lanckriet, T., Puleo, J.A., and Waite, N., 2013, A conductivity concentration profiler for sheet flow sediment transport: IEEE Journal of Oceanic Engineering, v. 38, p. 55–70, doi: 10.1109/JOE.2012.2222791.

Landauer, R., 1952, The Electrical Resistance of Binary Metallic Mixtures: Journal of Applied Physics, v. 779, p. 779–784.

Lavoué, F., Van Der Kruk, J., Rings, J., André, F., Moghadas, D., Huisman, J.A., Lambot, S., LWeihermüller, Vanderborght, J., and Vereecken, H., 2010, Electromagnetic induction calibration using apparent electrical conductivity modelling based on electrical resistivity tomography: Near Surface Geophysics, v. 8, p. 553–561, doi: 10.3997/1873-0604.2010037.

De Leeuw, J., Eggenhuisen, J.T., and Cartigny, M.J.B., 2016, Morphodynamics of submarine channel inception revealed by new experimental approach: Nature Communications, v. 7, p. 1–7, doi: 10.1038/ncomms10886.

Lewin, J., and Brewer, P.A., 2002, Laboratory simulation of clast abrasion: Earth Surface Processes and Landforms, v. 27, p. 145–164, doi: 10.1002/esp.306.

Lintern, D.G., Hill, P.R., and Stacey, C., 2016, Powerful unconfined turbidity current captured by cabled observatory on the Fraser River delta slope, British Columbia, Canada: International Association of Sedimentologists Special Publications, p. 1041–1064, doi: 10.1111/sed.12262.

Little, R.D., 1982, Lithified armored mud balls of the Lower Jurassic Turners Falls sandstone, North-Central Massachusetts: Geology, v. 90, p. 203–207.

Lowe, D.R., 1976, Subaqueous liquefied and fluidized sediment flows and their deposits: Sedimentology, v. 23, p. 285–308, doi: 10.1111/j.1365-3091.1976.tb00051.x.

Lowe, D.R., 1988, Suspended-load fallout rate as an independent variable in the analysis of current structures: Sedimentology, v. 35, p. 765–776, doi: 10.1111/j.1365-3091.1988.tb01250.x.

Malarkey, J., Baas, J.H., Hope, J.A., Aspden, R.J., Parsons, D.R., Peakall, J., Paterson, D.M., Schindler, R.J., Ye, L., Lichtman, I.D., Bass, S.J., Davies, A.G., Manning, A.J., and Thorne, P.D., 2015, The pervasive role of biological cohesion in bedform development: Nature Communications, v. 6, p. 1–6, doi: 10.1038/ncomms7257.

Marwala, T., 2010, Finite-element-model Updating Using Nelder–Mead Simplex and Newton Broyden–Fletcher–Goldfarb–Shanno Methods, *in* Finite-element-model Updating Using Computional Intelligence Techniques, p. 25–47, doi: 10.1007/978-1-84996-323-7_2.

Mastbergen, D.R., and Van Den Berg, J.H., 2003, Breaching in fine sands and the generation of sustained turbidity currents in submarine canyons: Sedimentology, v. 50, p. 625–637, doi: 10.1046/j.1365-3091.2003.00554.x.

Mather, A., Stokes, M., Pirrie, D., and Hartley, R., 2008, Generation, transport and preservation of armoured mudballs in an ephemeral gully system: Geomorphology, v. 100, p. 104–119, doi: 10.1016/j.geomorph.2007.10.030.

Meadows, A., and Meadows, P.S., 1994, Bioturbation in deep sea Pacific sediments: Journal of the Geological Society of London, v. 151, p. 361–375, doi: 10.1144/gsjgs.151.2.0361.

Milliman, J., and Farnsworth, K., 2013, River Discharge to the Coastal Ocean: A Global Synthesis: Cambridge University Press, v. 24, p. 143–160, doi: 10.5670/oceanog.2011.108.

Mueller, P., Patacci, M., and Di Giulio, A., 2017, Hybrid event beds in the proximal to distal extensive lobe domain of the coarse-grained and sand-rich Bordighera turbidite system (NW Italy): Marine and Petroleum Geology, v. 86, p. 908–931, doi: 10.1016/j.marpetgeo.2017.06.047.

Mulder, T., and Alexander, J., 2001, The physical character of subaqueous sedimentary density flows and their deposits: Sedimentology, v. 48, p. 269–299, doi: 10.1046/j.1365-3091.2001.00360.x.

Mulder, T., and Syvitski, J.P.M., 1995, Turbidity Currents Generated At River

Mouths During Exceptional Discharges To the World Oceans: Journal of Geology, v. 103, p. 285–299.

Mulder, T., Syvitski, J.P.M., Migeon, S., Faugères, J.-C., and Savoye, B., 2003, Marine hyperpycnal flows: initiation, behavior and related deposits. A review: Marine and Petroleum Geology, v. 20, p. 861–882, doi: 10.1016/j.marpetgeo.2003.01.003.

Nelder, J.A., and Mead, R., 1965, A simplex method for function minimization: The Computer Journal, v. 7, p. 308–313.

Noel, M., and Xu, B., 1991, Archeological investigation by electrical resistivity tomography: A preliminary study: J. Geoph. Int., v. 107, p. 95–102.

Normandeau, A., Lajeunesse, P., St-Onge, G., Bourgault, D., Drouin, S.S.O., Senneville, S., and B??langer, S., 2014, Morphodynamics in sediment-starved inner-shelf submarine canyons (Lower St. Lawrence Estuary, Eastern Canada): Marine Geology, v. 357, p. 243–255, doi: 10.1016/j.margeo.2014.08.012.

North, L., Best, A.I., Sothcott, J., and Macgregor, L., 2013, Laboratory determination of the full electrical resistivity tensor of heterogeneous carbonate rocks at elevated pressures: Geophysical Prospecting, v. 61, p. 458–470, doi: 10.1111/j.1365-2478.2012.01113.x.

Nossin, J.J., 1961, Occurrence and origin of clay pebbles on the East Coast of Johore, Malaya: Journal of Sedimentary Petrology, v. 31, p. 437–447, doi: https://doi.org/10.1306/74D70B91-2B21-11D7-8648000102C1865D.

O’Donoghue, T., and Wright, S., 2004, Concentrations in oscillatory sheet flow for well sorted and graded sands: Coastal Engineering, v. 50, p. 117–138, doi: 10.1016/j.coastaleng.2003.09.004.

Obelcz, J., Xu, K., Georgiou, I.Y., Maloney, J., Bentley, S.J., and Miner, M.D., 2017, Sub-decadal submarine landslides are important drivers of deltaic sediment flux: Insights from the Mississippi River Delta Front: Geology, v. 45, p. G38688.1, doi: 10.1130/G38688.1.

Ojakangas, R.W., and Thompson, J.A., 1977, Modern Armored Mud Balls in an Urban Environment: Journal of Sedimentary Petrology, v. 47, p. 1630–1633.

Pantin, H.M., 1979, Interaction between velocity and effective density in turbidity flow: Phase-plane analysis with criteria for autosuspension: Marine Geology, v. 31, p. 59–99.

Pantin, H.M., 1967, The origin of water-borne diamictons and their relation to turbidites: New Zealand Journal of Marine and Freshwater Research, v. 1, p. 118–138, doi: 10.1080/00288330.1967.9515198.

Parker, G., Fukushima, Y., and Pantin, H.M., 1986, Self-accelerating turbidity currents: J. Fluid Mech., v. 171, p. 145–181.

Parsons, J.D., Bush, J.W.M., and Syvitski, J.P.M., 2001, Hyperpycnal plume formation from riverine outflows with small sediment concentrations: Sedimentology, v. 48, p. 465–478, doi: 10.1046/j.1365-3091.2001.00384.x.

Patacci, M., Haughton, P.D.W., and Mccaffrey, W.D., 2014, Rheological complexity in sediment gravity flows forced to decelerate against a confining slope , Braux , SE France: Journal of Sedimentary Research, v. 84, p. 270–277.

Patacci, M., Haughton, P.D.W., and McCaffrey, W.D., 2014, Rheological complexity in sediment gravity flows forced to decelerate against a confining slope , Braux , SE France: Journal of Sedimentary Research, v. 84, p. 270–277.

Patel, M., Deshpande, V., and Kumar, B., 2015, Turbulent characteristics and evolution of sheet flow in an alluvial channel with downward seepage: Geomorphology, v. 248, p. 161–171, doi: 10.1016/j.geomorph.2015.07.042.

Paull, C.K., Talling, P.J., Maier, K.L., Parsons, D., Xu, J., Caress, D.W., Gwiazda, R., Lundsten, E.M., Anderson, K., Barry, J.P., Chaffey, M., O’Reilly, T., Rosenberger, K.J., Gales, J.A., et al., 2018, Powerful turbidity currents driven by dense basal layers: Nature Communications, p. 1–9, doi: 10.1038/s41467-018-06254-6.

Pettijohn, F.J., 1957, Sedimentary Rocks: New York, Harper and Bros., 718 p.

Peucker-Ehrenbrink, B., 2009, Land2Sea database of river drainage basin sizes, annual water discharges, and suspended sediment fluxes: Geochemistry, Geophysics, Geosystems, v. 10, p. 1–10, doi: 10.1029/2008GC002356.

Piper, D.J.W., and Aksu, A.E., 1987, The source and origin of the 1929 grand banks turbidity current inferred from sediment budgets: Geo-Marine Letters, v. 7, p. 177–182, doi: 10.1007/BF02242769.

Piper, D.J.W., Cochonat, P., and Morrison, M.L., 1999, The sequence of events around the epicenter of the 1929 Grand Banks earthquake: Initiation of debris flows and turbidity currents inferred from sidescan sonar: Sedimentology, v. 46, p. 79–97.

Polydorides, N., and Lionheart, W.R.B., 2002, A Matlab toolkit for three-dimensional electrical impedance tomography: A contribution to the Electrical Impedance and Diffuse Optical Reconstruction Software project: Measurement Science and Technology, v. 13, p. 1871–1883, doi: 10.1088/0957-0233/13/12/310.

Ponce, J.J., and Carmona, N., 2011, Coarse-grained sediment waves in hyperpycnal clinoform systems, Miocene of the Austral foreland basin, Argentina: Geology, v. 39, p. 763–766, doi: 10.1130/G31939.1.

Postma, G., Nemec, W., and Kleinspehn, K.L., 1988, Large floating clasts in turbidites: a mechanism for their emplacement: Sedimentary Geology, v. 58, p. 47–61, doi: 10.1016/0037-0738(88)90005-X.

Prior, D.B., Wiseman, W.J., and Gilbert, R., 1981, Submarine slope processes on a fan delta, Howe Sound, British Columbia: Geo-Marine Letters, v. 1, p. 85–90, doi: 10.1007/BF02463323.

Provenzano, G., Vardy, M.E., and Henstock, T.J., 2017, Pre-stack full waveform inversion of ultra-high-frequency marine seismic reflection data: Geophysical Journal International, v. 209, p. 1593–1611, doi: 10.1093/gji/ggx114.

Puleo, J.A., Faries, J., Davidson, M., and Hicks, B., 2010, A conductivity sensor for nearbed sediment concentration profiling: Journal of Atmospheric and Oceanic Technology, v. 27, p. 397–408, doi: 10.1175/2009JTECHO718.1.

Ribberink, J.S., 1998, Bed-load transport for steady flows and unsteady oscillatory flows: Coastal Engineering, v. 34, p. 59–82, doi: 10.1016/S0378-3839(98)00013-1.

Van Rijn, L.C., 1993, Principles of sediment transport in rivers: Aqua Publications.

Saucier, F.J., and Chassé, J., 2000, Tidal circulation and buoyancy effects in the St. Lawrence Estuary: Atmosphere-Ocean, v. 38, p. 505–556, doi: 10.1080/07055900.2000.9649658.

Schieber, J., 2016, Experimental testing of the transport-durability of shale lithics and its implications for interpreting the rock record: Sedimentary Geology, v. 331, p. 162–169, doi: 10.1016/j.sedgeo.2015.11.006.

Schieber, J., Southard, J.B., and Schimmelmann, A., 2010, Lenticular shale fabrics resulting from intermittent erosion of water-rich muds - interpreting the rock record in the light of recent flume experiments: Journal of Sedimentary Reseach, v. 80, p. 119–128, doi: 10.2110/jsr.2010.005.

Schwab, W.C., Lee, H.J., Twichell, D.C., Locat, J., Nelson, C.H., McArthur, W.G., and Kenyon, N.H., 1996, Sediment mass-flow processes on a depositional lobe, outer Mississippi Fan: Journal of Sedimentary Research, v. 66, p. 916–927, doi:

10.1306/D426843C-2B26-11D7-8648000102C1865D.

Sequeiros, O.E., Naruse, H., Endo, N., Garcia, M.H., and Parker, G., 2009, Experimental study on self-accelerating turbidity currents: Journal of Geophysical Research, v. 114, p. C05025, doi: 10.1029/2008JC005149.

Sequeiros, O.E., Spinewine, B., Beaubouef, R.T., Sun, T., Garcia, M.H., and Parker, G., 2010, Bedload transport and bed resistance associated with density and turbidity currents: Sedimentology, v. 57, p. 1463–1490, doi: 10.1111/j.1365-3091.2010.01152.x.

Shao, Y., Hung, C., and Chou, Y., 2017, Numerical study of convective sedimentation through a sharp density interface: Journal of Fluid Mechanics, v. 824, p. 513–549, doi: 10.1017/jfm.2017.349.

Smith, N.D., 1972, Flume Experiments on the Durability of Mud Clasts: Journal of Sedimentary Petrology, v. 42, p. 378–383, doi: 10.1306/74D72559-2B21-11D7-8648000102C1865D.

Sohn, Y.K., 1997, On Traction-Carpet Sedimentation: Journal of Sedimentary Research, v. 67, p. 502–509.

Southern, S.J., Patacci, M., Felletti, F., and McCaffrey, W.D., 2015, Influence of flow containment and substrate entrainment upon sandy hybrid event beds containing a co-genetic mud-clast-rich division: Sedimentary Geology, v. 321, p. 105–122.

Stanley, D.J., 1969, Armored mud balls in an intertidal environment, Minas Basin, Southeast Canada: Geology, v. 77, p. 683–693.

Stanley, D.J., 1964, Large mudstone-nucleus sandstone spheroids in submarine channel deposits: Journal of Sedimentary Petrology, v. 34, p. 672–676.

Stevenson, C.J., Feldens, P., Georgiopoulou, A., Schönke, M., Krastel, S., Piper, D.J.W., Lindhorst, K., and Mosher, D., 2018, Reconstructing the sediment concentration of a giant submarine gravity flow: Nature Communications, v. 9, p. 2616, doi: 10.1038/s41467-018-05042-6.

Stevenson, C.J., Talling, P.J., Sumner, E.J., Masson, D.G., Frenz, M., and Wynn, R.B., 2014, On how thin submarine flows transported large volumes of sand for hundreds of kilometres across a flat basin plain without eroding the sea floor: Sedimentology, v. 61, p. 1982–2019, doi: 10.1111/sed.12125.

Stow, D.A. V., and Johansson, M., 2000, Deep-water massive sands: nature, origin and hydrocarbon implications: Marine and Petroleum Geology, v. 17, p. 145–174, doi: 10.1016/S0264-8172(99)00051-3.

Straub, K.M., and Mohrig, D., 2008, Quantifying the morphology and growth of levees in aggrading submarine channels: Journal of Geophysical Research: Earth Surface, v. 113, p. 1–20, doi: 10.1029/2007JF000896.

Sumer, B.M., Kozakiewicz, A., Fredsoe, J., and Deigaard, R., 1996, Velocity and Concentration Profiles in Sheet-Flow Layer of Movable Bed: Journal of Hydraulic Engineering, v. 122, p. 549–558, doi: 10.1061/(ASCE)0733-9429(1997)123:10(927).

Sumner, E.J., Amy, L.A., and Talling, P.J., 2008, Deposit structure and processes of sand deposition from a decelerating sediment suspension: Journal of Sedimentary Research, v. 78, p. 529–547, doi: 10.2110/jsr.2008.062.

Sumner, E.J., and Paull, C.K., 2014, Swept away by a turbidity current in Mendocino submarine canyon, California: Geophysical Research Letters, v. 41, p. 7611–7618, doi: 10.1002/2014GL061863.Received.

Sumner, E.J., Talling, P.J., and Amy, L.A., 2009, Deposits of flows transitional between turbidity current and debris flow: Geology, v. 37, p. 991–994, doi: 10.1130/G30059A.1.

Sumner, E.J., Talling, P.J., Amy, L.A., Wynn, R.B., Stevenson, C.J., and Frenz, M., 2012, Facies architecture of individual basin-plain turbidites: Comparison with existing models and implications for flow processes: Sedimentology, v. 59, p. 1850–1887, doi: 10.1111/j.1365-3091.2012.01329.x.

Sylvester, Z., and Lowe, D.R., 2004, Textural trends in turbidites and slurry beds from the Oligocene flysch of the East Carpathians, Romania: Sedimentology, v. 51, p. 945–972, doi: 10.1111/j.1365-3091.2004.00653.x.

Symons, W.O., Sumner, E.J., Paull, C.K., Cartigny, M.J.B., Xu, J.P., Maier, K.L., Lorenson, T.D., and Talling, P.J., 2017, A new model for turbidity current behavior based on integration of flow monitoring and precision coring in a submarine canyon: Geology, p. G38764.1, doi: 10.1130/G38764.1.

Talling, P.J., 2013, Hybrid submarine flows comprising turbidity current and cohesive debris flow: Deposits, theoretical and experimental analyses, and generalized models: Geosphere, v. 9, p. 460–488, doi: 10.1130/GES00793.1.

Talling, P.J., 2014, On the triggers, resulting flow types and frequencies of subaqueous sediment density flows in different settings: Marine Geology, v. 352, p. 155–182, doi: 10.1016/j.margeo.2014.02.006.

Talling, P.J., Amy, L.A., Wynn, R.B., Peakall, J., and Robinson, M., 2004, Beds comprising debrite sandwiched within co-genetic turbidite: Origin and widespread occurrence in distal depositional environments: Sedimentology, v. 51, p. 163–194, doi: 10.1111/j.1365-3091.2004.00617.x.

Talling, P.J., Masson, D.G., Sumner, E.J., and Malgesini, G., 2012, Subaqueous sediment density flows: Depositional processes and deposit types: Sedimentology, v. 59, p. 1937–2003, doi: 10.1111/j.1365-3091.2012.01353.x.

Talling, P.J., Wynn, R.B., Schmidt, D.N., Rixon, R., Sumner, E., and Amy, L., 2010, How did thin submarine debris flows carry boulder-sized intraclasts for remarkable distances across low gradients to the far reaches of the Mississippi Fan? Journal of Sedimentary Research, v. 80, p. 829–851, doi: 10.2110/jsr.2010.076.

Tanner, L.H., 1996, Armoured mud balls revisited: Atlantic Geology, v. 32, p. 123–125.

Tarantola, A., 2005, Inverse problem theory and methods for model parameter estimation: Vol. 89 p.

Thompson, C.E.L., Amos, C.L., Jones, T.E.R., and Chaplin, J., 2003, The Manifestation of Fluid-transmitted Bed Shear Stress in a Smooth Annular Flume - A Comparison of Methods: Journal of Coastal Research, v. 19, p. 1094–1103, doi: 10.2307/4299251.

Vardy, M.E., Vanneste, M., Henstock, T.J., Clare, M.A., Forsberg, C.F., and Provenzano, G., 2017, State-of-the-art remote characterization of shallow marine sediments: the road to a fully integrated solution: Near Surface Geophysics, v. 15, p. 387–402, doi: 10.3997/1873-0604.2017024.

Warrick, J.A., and Milliman, J.D., 2003, Hyperpycnal sediment discharge from semiarid southern California rivers: Implications for coastal sediment budgets: Geology, v. 31, p. 781–784, doi: 10.1130/G19671.1.

Weimer, P., and Link, M.H., 1991, Global petroleum occurrences in submarine fans and turbidite systems: New York, Springer US.

Wiik, T., Nordskag, J.I., Dischler, E.Ø., and Nguyen, A.K., 2015, Inversion of inline and broadside marine controlled-source electromagnetic data with constraints derived from seismic data: Geophysical Prospecting, v. 63, p. 1371–1382, doi: 10.1111/1365-2478.12294.

Wilson, K.C., 1987, Analysis of bed-load motion at high shear stress: Journal of Hydraulic Engineering, v. 113, p. 97–103.

Winterwerp, J.C., Bakker, W.T., Mastbergen, D.R., and Van Rossum, H., 1992, Hyperconcentrated sand-water mixture flows over an erodible bed: Journal of Hydraulic Engineering, v. 118, p. 1508–1525.

Winterwerp, J.C., Van Kesteren, W.G.M., Van Prooijen, B.C., and Jacobs, W., 2012, A conceptual framework for shear flow-induced erosion of soft cohesive sediment beds: Journal of Geophysical Research, v. 117, p. C10020, doi: 10.1029/2012JC008072.

Wright, L.D., and Friedrichs, C.T., 2006, Gravity-driven sediment transport on continental shelves: A status report: Continental Shelf Research, v. 26, p. 2092–2107, doi: 10.1016/j.csr.2006.07.008.

Xu, J.P., Sequeiros, O.E., and Noble, M. a., 2014, Sediment concentrations, flow conditions, and downstream evolution of two turbidity currents, Monterey Canyon, USA: Deep Sea Research Part I: Oceanographic Research Papers, v. 89, p. 11–34, doi: 10.1016/j.dsr.2014.04.001.

Yin, D., Peakall, J., Parsons, D., Chen, Z., Averill, H.M., Wignall, P., and Best, J., 2016, Bedform genesis in bedrock substrates: Insights into formative processes from a new experimental approach and the importance of suspension-dominated abrasion: Geomorphology, v. 255, p. 26–38, doi: 10.1016/j.geomorph.2015.12.008.

Yu, G., and Tan, S.-K.T., 2006, Errors in the bed shear stress as estimated from vertical velocity profile: Journal of Irrigation and Drainage Engineering, v. 132, p. 490–497, doi: 10.1061/(asce)0733-9437(2006)132:5(490).

Zakeri, A., 2009, Submarine debris flow impact on suspended (free-span) pipelines: Normal and longitudinal drag forces: Ocean Engineering, v. 36, p. 489–499, doi: 10.1016/j.oceaneng.2009.01.018.

Zakeri, A., Høeg, K., and Nadim, F., 2008, Submarine debris flow impact on pipelines — Part I: Experimental investigation: Coastal Engineering, v. 55, p. 1209–1218, doi: 10.1016/j.coastaleng.2008.06.003.

Zakeri, A., Hoeg, K., Nadim, F., Uio, O., and Centre, I., 2008, OTC 19173 Submarine Debris Flow Impact on Pipelines : Drag Forces , Mitigation , and Control: